Development of NOx Estimator ECU Models for SCR After Treatment System in a Diesel Engine

Politecnico di Bari

Department of Mechanics, Mathematics and Management
MECHANICAL AND MANAGEMENT ENGINEERING
Ph.D. Program
SSD: ING-IND/08–FLUID MACHINERY

Final Dissertation

Development of NOx Estimator ECU Models for SCR After Treatment System in a Diesel Engine

---

by

Patrizia Domenica Ciliberti :

Supervisors:

Prof. Eng. S.M. Camporeale

Dr. Eng. S. Fischer

Coordinator of Ph.D Program:

Prof. Eng. Giuseppe Demelio

Course n°30, 01/11/2014-31/10/2017

Politecnico di Bari

Department of Mechanics, Mathematics and Management
MECHANICAL AND MANAGEMENT ENGINEERING
Ph.D. Program
SSD: ING-IND/08–FLUID MACHINERY

Final Dissertation

Development of NOx Estimator ECU Models for SCR After Treatment System in a Diesel Engine

---

by

Patrizia Domenica Ciliberti :

Referees:

Prof. Eng. I. Arsie

Prof. Eng. G.M. Bianchi

Supervisore:

Prof. Eng. S.M. Camporeale

Dr. Eng. S. Fischer

Coordinator of Ph.D Program:

Prof. Eng. Giuseppe Demelio

Course n°30, 01/11/2014-31/10/2017

Contents

Symbols

α_{st}	*Relative air/fuel in stoichiometric condition*	[-]
α	*Polynomial coefficient*	[-]
β	*Polynomial coefficient*	[-]
γ	*Specific Heat Ratio*	[-]
	Polynomial coefficient	[-]
λ	*Relative air/fuel*	[-]
θ	*Crank angle*	[°CAD]
v_{sq}	*Squish velocity*	[cm/s]
χ	*Volume concertation*	[mol/m^3]
A	*Area*	[cm^2]
A_c	*Cylinder section area*	[cm^2]
B	*Bore*	[-]
c_p	*Specific heat at constant pressure*	[J/K]
D_B	*Bowl Diameter*	[mm]
E	*Activation energy*	[1/K] [mol/J]
k	*Tuning /calibration coefficient*	[*]
m	*Mass flow*	[kg/h]
MW	*Molar weight*	[mol/g]
N	*Engine Speed*	[rpm]
n	*Chemical specie mole*	[mol]
p	*Pressure*	[bar]
R	*Gas Constant*	[J/mol K]
r	*Rate of reaction*	[mol/m^3 s]
T	*Temperature*	[K]
S_p	*Piston velocity*	[cm/s]
V	*Volume*	[cm^3]
V_B	*Bowl Volume*	[mm^3]
y_{O2}	*Rate of oxygen*	[-]
z	*Distance between cylinder head and piston*	[mm]

[*] depends by the contest

Subscript

AD	*adiabatic*
bw	*backward*
cg	*combusted gas*
cyl	*cylinder*
DISS	*dissociation*
EO	*Engine out*
EXH	*exhaust*
fw	*forward*
i	*i-th chemical species*
INTK	*intake*
Mdl	*model*
Meas	*measured*

ND	*non-dissociated species*
p	*pilot*
ref	*reference*
res	*residual*
reac	*reaction*
STOICH	*stoichiometric*
UB	*unburned*

Abbreviations

ANN	*Artificial Neural Network*	
ASIC	*Application-Specific Integrated Circuit*	
BMEP	*Brake Mean Effective Pressure*	[bar]
BTDC	*Before Top Dead Centre*	
CA	*Crank Angle*	[°CAD]
CR	*Common Rail*	
DOC	*Diesel Oxidation Catalyst*	
DoE	*Design of Experiment*	
DPF	*Diesel Particulate Filter*	
ECU	*Electronic Control Unit*	
EUDC	*Extra Urban Driving Cycle*	
EGR	*Exhaust Gas Recirculation*	
EoP	*Engine Operative Point*	
EVO	*End Valve Opening*	
HP EGR	*High Pressure Exhaust Gas Recirculation*	
HR	*Heat Release*	[J]
HRR	*Heat Release Rate*	[J*s]
ICPS	*In-Cylinder Pressure Signal*	
IMEP	*Indicated Mean Effective Pressure*	[bar]
ISS	*Instant Start Systems*	
IVC	*Intake Valve Closing*	
LHV	*Low Heat Value*	[kJ/kg]
LP EGR	*Low Pressure Exhaust Gas Recirculation*	
MNEDC	*Modified New European Driving Cycle*	
MFB	*Mass Fraction Burnt*	
NSC	*NOx Storage Catalyst*	
OBD	*On Board Diagnostic*	
ODE	*Ordinary Differential Equation*	
PEMS	*Portable Emissions Measurement System*	
PMR	*Power-To-Mass Ratio*	
rEGR	*Rate of EGR*	[-]
RMSE	*Root Mean Square Error*	[ppm]
SCR	*Selective Catalyst Reduction*	
SCRoF	*Selective Catalyst Reduction on filter*	
SCRuF	*Selective Catalyst Reduction under floor*	
SOC	*Start Of Combustion*	
SOI	*Start Of Injection*	
TDC	*Top Dead Centre*	

WLTC *Worldwide harmonized Light vehicles Test Cycle*
WLTP *Worldwide harmonized Light vehicles Test Procedure*

General Introduction

The need to meet current and future emission legislation and on-board diagnostic (OBD) regulation requires the set-up of further optimized interaction between engine control and exhaust gas after treatment systems. For diesel engines a particular attention is put on NOx emission.
The optimization of combustion during the engine calibration process leading to lowest engine out raw emissions is a prerequisite for a robust working exhaust gas after treatment system. The current after treatment technology for NOx reduction allows to choose between NSC and SCR as principle measures. This work focuses the attention on SCR (Selective Catalytic Reactor -SCR). The SCR efficiency estimation has a relevant role for the urea dosing strategy. For this reason, it is necessary to know the amount of NOx upstream and downstream the SCR.

Nowadays, one NOx sensor is mounted before the NOx after-treatment devices on the majority of the vehicles available on the market. The implementation of an estimator model in the ECU allows the diagnosis of the physical engine-out NOx sensor and it is more indispensable for the application in which the upstream SCR NOx sensor is not mounted for cost reasons. As any other "physical" device, the NOx sensor installation implicates aging and a calibration effort consuming adaptation of the control system parameters throughout the complete lifetime of the engine. Therefore, to overcome these difficulties, an accurate and robust model, that is able to estimate the engine-out NOx emission could replace the physical sensor.

On the other hand, the SCR downstream NOx sensor cannot be replaced. Depending on the after treatment layout, it is needed for SCR OBD and/or closed loop control. The adoption of an ECU model able to characterize the SCR behavior throughout the vehicle lifetime, improves the control of the dosed urea amount and, hence, the NOx reduction process. This is particularly true, if the after treatment layout is composed by a Selective Catalytic Reactor on Filter –SCRoF- followed by a SCR under floor –SCRuF- because the information about the ammonia slip of the first catalyst is necessary to know the exhaust gas conditions upstream of the second catalyst.

This work embraces both aspects. In the first part, a raw NOx emission model is developed and evaluated on dynamic vehicle roller bench cycles – MNEDC and WLTC. The second part deals with the implementation of a more detailed chemical reaction scheme in an already developed SCR kinetic model for engine control units. Both models aim to a real time application; but the results presented here are produced during off-line simulations.

1. Regulations and specifications

Year after year the attention on the environment protection has become higher so that the public institutions had issued regulations in order to further limit polluting emissions. The European Union has emitted several emission regulations which must be respected by all Member States.

A brief overview of the European Directives for new light duty vehicles (passenger cars and light commercial vehicles) is shown. For the purpose of emission standards and other vehicle regulations, vehicles are classified into categories, as listed Table 1.1.

Table 1.1 Vehicles categories. [1]

Category	Description
M	Motor vehicles with at least four wheels designed and constructed for the carriage of passengers.
M_1	Vehicles designed and constructed for the carriage of passengers and comprising no more than eight seats in addition to the driver's seat
M_2	Vehicles designed and constructed for the carriage of passengers, comprising more than eight seats in addition to the driver's seat, and having a maximum mass ("technically permissible maximum laden mass") not exceeding 5 tons
M_3	Vehicles designed and constructed for the carriage of passengers, comprising more than eight seats in addition to the driver's seat, and having a maximum mass exceeding 5 tons
N	Motor vehicles with at least four wheels designed and constructed for the carriage of goods.
N_1	Vehicles designed and constructed for the carriage of goods and having a maximum mass not exceeding 3.5 tons
N_2	Vehicles designed and constructed for the carriage of goods and having a maximum mass exceeding 3.5 tons but not exceeding 12 tons
N_3	Vehicles designed and constructed for the carriage of goods and having a maximum mass exceeding 12 tons
O	Trailers (including semi-trailers)
G*	Off-Road Vehicles
* Symbol G shall be combined with either symbol M or N. For example, a vehicle of category N_1 which is suited for off-road use shall be designated as N_1G.	

Emission standards for light-duty vehicles are applicable to all vehicles category M_1, M_2, N_1 and N_2 with a reference mass not exceeding 2610 kg. From 2000, the legislator has requested to the car manufacture companies the NOx reduction from 0.5 to 0.08 g/km. For more details, the EU emission standards are summarized in the following table –Table 1.2-:

Table 1.2 EU emission standards for passengers cars (category M1) [1]

Stage	Date	CO	HC	HC+NOx	NOx	PM	PN
		g/km					*#/km*
Compression Ignition (Diesel)							
Euro 1†	1992.07	2.72 (3.16)	–	0.97 (1.13)	–	0.14 (0.18)	–
Euro 2, IDI	1996.01	1.0	–	0.7	–	0.08	–
Euro 2, DI	1996.01[a]	1.0	–	0.9	–	0.10	–
Euro 3	2000.01	0.64	–	0.56	0.50	0.05	–
Euro 4	2005.01	0.50	–	0.30	0.25	0.025	–
Euro 5a	2009.09[b]	0.50	–	0.23	0.18	0.005[f]	–
Euro 5b	2011.09[c]	0.50	–	0.23	0.18	0.005[f]	6.0×10^{11}
Euro 6	2014.09	0.50	–	0.17	0.08	0.005[f]	6.0×10^{11}
Positive Ignition (Gasoline)							
Euro 1†	1992.07	2.72 (3.16)	–	0.97 (1.13)	–	–	–
Euro 2	1996.01	2.2	–	0.5	–	–	–
Euro 3	2000.01	2.30	0.20	–	0.15	–	–
Euro 4	2005.01	1.0	0.10	–	0.08	–	–
Euro 5	2009.09[b]	1.0	0.10[d]	–	0.06	0.005[e,f]	–
Euro 6	2014.09	1.0	0.10[d]	–	0.06	0.005[e,f]	6.0×10^{11} [e,g]

Engine emissions depend critically on engine operating conditions, such as speed, load or transients. A comparability of emissions between different vehicles is achieved by running an engine or vehicle over a standardized test cycle on an engine or vehicle dynamometer.

1.1 Emission test cycles

Engine emission test cycles are sequences of speed and load conditions performed on a dynamometer. The vehicle follows a prescribed driving pattern which includes accelerations, decelerations, changes of speed and load; the final test results can be obtained either by analysis of exhaust gas samples collected to bags over the duration of the cycle or by electronic integration of a fast response, continuous emission measurement. For particle mass measurement, integration usually occurs by accumulating particles on a filter. In this work, two transient cycles have been used: the MNEDC and the WLTC. [1]

The New European Driving Cycle (NEDC) comes from the ECE15+EUDC test cycle in Figure 1.1 and Figure 1.2. It is used for EU type approval testing of emissions and fuel consumption from light duty vehicles. The entire cycle includes four ECE segments repeated without interruption, followed by one EUDC segment. Before the test, the vehicle must soak for at least 6 hours at a temperature of

20-30°C; it is then started and allowed to idle for 40s. Now this idling period has been eliminated. After this modification the cycle is indicated as Modified New European Driving Cycle (MNEDC). [1]

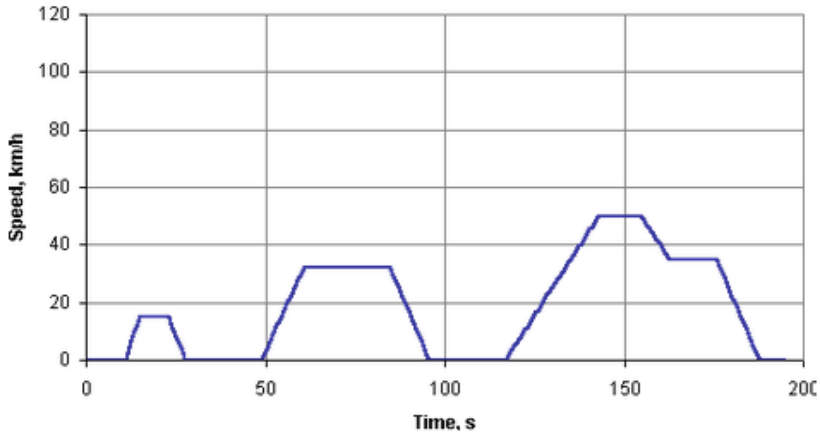

Figure 1.1 ECE Cycle [1]

The EUDC (Extra Urban Driving Cycle) segment has been added after the fourth ECE15 cycle to account for more aggressive, high speed driving modes. The maximum speed of the EUDC cycle is 120 km/h. An alternative EUDC cycle for low-powered vehicles has also been defined with a maximum speed limited to 90 km/h:

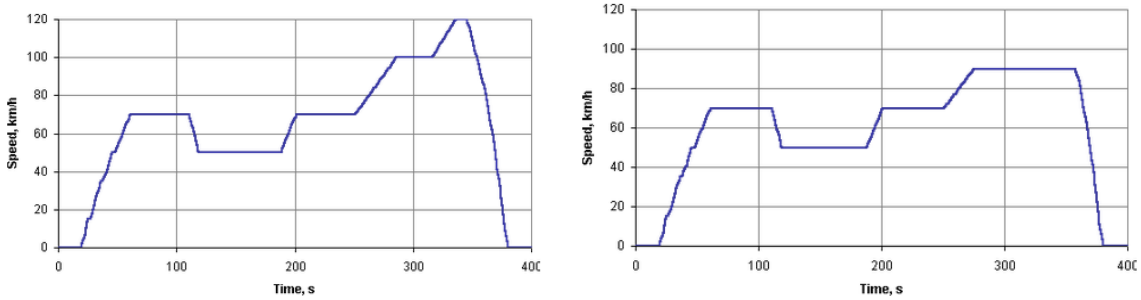

Figure 1.2 EUDC Cycle (left) EUDC Cycle for low power vehicles (right) [1]

Emissions are sampled during the cycle according to the constant volume sampling (CVS) technique, analyzed, and expressed in [g/km] for each of the pollutants. Table 1.3 includes a summary of selected parameters for the ECE 15, EUDC and NEDC cycles.

Table 1.3 Cycle parameters [1]

Characteristics	Unit	ECE 15	EUDC	NEDC†
Distance	km	0.9941	6.9549	10.9314
Total time	s	195	400	1180
Idle (standing) time	s	57	39	267
Average speed (incl. stops)	km/h	18.35	62.59	33.35
Average driving speed (excl. stops)	km/h	25.93	69.36	43.10
Maximum speed	km/h	50	120	120
Average acceleration[1]	m/s^2	0.599	0.354	0.506
Maximum acceleration[1]	m/s^2	1.042	0.833	1.042

The Worldwide harmonized Light vehicles Test Procedure (WLTP) - Figure 1.3- is a test cycle for the determination of emissions and fuel consumption from light-duty vehicles. The WLTP test has replaced the European NEDC procedure for type approval testing of light-duty vehicles. The WLTP includes three test cycles applicable to vehicle categories of different power-to-mass (PMR) ratio as presented in Table 1.4:

Table 1.4 Vehicle Categories for different PMR ratio [1]

Category	PMR	Speed Phases	Comments
Class 3	PMR > 34	Low, Middle, High, Extra-High	If v_max < 135 km/h, phase 'extra-high' is replaced by a repetition of phase 'low'.
Class 2	34 ≥ PMR > 22	Low, Middle, High	If v_max < 90 km/h, phase 'high' is replaced by a repetition of phase 'low'.
Class 1	PMR ≤ 22	Low, Middle	If v_max ≥ 70 km/h, phase 'low' is repeated after phase 'middle'. If v_max < 70 km/h, phase 'middle' is replaced by a repetition of phase 'low'.

The PMR parameter is defined as the ratio of rated power [W] and curb mass [kg]. Passenger cars belong to Class-3 Category; selected parameters for class-3 cycle are shown in Table 1.5:

Table 1.5 WLTC class-3 parameters [1]

Phase	Duration	Stop Duration	Distance	p_stop	v_max	v_ave w/o stops	v_ave w/ stops	a_min	a_max
	s	*s*	*m*		*km/h*	*km/h*	*km/h*	*m/s²*	*m/s²*
Low	589	156	3095	26.5%	56.5	25.7	18.9	-1.47	1.47
Middle	433	48	4756	11.1%	76.6	44.5	39.5	-1.49	1.57
High	455	31	7158	6.8%	97.4	60.8	56.6	-1.49	1.58
Extra-High	323	7	8254	2.2%	131.3	94.0	92.0	-1.21	1.03
Total	1800	242	23262						

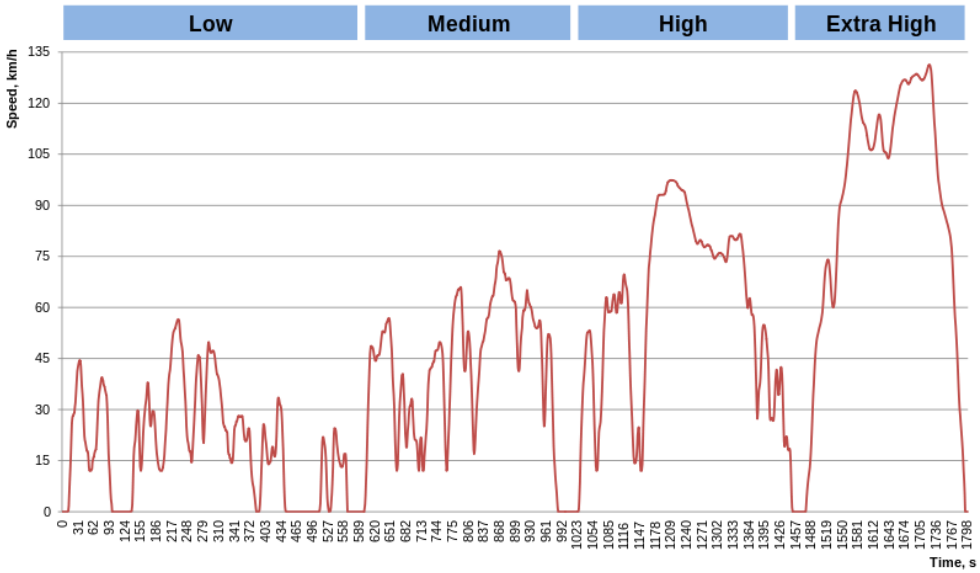

Figure 1.3 WLTC Speed profile [1]

A Real Driving Emission test will be required in addition to the standard procedure for the homologation at the roller bench. A Real Driving Emission test consists in a test on public road during which polluting emissions are measured via a Portable Emissions Measurement System (PEMS).

The NOx emission must not overcome the product between the NOx limit emission of the WLTP and a conformity factor. The conformity factor is set to 2.1 for the period 01/09/2017 to 01/09/2019; but it will be reduced to (1+0.5) starting from 01/01/2020. The added 0.5 indicates the uncertainty of the measurement system; it can be object of regulation revision.

2. Experimental Set-up

For the calibration and validation of the developed models, a wide experimental campaign has been conducted. A steady state campaign has been performed on test bench in order to calibrate the NOx raw emission model while its validation has been done on standard dynamic cycles on engine test bench.

For the development of the SCR kinetic model, the experimental campaign is composed by two parts. The first part consists in "filling and empty test" and standard dynamic cycles which are measured on test bench while real driving tests are conducted with a vehicle on the road.

2.1. Facilities

In Figure 2.1 the test cell layout and the measurement devices are represented. The test bench is equipped with a three phase asynchronous machine with a squirrel-cage rotor, that serves as dynamometer for engine speed/torque control and measurement. For measuring the torque, a lever arm connected with the cradle-mounted stator acts, via a pendulum support, on a bending beam with an applied strain gauge, that is supported against a console. The speed is measured through an optical incremental encoder. The control and monitoring of the device is fully realized via a PC-based interface, *AVL Puma*, and a dedicated test bed console (*EMCON*).

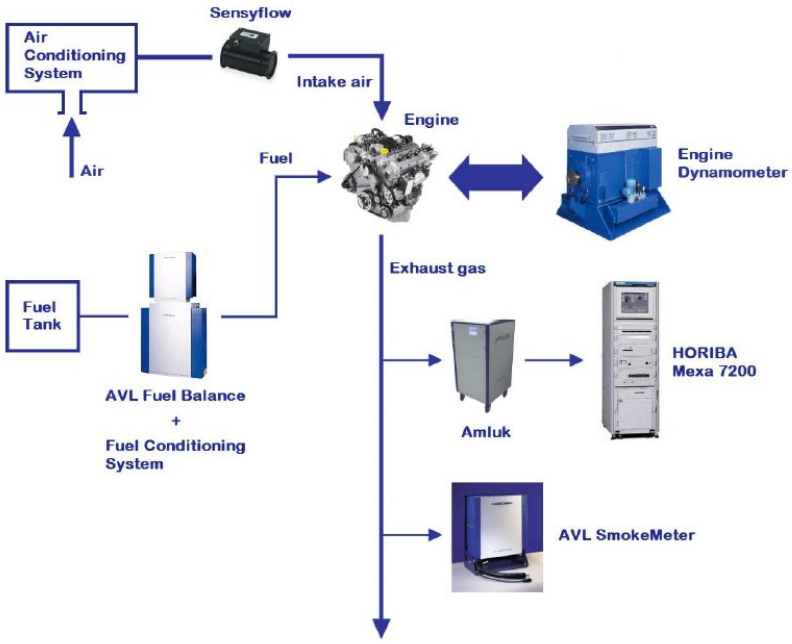

Figure 2.1 Test Bench layout

Two main intake paths can be recognized: combustor air line and fuel line. The air mass flow from the air conditioning system to the engine is measured trough a hot-film anemometer (*Sensyflow*): this method of measurement is based on the abstraction of heat from a heated body by an enveloping gas flow and the flow-dependent cooling impact is used as the measuring effect. With this measuring method the gas mass flow rate can be determined directly, without the need for pressure and temperature compensation.

The fuel injected is measured through a high-accuracy fuel balance by *AVL* (model *735*) and it is maintained at a constant temperature by the conditioning system *AVL 753C*.

Attached to the exhaust line there are the gas analysing devices. The *Amluk 209/M98 QC* is a heated pre-filter, used for exhaust gas sampling. It is not a measuring device and consists of a filter, a pump and several electro-pneumatic valves to pipe exhaust gas from engine towards the emissions analysis device, *HORIBA Mexa 7200*. This is a high-precision exhaust gas analyser. The calibration of the exhaust analyzer is performed before every measurement, comparing the measured values with sample gases from certified bombs. The *AVL 415S SmokeMeter* is a device for measuring the soot content in the engine exhaust gas, even at extremely low concentrations.

In Figure 2.2, an overview of the measurement chain is presented. The in-cylinder pressure signal is the starting point of this brief presentation. It is one of the engine control parameters. It is sampled by the pressure sensor and converted in a voltage curve (in the range 0-10V) by a conditioning system (*MicroIFEM Piezo Module*) from which the voltage signal reaches the test-bench Indicating system.

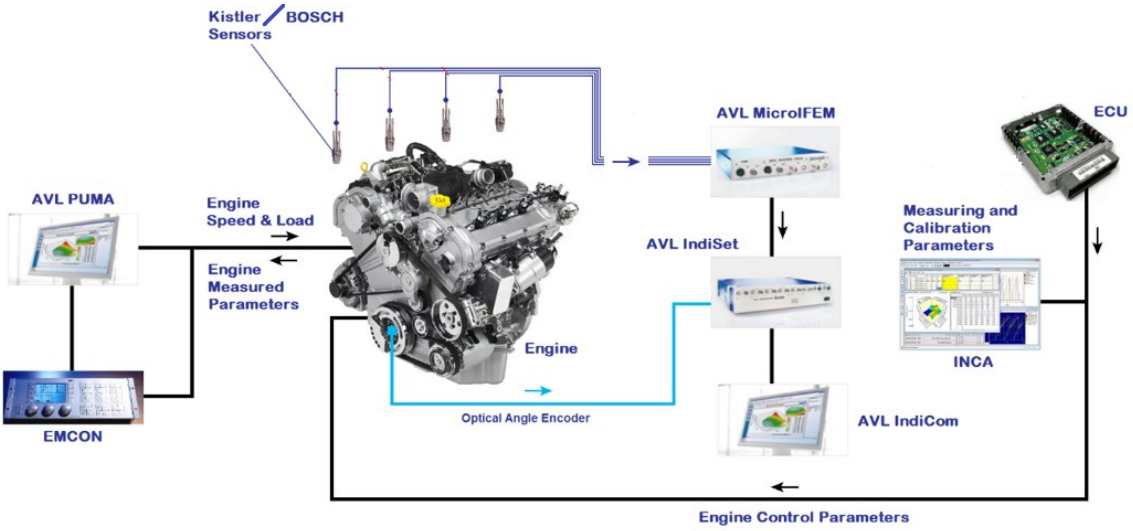

Figure 2.2 Schematics of the measurement chain.

The *MicroIFEM Piezo Module* is a compact 4-channel amplifier used to measure the electrostatic charges generated by pressure transducers in pressure, force and acceleration measurement systems. The high upper cut-off frequency (embedded 100kHz low-pass filter) permits highly dynamic measurements. The *AVL MicroIFEM* system is fully remote controlled via a serial connection and it is parameterized by means of the operating software *IndiSignal*.

The *AVL Indiset Advanced™ 631* provides, also an optical crank angle encoder, which triggers the data acquisition with a resolution of 0.1 °CA, and a specific software, engine data recording and visualization and allows real time combustion analysis by the calculation of the most useful indicating parameters (*IMEP*, heat release parameters, etc.) according to standard post processing algorithms, as well as customized algorithms. It is linked to a standard PC via a serial link interface (10 Mbit/s). A post-processing software tools from AVL GmbH- AVL IndiCom™ and AVL CONCERTO – allows the visualization of the measurements.

IndiCom is a user interface control software for all AVL indicating systems and it includes: a data visualization and output module, which allows data and results to be displayed using diagrams and reports, either offline or online, even during a measurement; a parameterization module (AVL IndiPar), which is used for parameterizing data acquisition, measurement types and real-time evaluations; a formula/macro/script editor, which is a text editor for writing formulas, macros and scripts for operating sequences; a graphic indicating formula editor (CalcGraf), which is a graphical editor that allows the user to define customized calculation procedures. AVL IndiCom constitutes the real time-capable core of the graphics package CONCERTO.

2.2. In-cylinder pressure sensor

Particular attention should be put on the in-cylinder pressure sensor because the main requirement of this work is the use of variables derived from the in-cylinder pressure signal for the development of the NOx model estimator.

The available technology allows to choose between piezoelectric sensor and piezoresistive sensor. During the development of the activity, both of them have been used. In particular, the AVL and Klister sensors are piezoelettric sensors while the Beru series sensors are piezoresistive. The AVL and Klister sensors are designed and developed for laboratory measurements; for this reason, they are more accurate than the Beru ones. In the following paragraph, details about their technology are explained.

Piezoelectric Sensor

A glow plug integrated pressure sensor combines both glowing and sensing functionalities, since it carries a piezoelectric pressure sensor, but it also works as a conventional glow plug in an *ISS* (*Instant Start Systems*).

As it is possible to see in Figure 2.3, the measuring element is contacted and pre-tensioned with appropriate insulation within the glow plug body. The heating rod, which is usually tightly pressed into the glow plug body, is designed to slide with a coaxial movement and transfers the pressure as a force to the sensing crystal. The actual pressure sensor is not directly exposed to the combustion flame, because it is located away from the combustion chamber, in an area where much more favourable ambient conditions prevail.

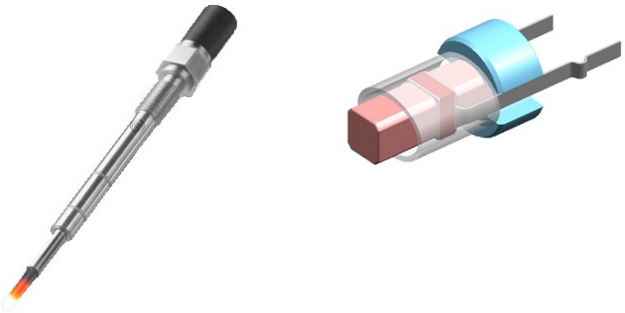

Figure 2.3 Glow Plug Combustion Pressure Sensor (left) and detail of the sensing element. [2]

This structure, using the glow plug as a transmission element, is helpful to avoid the well-known problems of temperature resistance and thermal shock, but, however, it requires an enhanced sealing against hot combustion gases and soot.

Charge signal processing and voltage output generation take place in a sensor-integrated electronic module *ASIC* (*Application-Specific Integrated Circuit*) incorporating a differential charge amplifier with high input impedance and a logic control unit which triggers the discharge of the internal capacitors (*reset*) by evaluating the output, in order to compensate signal drift. [2] Among the pressure sensors available on the market, the AVL GH13P has been chosen. In Figure 2.4, the data sheet of the piezoelectric sensor AVL GH13P is shown.

Measuring range			0 ... 250 bar	
Overload			300 bar	
Lifetime	≥		10^8	load cycles
Sensitivity			16 pC/bar	nominal
Linearity	≤	±	0.3%	FSO
Natural frequency	–		115 kHz	
Acceleration sensitivity	≤		0.001 bar/g	axial
Shock resistance	≥		2000 g	
Insulation resistance	≥		10^{13} Ω	at 20 °C
Capacitance			7 pF	
Operating temperature range	≤		400 °C	
Thermal sensitivity change	≤		2%	20 ... 400 °C
	≤	±	0.5%	250 ± 100 °C
Load change drift			1 mbar/ms	max. gradient
Cyclic temperature drift *	≤	±	0.5 bar	
Thermo shock error **				
Δp	≤	±	0.3 bar	
Δp_{mi}	≤	±	1.5%	
Δp_{max}	≤	±	1%	
Mounting bore			Ø 4.3 mm	front sealed
Cable connection			M3x0.35	negative
Weight			4.7 grams	without cable
Mounting torque			1.5 Nm	

*) at 7 bar IMEP and 1300 rpm, diesel
**) at 9 bar IMEP and 1500 rpm, gasoline

Figure 2.4 Data sheet of AVL GH13P sensor [2]

Piezoresistive Sensor

In a Beru piezoresistive sensor - Figure 2.5-, the heating rod, which is usually pressed tightly into the glow body, is designed to be movable. The glow tube and the inner pole are extended and protrude from the glow plug body at the top. There the measuring diaphragm is welded to the body and glow tube. The heating rod is flexibly mounted in the Pressure Sensor glow plug body and transfers the pressure as a force to a diaphragm. The three necessary sensor contacts are arranged concentrically around the high current contact with different diameters on three levels. The decoupling of the plug from the movable heating rod takes place for the sensor contacts by means of spring contacts and by the special design of the high current contact at the inner pole of the glow plug. [2]
This kind of sensors, cheaper than the previous type, does not ensure the same level of accuracy; furthermore, pressure curves generated, are affected by electronic noise and pre-filtering is needed. It has not chosen for this application.

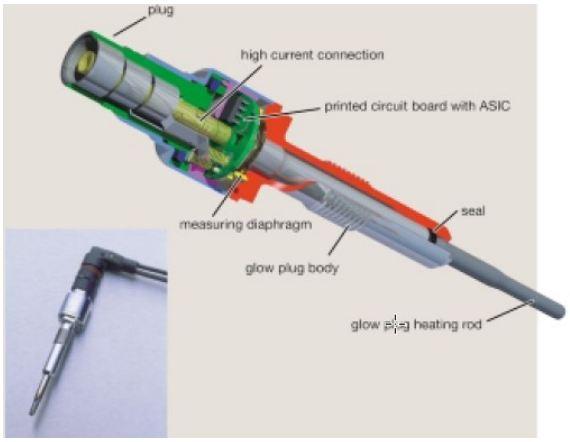

Figure 2.5 Piezoresistive Pressure Sensor scheme [2]

2.3. Experimental Set-up for NOx Model Emission Model

For the NOx raw emission model two engines have been used. The selected engines have characteristics as illustrated in Table 2.1. Both of them are equipped with a common rail system by Bosch with a maximum fuel pressure of 2000 bar for Engine 1 and of 1800 bar for Engine 2.

Table 2.1 Characteristic parameters of Engine 1 and Engine 2

	Engine 1	Engine 2
Displaced volume	1968 cm^3	1968 cm^3
Stroke	95.5 mm	95.5 mm
Bore	81 mm	81 mm
Connecting Rod	144 mm	144 mm
Compression ratio	16.2:1	16.5:1
Number of cylinder/valves per cylinder	4/4	4/4
Power/at engine speed	110 kW/4000 rpm	103 kW/4000 rpm
Torque/at engine speed	320Nm/1750-3000 rpm	320Nm/1750-3000 rpm
Maximum fuel injection pressure	2000 bar	1800 bar
Injector type	Solenoid	Piezoelectric

Also for the exhaust gas treatment, the engine layouts are different. Engine 1 is equipped only with LP EGR while Engine 2 has been equipped with high and low pressure EGR which functional scheme are represented in Figure 2.6 .

In the HP EGR, the exhaust gas is sampled at the exhaust manifold, cooled in the EGR cooler and mixed into the fresh air flow in the intake manifold. The exhaust gas recirculation depends on the pressure difference between the exhaust and the intake manifolds and EGR valve position. If it is necessary, the pressure difference can be regulated via a throttle valve mounted between the compressor and the HP EGR valve. The HP EGR has a high influence on the NOx reduction and can lower the cooling of the after treatment system for low loads. In the used layout, it has not got a cooling system. In this case, the compressor is not dirtied by soot. In the Low Pressure –LP – EGR, the exhaust gas is sampled after the Diesel Particulate Filter –DPF-, cooled in the EGR cooler and mixed into the fresh air upstream the compressor.

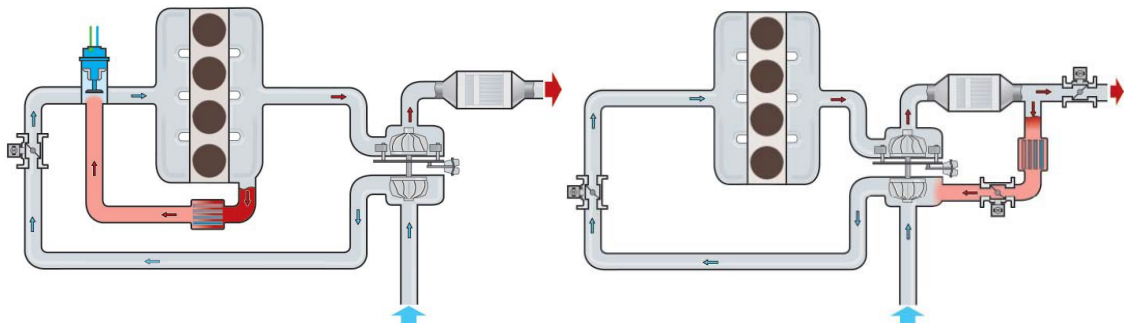

Figure 2.6 Functional scheme of a HP EGR (left), LP EGR (right)

2.4. Experimental Set-up for SCR Kinetic Model

For the experimental activity of the SCR kinetic model improvement, a third engine "Engine 3" and a vehicle, in which the Engine 3 is mounted, are used. The main characteristics are summarized in Table 2.2.

Table 2.2 Characteristic parameters of Engine 3.

	Engine 3
Displaced volume	1653 cm^3
Stroke	80.2 mm
Bore	81 mm
Connecting Rod	152 mm
Compression ratio	16.2:1
Number of cylinder/valves per cylinder	4/4
Power/at engine speed	100 kW/ 4000 rpm
Torque/at engine speed	300 Nm/1750-3000 rpm
Maximum fuel injection pressure	2000 bar

In Figure 2.7, the adopted after-treatment layout is presented. As a common practice, the exhaust flow passes through the DOC as a first step. It oxidizes soot, HC and CO. Then, the exhaust gas flows into the SCRoF - total volume is 3.4l-. It works as a SCR and a DPF at the same time. Further NOx reduction is achieved in the second SCR also called SCRuF –SCR under floor. In Chapter 8 will be given further details about possible after treatment layouts.

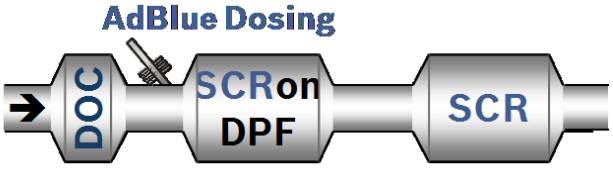

Figure 2.7 After-treatment layout for the test bench activity

Development of a NOx Raw Emission Model based on in-cylinder pressure

Introduction

The possibility to implement fast-predictive emission models in the ECU that are able to follow the engine behavior throughout its complete lifetime, can increase the system capability to reduce emissions with higher efficiency.
Important information on the behavior of the engine and, in particular, on the combustion process can be deducted from the in-cylinder pressure signal (ICPS).
ICPS is not a real novelty on the market: sensors with adequate robustness and resistance have been under development since the 80s, but only in the last decade continuous research made them withstand the high pressure in the chamber at a feasible price.
The importance of the in-cylinder pressure sensor is mainly due to the impact on system control strategies as they change in some close-loop modus: after-treatment system has a high safety tolerance because of operational uncertainty and aging because a ICPS based NOx raw emission model can reduce those tolerances. For these reasons, importance is given to the estimation of NOx raw emissions by exploiting in-cylinder pressure sensor.

The aim of this work is to replace or diagnose the NOx sensor mounted upstream of the SCR.
for this purpose, the requirements for the model are: a maximum relative error of 10 % for the estimation of NOx amount higher than 100 ppm and maximum relative error of 20 % for the estimation of NOx amount lower than 100 ppm (taking into account the accuracy of the NOx sensor on-board). After a brief overview on the possible kind of approach for NOx raw emission estimation, the steady state calibration and analysis and the dynamic validation are shown. The model is calibrated on Engine 1 while Engine 2 has been used for supporting measurements.

3. NOx Formation Process

The design of a model capable to predict NOx concentration produced by a Diesel engine both in steady state and dynamic conditions starts from the study of the combustion process in order to identify when and how NOx are formed.

Considering Dec's conceptual combustion scheme, after the ignition delay, the combustion develops in a fuel-rich premixed flame followed by a local stoichiometric diffusion combustion. soot and incomplete combustion products are formed during the rich-premixed combustion while NOx are formed during the diffusion combustion. In particular, the NOx formation process takes place both on the flame front and in the post-flame region; but the dominant zone of NOx formation is the post-flame zone because the flame front is very small (roughly 0.1 mm), leading to short residence times in the flame zone.[4][11]

High values of in-cylinder temperature (> 1800 K) and the availability of O_2 in stoichiometric condition lead to NOx production. Mass and energy transports, guaranteed by turbulence, can have a significant role for the creation of the condition for production of NOx. As a consequence, in-cylinder temperature, the availability of O_2 and turbulence are the main physical factors that characterize the process. Moreover, it is possible to consider the heat release rate as the physical variable that is able to describe how the combustion process is proceeding. Therefore, even if there is not a direct correlation between NOx production and heat released rate, it can be used as an important factor for the development of a NOx model. In Figure 3.1, the main physical relations, that deal with NOx formation, are schematized. In the following sections each physical variable identified is developed.

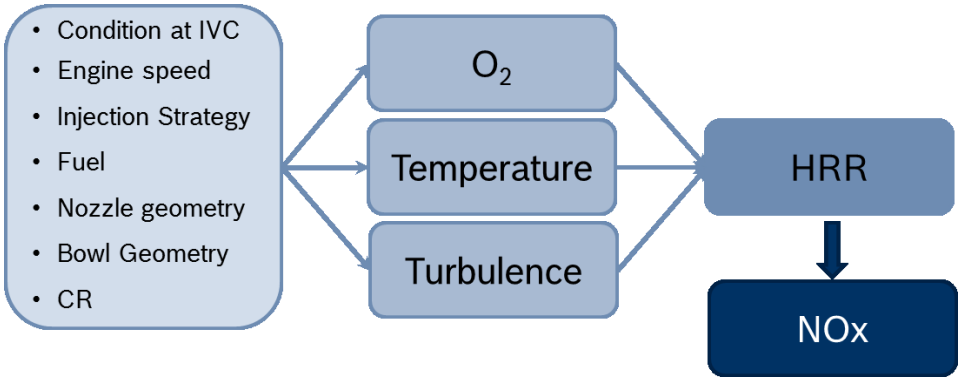

Figure 3.1 Schematic relationship of the main physical variables involved in the NOx formation process

3.1. Condition at Inlet Valve Closing

The air management parameters such us EGR rate, intake pressure and intake temperature are the most influential variables on O_2 availability and on in-cylinder temperature values. At the test bench, it is possible to range O_2 availability applying intake air quantity and/or intake pressure variations and keeping, at the same time, the intake temperature constant thanks to the presence of intercooler. In Figure 3.2, the NOx trend as function of intake oxygen rate is shown. The reduction of intake oxygen caused by an increase of the EGR rate leads to a combustion characterized by lower in-cylinder peak temperature and pressure and lower NOx.

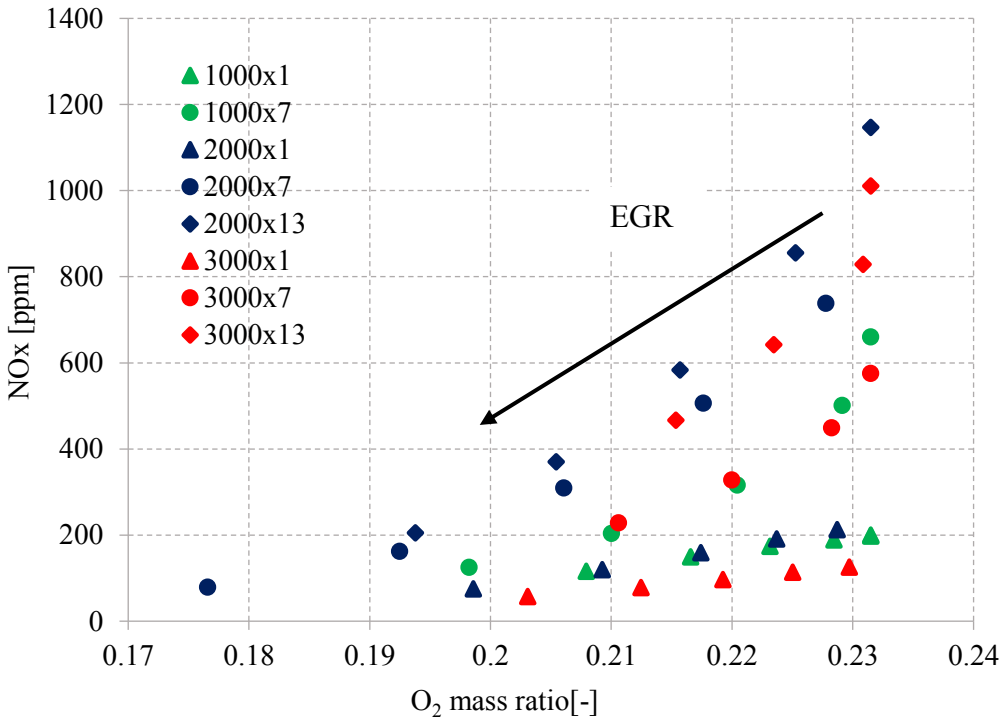

Figure 3.2 NOx production when EGR is varied. The EoPs are identified with [rpmxbar]

3.2. Turbulence Effect

Turbulence has an important role in NOx formation process because it is able to create the local condition –in cylinder temperature and quantity of O_2 available- necessary to NOx formation. Generally, a high level of turbulence enhances the combustion process because it reduces the quantity of incomplete combustion products and soot, but it leads to a higher NOx production. [4][5] Engine speed, injection strategy and common rail pressure influence the level of turbulence in the combustion chamber. A higher engine speed leads to a higher air motion that improves the mixing between fuel and air. In contrast, a higher engine speed reduces the available time for oxidation reaction and the incoming of expansion stroke freezes them. [4][5]

The injection system and the injection strategy affects strongly the development of the spray and air-fuel mixing. The expression "injection strategy" means injection pattern, injection timing and rail pressure. All these factors, among them the nozzle geometry in particular, influence the spray formation that is characterized by cone angle, flame lift off length, flame length, fuel exit velocity. These parameters define the turbulence in the chamber. [3][4][5]In this examination, the attention is focused only on the injection strategy.

A complete and typical injection pattern includes one or more pilot injections, a main injection and a post injection. As it is illustrated in Figure 3.3, the main contribution to NOx formation is related to the main injection because it is the one with the highest value of injected fuel mass and its combustion causes the peak of in-cylinder pressure and, thus, temperature. The pilot injections have not a direct relation to the NOx formation, but they influence the heat release rate and, in general, the proceeding of the combustion development. Thus, it is necessary to consider them in the study. The post injection has a marginal influence on NOx and it can be ignored in the study. [4][6][19][36]

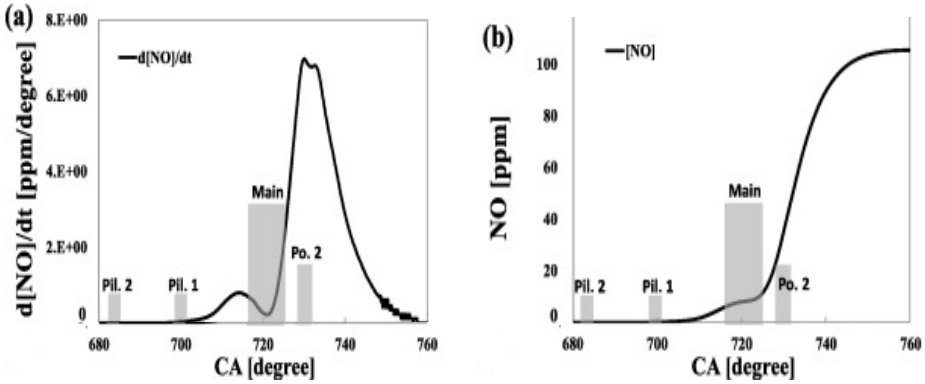

Figure 3.3 Effect of injection pattern on NOx formation rate and NOx production [19]

The injection timing has a relevant role on the determination of the in-cylinder pressure curve and on heat release rate estimation. For a conventional combustion strategy, when the start of main injection - SOI_{main} - is advanced, the peak pressure and in-cylinder temperature increase. This leads to higher local flame temperature and, thus, to higher NOx emission. [4][6][19][36]The experimental data confirm this trend.- Figure 3.4.

A high rail pressure means a high atomization level to the injected fuel. A high atomization increases the spray penetration. The resulting effect is an increase of NOx as it is possible to observe in Figure 3.5. A higher flame surface available leads to a faster combustion and a greater region with higher temperature. At the same time, a higher rail pressure means more probability of flame impingement on the chamber wall. It is recommended to avoid this phenomenon because it deteriorates the combustion process and it can create a thin fuel layer on the wall chambers that modified the normal heat transfer process and it is one of the area where soot and HC are formed.[7][8][9].

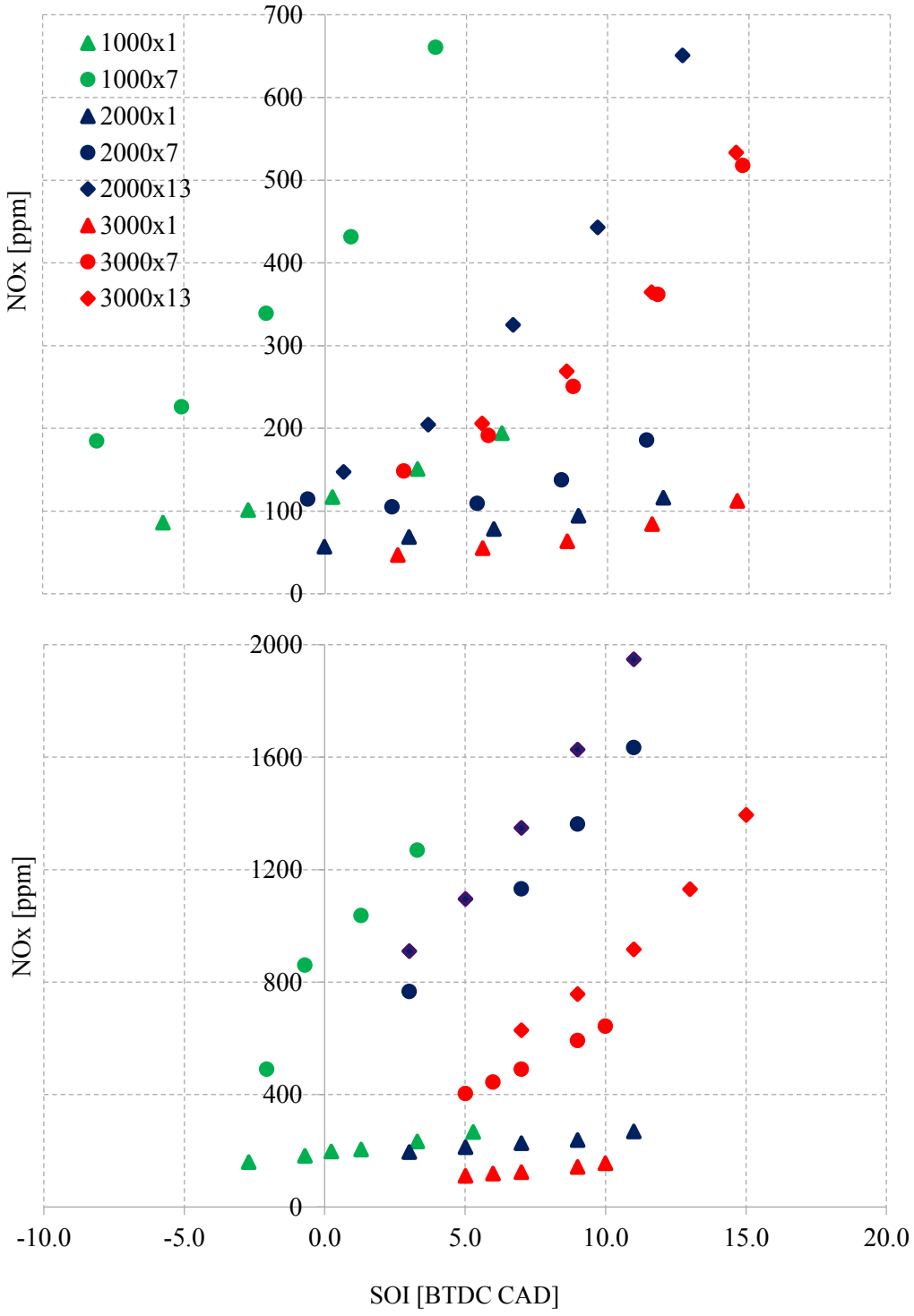

Figure 3.4 NOx production as function of main injection timing in nominal condition with EGR (a) and without EGR (b). The EoPs are identified with [rpmxbar]

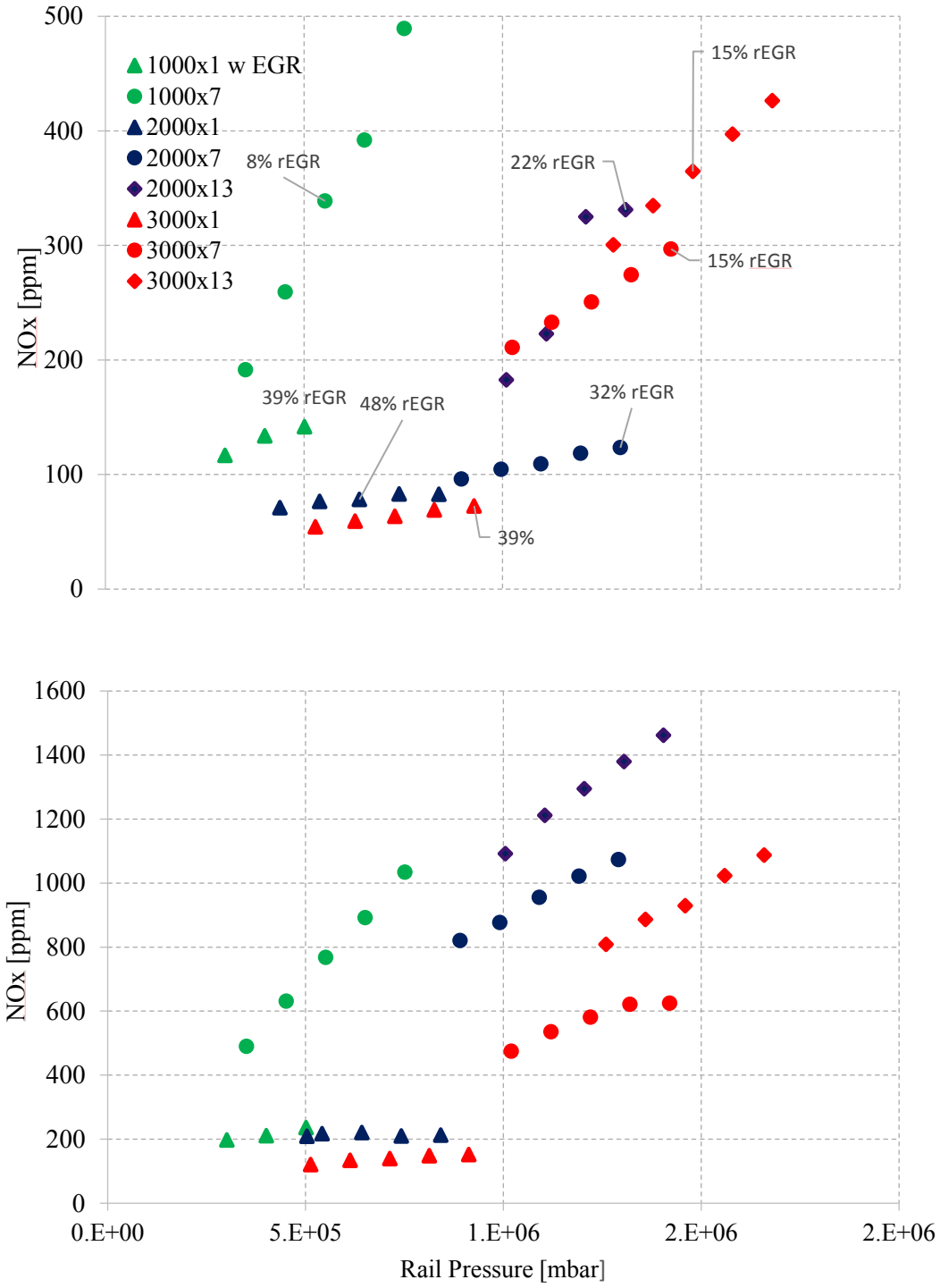

Figure 3.5 NOx production as function of rail pressure in nominal condition with EGR (a) and without EGR (b). Each EoP are characterized by engine speed and load

It is possible to notice that the range of variation of NOx for low loads is lower than for high loads. This behavior, as it will be demonstrated in the Chapter 7, leads difficulties during the NOx model developing activity because it is easier to introduce a mathematical expression able to estimate NOx when there is a wide NOx variation – which characterizes high loads- rather than the case with low NOx variation range –which characterizes low loads.

The presented analysis considers only the effect of engine control parameters, which have effects on oxygen availability, on in-cylinder temperature and reaction velocity because the developed model takes into account only them as a first step. The environmental conditions should be included among the parameters that affect the condition of the charge at the intake, if further development have to be conducted. In particular, the effect of humidity at the intake can not be neglected because for a variation of 100% of relative humidity, the NOx reduction is about 30% due to the increase of water amount that leads to an increase of heat capacity and lower values of the in-cylinder temperature.

3.3. Chemical Model

The expression NO_X is used to refer both to nitric oxide (NO) and nitrogen dioxide (NO_2), even though the former is the predominant one in the cylinder. The complete reaction scheme describing NOx formation process is complex and composted by at least 67 reactions, but four main mechanisms have been identified:

- thermal mechanism or Zeldovich mechanism
- prompt mechanism
- NO_X formation via nitrous oxide (N_2O)
- NO_X formation from fuel nitrogen.

The choice of the reaction mechanism that has to be considered is yet an open question and several authors underline this unresolved topic. Figure 3.6 summarizes the common chemical schemes that can be adopted based on the application. Mellor at al. suggest the N_2O mechanism and the Zeldovich mechanism in lean conditions and at high pressures which are the typical conditions of Diesel combustion. [51] In the common practice and in this work, it is adopted only Zeldovich mechanism for a Diesel engine combustion.

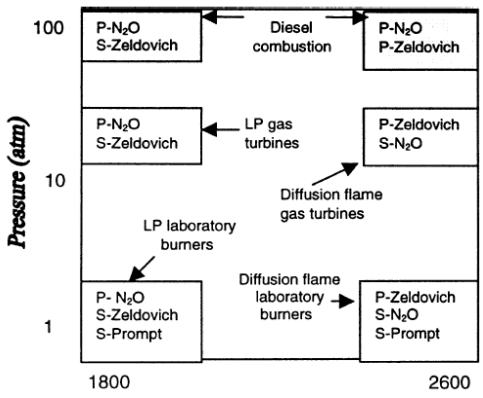

Figure 3.6 Reaction scheme based on temperature and pressure [51]

3.3.1. Zeldovich Mechanism

The well-known Zeldovich mechanism consists in the reaction presented in Table 3.1. It is important to highlight the high activation energy (argument of the exponential term) in the first reaction of Table 3.1: this high value results from energy needed to break the strong N_2 triple bond and this is the reason why thermal NO_X are the major source of pollutants in Diesel engine, whose combustion is characterized by high pressure and temperature.

Since thermal NO_X are so temperature sensitive, variation with air/fuel equivalence ratio must be expected with a peak in near-stoichiometric conditions; furthermore, as they cover the most part of NO_X production, modelling temperature in the combustion chamber is a basic requirement for a good estimation of NOx emissions. [9]

Table 3.1 Extended Zeldovich mechanisms with their rate constant [9]

Reaction	Rate constant, $cm^3/mol \cdot s$	Temperature range, K	Uncertainty, factor of or %
(1) $O + N_2 \rightarrow NO + N$	$7.6 \times 10^{13} \exp[-38{,}000/T]$	2000–5000	2
(−1) $N + NO \rightarrow N_2 + O$	1.6×10^{13}	300–5000	±20% at 300 K 2 at 2000–5000 K
(2) $N + O_2 \rightarrow NO + O$	$6.4 \times 10^{9}\ T \exp[-3150/T]$	300–3000	±30% 300–1500 K 2 at 3000 K
(−2) $O + NO \rightarrow O_2 + N$	$1.5 \times 10^{9}\ T \exp[-19{,}500/T]$	1000–3000	±30% at 1000 K 2 at 3000 K
(3) $N + OH \rightarrow NO + H$	4.1×10^{13}	300–2500	±80%
(−3) $H + NO \rightarrow OH + N$	$2.0 \times 10^{14} \exp[-23{,}650/T]$	2200–4500	2

3.3.2. NO formation via N_2O mechanism

For NO formed by the nitrous oxide mechanism, Malte and Pratt [51] postulated reactions involving N_2O formation which combine with radicals (O-atom and H-atom) to form NO. The N_2O mechanism consists of steps such as:

$$O + N_2O \Leftrightarrow 2NO \quad \text{R 3.1}$$

$$O + N_2 + M \Leftrightarrow N_2O + M \quad \text{R 3.2}$$

$$N_2O + H \Leftrightarrow NO + NH \Rightarrow 2NO \quad \text{R 3.3}$$

$$O_2 + M \Leftrightarrow 2O + M \quad \text{R 3.4}$$

For high-pressure conditions, Polifke et al. [52] found that N_2O is mainly decomposed through the reverse of reaction R 3.5, while decomposition due to radical attack is secondary. In contrast, at atmospheric conditions the importance of H-atom and O atom to N_2O destruction cannot be ignored. Since Diesel combustion occurs under the former, the N_2O reactions relevant to model NO formation in Diesels are reactions R 3.4, R 3.5 and R 3.7, based on the work of Polifke et al. [52].

3.3.3. Prompt mechanism

Also called Fenimore NO, prompt NO occurs at low temperatures and in rich premixed flames. Fenimore concluded that the NO formed early in the flame was the result of the attack of a hydrocarbon free radical on N_2. The rate of oxidation of the fuel is usually sufficiently rapid that fuel radicals like CH are at low concentrations that reactions such as CH + N_2 are negligible. Under certain fuel-rich conditions, however, hydrocarbon radicals can reach high enough concentration levels that reactions with N_2 can become an important mode of breaking the N_2 bond and, in turn, be responsible for significant NO formation. Such reactions appear to have relatively low activation energy and can proceed at a rate comparable to that of the oxidation of the fuel. Because of the early formation of NO by this mechanism, relative to that formed by the Zeldovich mechanism, NO formed is often referred to as prompt NO. Since the attack of N_2 by O is highly endothermic, most prompt NO is formed relatively late in fuel-lean flames, after CO has been formed but before the final C/H/O equilibrium is achieved. Since prompt NO are negligible with respect to the total NOx amount, their modelling will be disregarded.

Another source of NO_X pollution formation is fuel nitrogen. Even though Diesel fuel has more N_2 than gasoline, in [9] it is suggested that it is a minor source of NO_X.

4. General classification

The formation of pollutants in internal combustion engines is rather difficult to predict theoretically or by numerical simulation. This is primarily due to the fact that these phenomena are governed by a detailed spatial and temporal distribution of the mixture composition, temperature, and pressure inside the combustion chamber. All the possible approaches rely on the fundamental assumption that the pollution formation process depends, in a deterministic way, on the control inputs and on the thermodynamic boundary conditions. Of course, this determinism is not entirely true in real situations, such that only average estimations of engine-out pollutant concentration levels are possible. [13]

There are several kinds of models to simulate NOx, but the choice depends on the particular application. In order to classify all the possible models, three criteria are considered as shown in Table 4.1. [13]
The first one is the sampling period: the models can be quasi-static, cycle resolved or crank angle resolved. The second one is the kind of input variables: they can be limited to control variables and measured variables from the air path sensors, which correspond to standard Engine Control Unit (ECU) variables, or in-cylinder pressure based variables. The third one is the mathematical model approach.

Table 4.1 General classification of models for NOx estimation

Model Name	Sampling period	Input variables	Model
Empiric or Black Box	quasi-static	- Injection strategy - Air system variables - In-cylinder pressure signal variables	- 2D static map - polynomial expression - neural network
	cycle resolved		- neural network
Semi-empiric or Grey Box	cycle resolved	- Air system variables - In-cylinder pressure signal variables	Algebraic expression base on physic assumption
	crank angle resolved		
Thermodynamic or White Box	crank angle resolved	- Species concentration - In-cylinder signal variables	ODE
CFD	crank angle resolved		ODE

From a computational point of view, black box models represent the simplest possible models while CFD models are the most complex. A low computation effort allows to have a real time application, but it requires a high number of experimental data for the calibration phase and it has not a high accuracy outside the training field. The opposite characteristics are typical for a white box model - Figure 4.1.

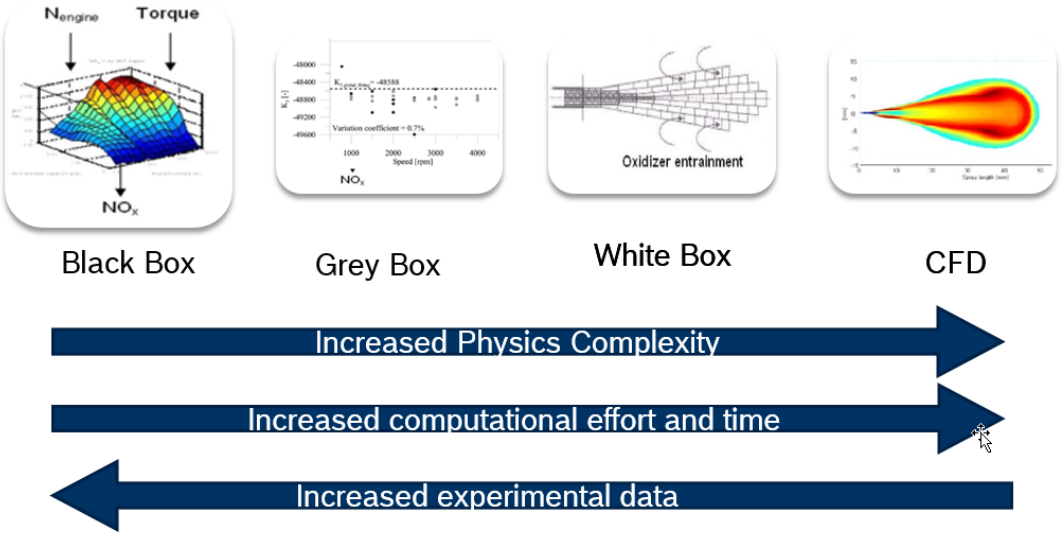

Figure 4.1 Overview of the general classification of models for NOx estimation

In this Chapter is to investigate all possible ways to design a NOx model control-oriented, this constrain limits the investigation from black box to physic model (white box). Nevertheless, CFD simulation remains a valid supporting tool for NOx model design because it is able to define NOx formation areas. For any type of model, the necessary steps for the creation of the model are:

1) Input identification
2) Model design
3) Training
4) Validation using steady state measurements and dynamic traces.

4.1 Empirical or Black Box Model

A black box model does not require a physical/chemical description of the phenomena because it consists of a mathematical relation between a set of measured input and output. It requires low complexity and limited calculation power and time.

There are two different approaches: global and global-local. In a global approach, all the inputs for the emission model are introduced equivalent in the model structure. “Global” refers to the equal treatment of the engine operation points, defined by the engine speed and the desired injection quantity, to the other inputs. In a “global-local” approach, the engine speed and the desired injection quantity are regarded separately: they are determined by the drivers request and are not included in the local models. Thus, for each operation point a local model is parametrized. [47]

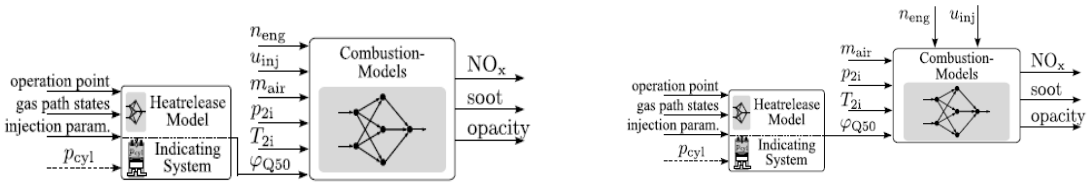

Figure 4.2 Example of global (a), global-local (b) models [47]

Among the empirical models, grid models are the most employed models in the ECU for their low power effort required. They frequently have a nested structure in order to describe a complex phenomenon. The composition of the grid map (input variables) are often engine speed and torque that individuates the engine operative point; but for a more articulated model design it is possible to introduce maps that are based on other physical variables. In this case, a correlation analysis is compulsory. A grid model is suitable for steady state NOx estimation. For transient emission this limit is overcame with a simple linear interpolation. [12][47][48]

Instead, in an Artificial Neural Network and polynomial relations expression, NOx emissions can be modelled as a function of several control (injection parameters, actuator positions) or measured variables from the air path sensors (air mass flow, intake manifold thermodynamic conditions, …). Others consider the response of the system in terms of combustion development by using cycle-resolved in-cylinder variables calculated from the cylinder pressure signal. To capture the slow dynamic of the air path, same authors feed the models not only with instantaneous values of input

variables, but also with the derivatives of these inputs or/and with the values for previous engine cycles.

Artificial Neural Networks are a family of models inspired by biological neural network. They can be used to find highly nonlinear relationships between physical variables due to their ability to predict cases that are not included in the training set. A neural network is composed by several "neurons" which are organised in at least three layers: input layer, hidden layer and output layer. Each neuron is a physical variable involved in the physical description of the phenomena and the relationship between each neuron is a mathematical expression activated by a weighting factor. Following the step highlighted previously:

1) Input identification

Table 4.2 collects the common selection of input for a ANN available in the literature. It is possible to recognized variables dealing with turbulence (e.g. engine speed, start of injection…) and air path (e.g., rate of EGR, mass of air at intake).

Table 4.2 Input selection example for Artificial Neural Network

[42]Desantes, J. et al.	N, SOI, rEGR, p_{rail}, p_{boost}, m_{air}, m_{fuel}, nozzle diameter
[43] Traver, M. et al.	P_{peack}, IMEP, Ignition Delay, MFB50, Heat Release
[44]*Arsie, I. et al.	N, SOI, p_{int}, λ
[45] Wang Jun et al.	N, SOI, Δp_{max}, Δp_c
[46] Henningsson et al.	N, SOI, Injection duration
[47] Atkinson, C. et al.	N, p_{boost}, rEGR, T
[48] Heiko Sequenz et al.	N, MFB50, p_{int}, m_{air}, m_{fuel}, T_{int}

*) Gasoline Engine example

2) Model Design

The processing elements of a Neural Network consists of many computational elements arranged in several layers. A proper design must ensure a training data set extensive enough, then select the proper stopping criteria to prevent overtraining and, finally, define the network structure with the minimum number of weights.

As the number of neurons increases, the ANN ability to deal with more complex problems also increase. At a certain point, a balance between complexity of the problem and limited number of data available for the training is reached. [41][42][43]

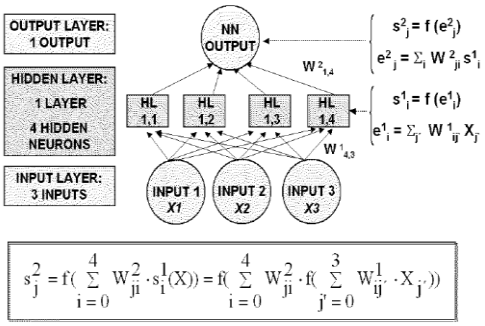

Figure 4. 3 Scheme of an Artificial Neural Network [42]

3) Training and Validation

Table 4.3 collects some of empirical model results found in literature. As can be noticed, they are characterized by a high computational effort, but they ensure a good performance. The results refer to the steady state case and they are all real time applications. The in-cylinder pressure is an input variable for the calculation of MFB50 or for the calculation of peak pressure.

Table 4.3 Main result of Empirical or Black Box Model

Author	R^2	Relative Error [%]	Total number of test
[42] Desantes	0.994	-	680
[43] Traver	0.998	-	EOP 64
[43] Traver	0.993	-	EOP 64
[44] Arsie	-	3.39	-
[45] Wang	-	2.5	350
[46] Hennigsson	0.899	-	-
[47] Atkinson	-	10	-
[48] Morales	0.968	-	64 EOP

4.2 Semi-physical model or Grey Box Model

A semi-physical model tries to capture the physics of the phenomena with an algebraic relation that uses coefficients opportunely tuned. An accurate and close description of the actual process in the combustion chamber is not possible to obtain, but the tuning coefficients can compensate any differences which arise between the actual combustion process and the approach for modelling the combustion process. Grey box models can include black box sub-models for the calculation of intermediate variables which are input for the NOx estimator sub-model.

1) Input Identification

Due to the simplicity of the algebraic relation adopted in the NOx estimator model, it is necessary to omit negligible effects. For this reason, it is not recommended to consider other chemical mechanisms than the extended Zeldovich because in a semi empirical model there is not a detailed flame description which would involve more chemical reactions. These models take as input combustion related variables, calculated from the in-cylinder pressure signal, rather than control variables. In Table 4.4, the mains input are summarized.

Table 4.4 Example of input selection for semi-empirical models

O_2	rO2, rEGR
Turbulence	N, p_{rail}, SOI, p_{boost},m_{fuel}
Heat Release	HRR
Temperature	T_{AD}

2) Model Design

In a grey box model are noticeable three main sub-models:

- Air path
- In-cylinder process
- NOx model estimator

The air path model delivers the thermodynamic condition at the intake manifold (P_{int}, T_{int}) and the charge composition with a particular reference to the rate of EGR and/or the mass concentration of O_2 to the following sub-models. The second step is the modeling of the combustion process. It can be

done through the estimation of the in-cylinder temperature and the heat release rate, if required by the NOx estimator sub-model. The estimation of the in-cylinder temperature is a fundamental step for NOx model design. It is possible to choose among different types of models. The following list summarizes the common approaches:

- Three zones model –based on energy and mass conservation equations [10][30][31]
- Two zones model –based on energy and mass conservation equations [21]
- Algebraic relation – based on enthalpy balance [13]
- Algebraic relation –based on Gibbs energy minimization for the species concentration estimation [14]
- Black Box

In a two zones model, the volume is subdivided in two parts which are homogeneous from a thermodynamically point of view: the unburned zone and the burned zone. Instead, in a three zones model the chamber is filled by:

- air from inlet valve closing to start of injection
- mixture of air-vapor of fuel from start of injection to start of combustion
- burned gas from start of combustion to the end of combustion

In each zone and for both approaches, mass and energy conservation equations are computed considering their dependence from time.

The heart of the model is the NOx model estimator which has the two previous sub-models as input. All the models presented in the literature can be developed with a non-integral approach or with an integral approach.

In a non-integral approach, the formed NOx mass per cycle is proportional to a function which has physical variables as input. The formula is not derived from a physical reason, but the values assumed from the tuning have to reproduce the actual physical relations among the input variables. The Arrhenius factor is often introduced in this kind of formulation. The general formulation is:

$$m_{NO_x} = k \cdot f\left(x_1^{k_1}, x_2^{k2} \ldots x_n^{k_n}\right) \qquad \begin{array}{l} k, k_1 - k_n \Rightarrow \textit{tuning coefficients} \\ x_1 - x_n \Rightarrow \textit{physical factors} \end{array} \qquad \text{Eq. 4.1}$$

D'Ambrosio at al. adopted a non-integral approach for their model where the amount of NOx is calculated with the following expression [4]:

$$m_{NO_x} = k \cdot e^{\frac{k_1}{T_{b\max,main}}} \cdot \alpha_{st}^{k_2} \cdot m_{fuel}^{k_3} \cdot N^{k_4} \cdot p_{rail}^{k_5} \qquad \text{Eq. 4.2}$$

In an integral approach model, a simple but physically motivated relation is defined for the function of integral in which the integral interval variable is the crank angle. The general formulation is:

$$m_{NO_x} = \int_{\alpha_1}^{\alpha_2} f(\alpha, x_1, x_2 \ldots x_n, k_1, k_2 \ldots k_m) d\alpha \qquad \text{Eq. 4.3}$$

$k, k_1 - k_m \Rightarrow$ *tuning coefficients*

$x_1 - x_n \Rightarrow$ *physical factors*

$\alpha \Rightarrow$ *crank angle*

The crank angle interval in which NOx forms is defined by α_1 e α_2. As an example of an integral approach, it can be shown the model proposed by Asprion at al. [5]:

$$n_{NOx} = \int_{\theta_{SOC}}^{\theta_{EVO}} V_{reac}(\theta) \cdot \left(r_{fw}(\theta) - r_{bw}(\theta)\right) d\theta \qquad \text{Eq. 4.4}$$

where the quantity of NOx results from the product between a "reaction volume" and an emission concentration.

For both approaches, the tuning coefficients can be map-based [k=f (N, load)] and must have a plausible physical motivation in order to have a model able to describe the combustion process correctly. The most common adopted algorithm for the coefficients estimation is the least square method. In Table 4.5, some parameters of semi-physical models found in the literature are summarized.

A grey box model is able to detect NOx deviations due to variations of the operating conditions with less calibration effort than a black box model. The in-cylinder pressure signal is adopted to calculate the heat release rate and MFB.

Table 4.5 Main results of Semi-Empirical or Grey Box Model

Author	**R^2**	**RMSE**	**Relative Error [%]**	**Computational Effort**
[4] D'Ambrosio	0.96	21 ppm	-	Few tens ms
[4] Gartner	0.90	28 ppm	-	-
[4] Krishnan	0.88	42 ppm	-	-
[5] Asprion	-	-	2.63-3.13	0.13 ms
[13] Grondin	-	-	20	-
[13] Querel	0.96	-	12	-
[13] Letellier -1	0.98	20 [%]	-	-
[13] Letellier -2	0.99	6 [%]	-	-
[16] Guardiola	-	-	15.21-17.71	0.9 ms
[19] Parka	0.98	-	9.3	-
[30] Hegarty	0.98	-	-	-
[42] Desantes	0.98	-	-	-

4.3 Physical model or White Box

A physical model is similar to the grey box model for the air path sub-models; but the in-cylinder process and NOx estimator sub-models are different. The heart of the NOx estimator sub-model is the resolution of the ordinary differential equation which is the physical model that describes the chemical kinetic of NOx reactions.

$$\frac{d[NO]}{dt} = \frac{2 \cdot R_1 \cdot \left\{1 - \left([NO]/[NO]_e\right)^2\right\}}{1 + \left([NO]/[NO]_e\right) \cdot \dfrac{R_1}{R_2 + R_3}} \qquad \text{Eq. 4.5}$$

This equation considers the Zeldovich mechanism only, but some authors use more detailed reaction scheme. The equilibrium concentrations of the chemical species involved in the equation are tabulated and are function of the pressure and temperature, while the rate of formation is expressed as Arrhenius factor:

$$R_1 = k_1^+ \cdot e^{\frac{\gamma_1^+}{T}} \cdot [O]_e \cdot [N_2]_e = k_1^- \cdot e^{\frac{\gamma_1^-}{T}} \cdot [NO]_e \cdot [N]_e \qquad \text{Eq. 4.6}$$

$$R_2 = k_2^+ \cdot e^{\frac{\gamma_2^+}{T}} \cdot [N]_e \cdot [O_2]_e = k_2^- \cdot e^{\frac{\gamma_2^-}{T}} \cdot [NO]_e \cdot [O]_e \qquad \text{Eq. 4.7}$$

$$R_3 = k_3^+ \cdot e^{\frac{\gamma_3^+}{T}} \cdot [N]_e \cdot [OH]_e = k_3^- \cdot e^{\frac{\gamma_3^-}{T}} \cdot [NO]_e \cdot [H]_e \qquad \text{Eq. 4.8}$$

where k and γ are tabulated.

For the estimation of the temperature, it is necessary to consider the "zone models" (three, two or multi zones models) as they were already presented for grey box models. The estimation of the in-cylinder temperature must be the most accurate possible. In particular, a single zone is able to predict only the heat release rate, thus it is compulsory to introduce at least another zone for the estimation of the NOx emissions. A white box model is able to predict the NOx concentration within 10% of relative error if the complete reaction scheme is resolved, but this result is not reached if the reaction scheme is reduced to the Zeldovich mechanism (relative error value of 60%). They are not indicated to be implemented for a real time application. The main result of some white box model are summarized in Table 4.6.

Table 4.6 Main result of Thermo-dynamic or White Box Model

Author	R^2	Relative Error [%]	Computational Effort	Zone
[10] Walke	0.88	47	-	2 Zones
[22] Maroteaux	-	6,5	-	2 Zones
[23] Ericson	-	-	0.25 s	2 Zones
[25] Johansson	-	20	-	2 Zones
[26] Mellor	0.885	-	-	1Zone
[26] Mellor	0.83	-	-	2Zone
[31][32] Finesso	0.94	3	0.5 ms	3Zones
[33] Egnell	0.78	35	-	Multi
[33] Egnell	0.94	34	-	2 zones

5. Development of the Model and Steady State Calibration

Due to its simple formulation and low computational effort, the model developed by Guardiola et al. results adequate for its best compromised between computational and calibration effort. [16][17] Therefore, it has been chosen as starting point from which an improved model has been developed.
In this Chapter, the description of the reference model and the steps done to improve it are described. In particular, the results of the steady state model calibration are presented.

5.1. Reference model description

The reference model estimates NOx engine out emissions via Zeldovich mechanism and via the "re-burning" process which describes the recirculation of NOx molecules in the spray. In this work, only the Zeldovich mechanism is considered. The reference model estimates the mass of NO_X emissions at engine out position on the exhaust line with the Eq. 5.1. It is a crank angle resolved model:

$$m_{NO_X} = \int_{\theta} HRR(\theta) \cdot K_1 \cdot \left(\frac{N}{2000}\right)^{K_2} \cdot exp\left(\frac{K_3}{T_{AD}(\theta)}\right) \cdot d\theta \qquad \text{Eq. 5.1}$$

in which HRR is the heat release rate,

n the engine speed,

T_{AD} the adiabatic temperature at which thermal NO_X is assumed to form and

K_1, K_2 and K_3 are the calibration parameters.

The model aims to describe the combustion evolution in a Diesel engine and the main hypothesis is that the combustion develops in stoichiometric condition and the heat loss due to radiative and convection mechanisms takes place on time scale higher than combustion itself. [9]
The equation Eq. 5.1 considers the NOx formation process as the product between a "thermodynamic reaction volume": $HRR(\theta) \cdot K_1 \cdot \left(\frac{N}{2000}\right)^{K_2}$ and a "magnitude": $exp\left(\frac{K_3}{T_{AD}(\theta)}\right)$ with which NOx are produced; both of them evolve in time and space. The "thermodynamic volume" is thought as the volume in which the combustion takes place. In order to describe it, the heat release curve can be taken in consideration because it is able to catch effect on the combustion due to calibration variation.

For the term that contains the engine speed, it is supposed that the time available for the reaction becomes shorter when the engine speed is higher.

The Arrhenius factor, $exp\left(\frac{K_3}{T_{AD}(\theta)}\right)$, derives from the kinematic equation. It represents the magnitude at which the reactions happen:

$$k = T^{\beta} \cdot exp\left(\frac{E}{R \cdot T}\right) \qquad \text{Eq. 5.2}$$

where β is the power of direct temperature relationship and R is universal gas constant. The term T^{β} is disregarded in the reference model –or incorporated in K_1- for simplicity sakes; E/R is condensed in K_3, that is the activation energy expressed in the unit of temperature.

The heat release rate can be computed applying the conservation laws:

$$HRR(\theta) = \frac{1}{\gamma - 1} \cdot \left(V_{cyl} \cdot \frac{dV_{cyl}}{d\theta} + \gamma \cdot p_{cyl} \cdot \frac{dV_{cyl}}{d\theta}\right) \qquad \text{Eq. 5.3}$$

where V_{CYL} and p_{CYL} are the instantaneous values of displaced volume and pressure respectively, and γ is the specific heats ratio of the charge. [9] It is compatible with ECU computational capabilities and accurate enough for the purposes of current study.

Finally, the adiabatic temperature is considered as the sum of three terms:

$$T_{AD} = T_{UB} + \Delta T_{ND} - \Delta T_{DISS} \qquad \text{Eq. 5.4}$$

where T_{UB} is the temperature of unburned gases

ΔT_{ND} is the temperature rise which stems from fuel oxidation

ΔT_{DISS} is the temperature variation due to dissociation effect

The temperature of unburned gases, T_{UB}, is calculated as function of in-cylinder pressure evolution and starting from the pressure at the IVC (intake valve closing) position via isentropic compression/expansion.

$$T_{UB} = T_{UB-1} \cdot \left(\frac{p_{cyl}}{p_{cyl-1}}\right)^{\frac{\gamma-1}{\gamma}} \quad \text{Eq. 5.5}$$

It is worth noting that, even if Eq. 5.5 is valid in adiabatic condition, the ratio of specific heat depends on temperature, but this variation is disregarded for sake of simplicity and a constant value is assumed in order to avoid iterative calculation.

ΔT_{ND} is the temperature rise due to fuel oxidation, without considering the variation of species specific heat with temperature or chemical dissociation at high temperature.

$$\Delta T_{ND} = 37630.5 \cdot \left(\frac{y_{O_2}}{3.48 \cdot \lambda}\right) \quad \text{Eq. 5.6}$$

where y_{O_2} is the molecular oxygen mass fraction at intake manifold (which depends on EGR rate and global equivalence ratio) and λ is the "relative fuel/air equivalence ratio".
Considering its physical meaning, ΔT_{DISS} is the function of temperature as heat capacity and dissociation effect are expected to increase as the chamber temperature rises; the reference paper uses a threshold value of 2600 K and an if-function defines the right ΔT_{DISS} expression:

$$if\ T_{UB} + \Delta T_{ND} < 2600\ K \quad \text{Eq. 5.7}$$

$$\Delta T_{DISS} = 1.554 \cdot 10^{-7} \cdot (T_{UB} + \Delta T_{ND})^{2.677}$$

$$if\ T_{UB} + \Delta T_{ND} > 2600\ K \quad \text{Eq. 5.8}$$

$$\Delta T_{DISS} = 7.136 \cdot 10^{-10} \cdot (T_{UB} + \Delta T_{ND})^{3.36}$$

5.2. Development of the model

In the following paragraph, the choices and steps of the developed model which improve the reference one are illustrated. The main differences deal with:

- Interval of integration
- Adiabatic temperature model
- Turbulence effect description in the model

This part of the study has been produced thanks to support of two master thesis works.

5.2.1. Interval of integration

The integral is computed, according to reference paper, starting at SOC (start of combustion) crank position; but no information is presented for the end of crank angle. Therefore, since NOx are formed during the diffusion combustion, it is possible to limit the interval of integration between MFB20 and MFB80.

The choice of MFB has an important advantage because they are stable values from the point of view of cycle-by-cycle variations, Figure 5.1: the heat curve exhibits plateau for crank angle values far from TDC (Top Dead Centre) and MFB values greater than MFB80 show significant cycle-by-cycle oscillations.

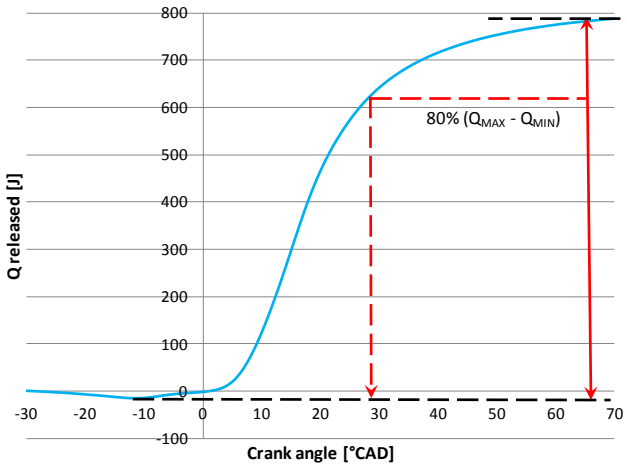

Figure 5.1 Graphic procedure for MFB80 calculation.

5.2.2. Improved adiabatic flame temperature model

The adiabatic temperature model is developed in an independent way from the reference model. Bearing in mind the adiabatic temperature model explained in the section 5.1, the first step is to investigate how to express the T_{AD} with a mathematical formula which catches the effect of EGR rate or O_2 mass fraction variations.

The adiabatic temperature is modelled as the sum of two contributions: temperature of unburnt gas T_{UB} and of ΔT_{ND} , which is the temperature rise due to oxidation:

$$T_{AD} = T_{UB} + \Delta T_{ND} = T_{UB} + \frac{LHV}{\sum_i n_i \cdot \overline{c}_{p,i}} \qquad \text{Eq. 5.9}$$

where LHV is the lower heating value per fuel mole unit.

n_i is the i-th chemical specie involved

$\overline{c}_{p,i}$ is the specific heat of the i-th chemical species of species involved.

The following section explains the procedure for the ΔT_{ND} computation. Details about the T_{UB} computation are already presented in section 5.1. For the ΔT_{ND} computation, the first step is to compute the intake air composition: n_i and, then, the specific heat of the i-th species. The main hypothesis is that the combustion is locally stoichiometric $\lambda = 1$, so in this conditions (i.e. considering the combustion of a stoichiometric O_2 molar quantity per unit mole of injected fuel), the local adiabatic flame temperature is evaluated considering: the impact of the dilution of the in-cylinder charge due to EGR-derived chemical species and the variation of the specific thermal capacity for the mixture species as a function of the gas. Moreover, It is supposed that the combustion reaction is complete. Tetradecane is generally used to shape Diesel molecule fuel, but first reactions consist of bonds breaking to form n-heptane:

$$C_7H_{16} + 11(O_2 + 3.76N_2) \rightarrow 7\,CO_2 + 8\,H_2O + 41.36\,N_2 \qquad \text{Eq. 5.10}$$

The amount of air at the exhaust is computed as the quantity of air that does not react with the fuel due to the lean combustion:

$$n_{AIR,RES} = (\lambda - 1) \cdot \alpha_{STOICH,MOL} \cdot n_{FUEL} \quad \text{Eq. 5.11}$$

where λ is the ratio between air and fuel mass

$\alpha_{STOICH,MOL}$ is, air moles that reacts stoichiometrically with one mole of fuel

$$\alpha_{STOICH,MOL} = \frac{n_{air}}{n_{fuel}} = \frac{11(1 + 3.76)}{1} = 52.36 \quad \text{Eq. 5.12}$$

Moles of CO_2, O_2, N_2, H_2O are easily derived from stoichiometry and volume concentration of oxygen in the air ($\chi_{O_2,AIR}$)

$$n_{CO_2} = 7 \quad \text{Eq. 5.13}$$

$$n_{O_2} = \chi_{O_2,AIR} \cdot n_{AIR,RES} = 0.21 \cdot n_{AIR,RES} \quad \text{Eq. 5.14}$$

$$n_{N_2} = \chi_{N_2,AIR} \cdot n_{AIR,RES} + 41.36 = 0.79 \cdot n_{AIR,RES} + 41.36 \quad \text{Eq. 5.15}$$

$$n_{H_2O} = 8 \quad \text{Eq. 5.16}$$

N_2 derives from both N_2 excess, via its volume concentration $\chi_{N_2,AIR}$, and the reacting air. Once that concentrations on exhaust side are known, moles in the intake manifold are determined. The oxygen entering the chamber comes from EGR and fresh air and it is possible to compute as:

$$n_{O_2,INTK} = n_{O_2,AIR} + n_{O_2,EGR} \quad \text{Eq. 5.17}$$

where:

$$n_{O_2,AIR} = \chi_{O_2,AIR} \cdot n_{AIR} = 0.21 \cdot n_{AIR} \quad \text{Eq. 5.18}$$

and n_{AIR} is calculated, considering global λ:

$$n_{AIR} = \lambda \cdot \alpha_{STOICH,MOL} \quad \text{Eq. 5.19}$$

For the computation of $n_{O_2,EGR}$ and $n_{N_2,EGR}$, it is assumed that the species are uniformly distributed in the exhaust flow: N_2/O_2 ratio does not change up- and down-stream of EGR valve. Uniform distribution of species is a simplification of the actual physics of the phenomena; but it allows to

calculate required data when no 3D model is available. So, if the amount of re-circulated molecular oxygen is known, also other species moles are evaluated:

$$n_{N_2,EGR} = \left(\frac{J}{n_{O_2}}\right)_{EXH} \cdot n_{O_2,EGR} \qquad \text{Eq. 5.20}$$

where $J = \{N_2, CO_2, H_2O\}$.In order to evaluate the amount of oxygen in the recirculated exhaust mass flow, an iterative method is used: a certain value of $n_{O_2,EGR}$ is the number of oxygen moles recirculated by EGR valve if y_{O_2} estimated by:

$$y_{O_2} = \frac{n_{O_2,INTK} \cdot MW_{O_2}}{n_{AIR} \cdot MW_{AIR} + n_{EGR} \cdot MW_{EGR}} \qquad \text{Eq. 5.21}$$

is in a tolerance band of the desired y_{O_2}. The desired amount of oxygen in the intake manifold is derived from the following analysis.

The oxygen concentration is a function of EGR rate and λ value at intake manifold. These engine parameters can be easily derived from the ECU.

Considering the simplified engine scheme in Figure 5.2, exhaust gas is composed by excess air, and products of combustion. K_L is the mass ratio between them:

$$K_L = \frac{m_{air,EO}}{m_{cg,EO}} = \frac{(\lambda - 1) \cdot \alpha_{STOICH} \cdot m_{FUEL}}{(\alpha_{STOICH} + 1) \cdot m_{FUEL}} = \frac{(\lambda - 1) \cdot \alpha_{STOICH}}{(\alpha_{STOICH} + 1)} \qquad \text{Eq. 5.22}$$

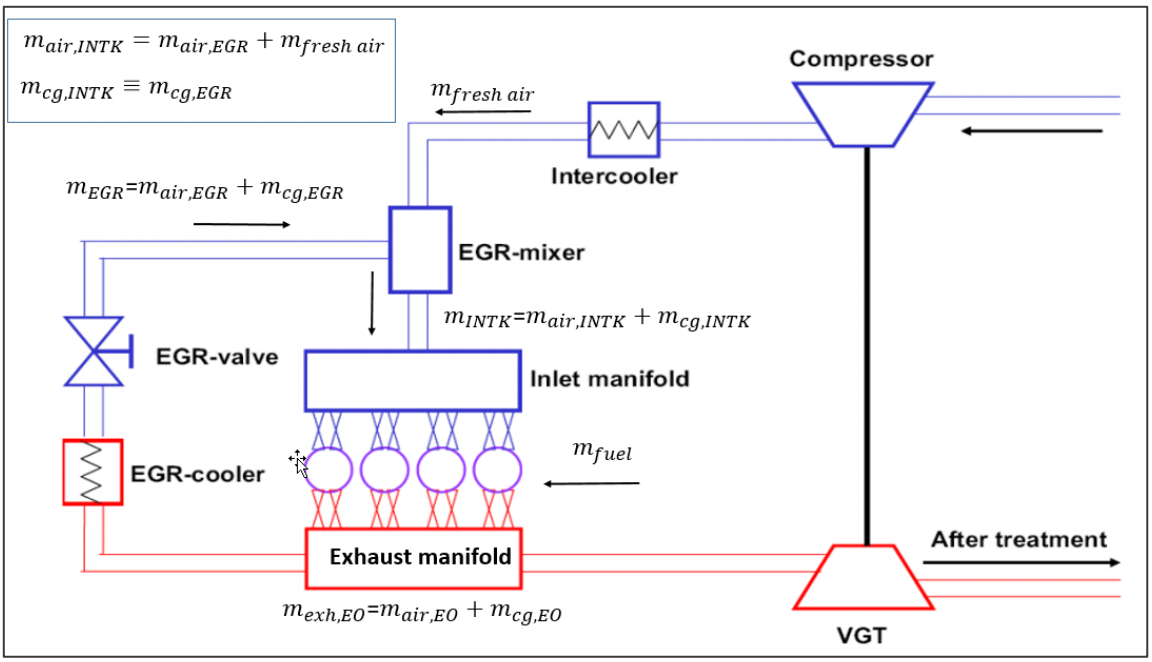

Figure 5.2 Main flows across the engine.

Provided uniform mixing between air and inert gases at engine out, K_L has the same value if m_{AIR} and m_{IG} are considered down line of the EGR valve:

$$K_L = \frac{m_{air,EGR}}{m_{cg,EGR}} = \frac{m_{air,EGR}}{m_{cg,INT}} = \frac{m_{EGR} - m_{cg,EGR}}{m_{cg,EGR}} = \frac{m_{EGR} - m_{cg,EGR}}{m_{cg,INTK}} \qquad \text{Eq. 5.23}$$

Also air mass in the intake manifold can be reformulated by K_L

$$m_{air,INTK} = m_{fresh\ air} + m_{air,EGR} = m_{fresh\ air} + m_{EGR} \cdot \frac{K_L}{K_L + 1} \qquad \text{Eq. 5.24}$$

where

$$m_{fresh\ air} = m_{INTK} - m_{EGR} \qquad \text{Eq. 5.25}$$

Substituting Eq. 5.23,Eq. 5.24 and Eq. 5.25 into the oxygen mass concentration definition

$$y_{O_2} = 0.23 \cdot \left(\frac{m_{AIR,INTK}}{m_{INTK}}\right) \quad \text{Eq. 5.26}$$

the final expression is

$$y_{O_2} = 0.23 \cdot \left[1 - rEGR \cdot \frac{\alpha_{STOICH} + 1}{\lambda \cdot \alpha_{STOICH}}\right] \quad \text{Eq. 5.27}$$

where 0.23 is the O_2 mass concentration in the air and the stoichiometric air/fuel equivalence ratio (α_{STOICH}) is 14.6. Apart from mathematical demonstration, Eq. 5.27 is reasonable: oxygen fraction depends only on air path variables, it reaches its maximum value (0.23) when EGR rate is equal to zero and decreases when EGR rate is increased. At the end of the code, when the Eq. 5.27 and Eq. 5.21 the agree to the same value, the EGR rate can also be estimated by molecular weights via

$$rEGR = \frac{m_{EGR}}{m_{EGR} + m_{fresh\ air}} = \frac{n_{EGR} \cdot MW_{EGR}}{n_{EGR} \cdot MW_{EGR} + n_{AIR} \cdot MW_{AIR}} \quad \text{Eq. 5.28}$$

After the intake chemical species computation, the computation of the specific heat is the next step. The main assumption is that there is a variation of specific heat with temperature, but the dissociation effects are disregarded as a first approximation.

Two different polynomial expressions are implemented to describe specific heat evolution with temperature, depending on the nature of selected compound (organic for fuel, inorganic for other species):

$$c_{p,FUEL} = \alpha + \beta \cdot T + \gamma \cdot T^2 \quad \text{Eq. 5.29}$$

$$c_{p,INORG} = \alpha + \beta \cdot T + \gamma \cdot T^{-2} \quad \text{Eq. 5.30}$$

For simplicity sake, mean values rather than exact expressions are introduced in the code:

$$\overline{c}_{P,FUEL} = \frac{1}{T_{AD} - T_{UB}} \cdot \left(\alpha + \frac{\beta}{2} \cdot T^2 + \frac{\gamma}{3} \cdot T^3\right)\Big|_{T_{UB}}^{T_{AD}} \quad \text{Eq. 5.31}$$

$$\overline{c}_{P,INORG} = \frac{1}{T_{AD} - T_{UB}} \cdot \left(\alpha + \frac{\beta}{2} \cdot T^2 + \frac{\gamma}{T}\right)\Big|_{T_{UB}}^{T_{AD}} \qquad \text{Eq. 5.32}$$

Provided a reaction like Eq. 5.10, T_{UB} represents the reactants temperature and T_{AD} is the temperature of the products. At this step, it is possible to compute the Eq. 5.9.

Note that T_{AD} is determined by iterative calculation:

- a guess value for T_{AD} is hypothesized ($T_{AD,GUESS}$)
- the specific heat of species involved in the reaction can be calculated via Eq. 5.31 and Eq. 5.32, so that the value of the expression on the right side of the equals sign in Eq. 5.9 is derived
- if T_{AD} resulting from Eq. 5.9 agrees with $T_{AD,GUESS}$ then the latter is the solution of the equation, otherwise a new guess value is assumed for $T_{AD,GUESS}$ via bisection method.

Figure 5.3 shows the comparison between the term ΔT_{AD} when the EGR rate and the coefficient λ are changed. The main physical trends are reproduced: for fixed λ value, if the EGR rate increases, the adiabatic temperature decreases because fresh air is gradually replaced by inert gases, so that there are less oxygen molecules and charge heat capacity increases.

For a fixed value of EGR, the heat capacity of the in -cylinder charge decreases due to an decrease of the amount of CO_2 and H_2O in the in-cylinder charge. This leads to an increase of the adiabatic temperature.

Finally, if the rate of EGR is equal to zero, the highest temperature is reached for any "global value" of λ.

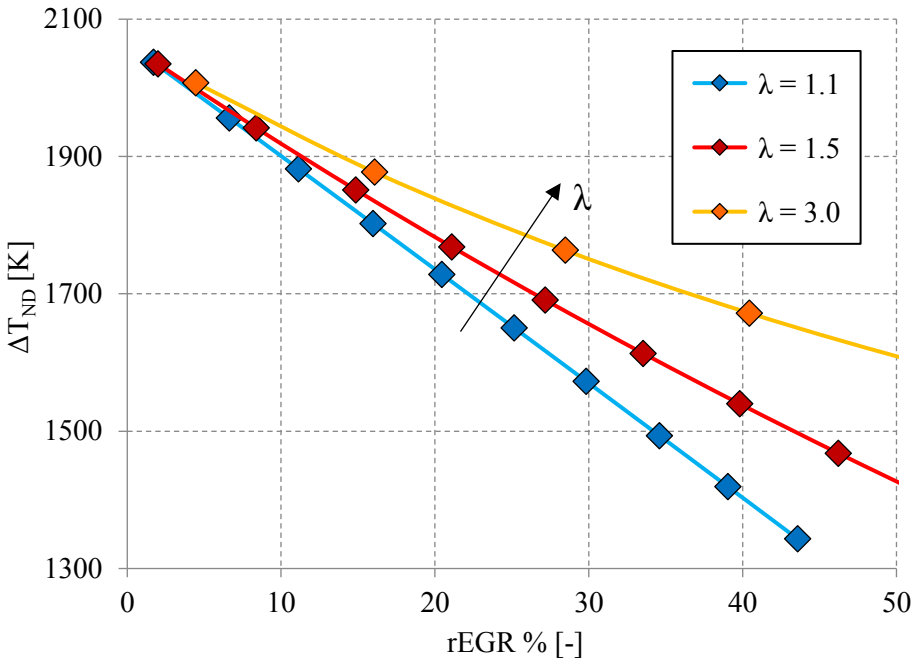

Figure 5.3 Temperature trend with respect to EGR valve opening when λ is varied.

The explained model introduces a high computational effort. Therefore, it has been developed a black box in ASCMO. ASCMO (Advanced Simulation for Calibration, Modelling and Optimization) is a commercial tool by ETAS for modelling the input/output behaviour of unknown systems. This data-based modelling is necessary whenever a precise physical description of the system is not possible. The high model quality, that can be achieved with this method, allows the mapping of even complex relationships, such as the global behaviour of an internal combustion engine.

In the case in exam, T_{AD} is computed as a function of the temperature of unburned gases and of air path settings, represented by oxygen mass ratio and EGR rate. The fitting of the ASCMO model is good since RMSE = 3 K and $R^2 = 0.99976$.

The next steps are obtained considering the model composed by Eq. 5.1 and the adiabatic temperature model just described. Hereafter, it will be indicated as “base model”.

5.2.3. Improvement of the model: turbulence effect

The main aim of this work is to develop a model able to follow any variation of calibration parameters; but, as first step, it is necessary to check if the model is able to describe the effects caused by a restricted number of calibration parameters. A DoE measurement program is generated on a fixed grid of EOPs, where combinations of EGR rate and injection timing (Start of pilot Injection- SOI_P) are created around the base calibration set point values, Table 5.1. The selected variables are the ones which have the highest impact on NOx emission production as presented in Chapter 3 . Hereafter, this measurement plan is indicated as "partial DoE" to distinguish it from the "complete DoE", described in Table 5.6, which is characterized by a higher number of variated parameters. In particular, the set of measurements of the "partial DoE" is divided in two parts, one used for the model training, the other for the model testing. The division is performed by randomly selecting 50% of the measurement points for each EOP separately.

Table 5.1 Variation of operating parameters for DoE for base model calibration and steady state validation

Engine parameter	Unit	Variation range
Engine speed	[rpm]	1000…3000, step 500
Load (BMEP)	[bar]	1…10 (7 for 1000 [rpm]), step 3
EGR rate	[%]	0…nominal calibration + c.ca 5
Inj. Timing (SOI_P)	[°CAD BTDC]	±6 nominal calibration

The purpose of the calibration phase is to compute the value of the $\{K_1, K_2, K_3\}$ set. The calibration parameters have the duty to reduce the gap between the real combustion and the mathematical base formula. Therefore, an optimization function has to be used in order to compute the "right" K_i values able to reduce the difference between estimated and measured NOx. The Matlab *lsqcurvefit* function computes the $\{K_1, K_2, K_3\}$ set reducing the root mean square error between estimated and measured NOx. Results for both training data and test data of the base model are illustrated synthetically in Table 5.2.

Table 5.2 Base model performance in training and validation phase using data of the "partial DoE"

Parameter	Training	Test
RMSE [ppm]	70	90

RMSE [%]	24.8	28.6
R^2	0.91	0.86

The minimum accuracy value of 0.95 is not achieved and, thus, the obtained results can not be considered acceptable. Therefore, single variation tests of air mass, main injection timing and rail pressure for two different EOPs (1600×4 and 2000×6 [rpm× bar) are performed to understand which phenomena are not considered.

The training is conducted locally: for each EoP a set of tuned parameters $\{K_i\}$ is computed and, then, percentage errors are analysed. Starting from the single variation of the intake air mass, there is not a clear trend between NOx emission and the relative error when the intake air mass variation is considered in Table 5.3.

Table 5.3 Percentage errors related to measurements with air mass variations

EoP 1600x4 [rpmxbar]			EoP 2000x6 [rpmxbar]		
Intake air mass [mg/hub]	NOx [µg/strk]	Relative Error	Intake air mass [mg/hub]	NOx [µg/strk]	Relative Error
340.23 (nominal)	51.81	3.20%	432.3 (nominal)	68.45	-0.96%
580.38	395.82	1.35%	678.83	607.55	-0.43%
441.09	174.89	-14.21%	530.3	214.00	6.77%
298.58	27.16	6.67%	480.32	128.65	-3.92%
390.42	103.06	-1.47%	405.26	51.504	-19.09%

Data available how the rail pressure variation on the performance of the model does not indicate any relationship. However, the results are presented in Table 5.4.

Table 5.4 Percentage errors related to measurements with rail pressure variation

EoP 1600x4 [rpmxbar]			EoP 2000x6 [rpmxbar]		
Rail Pressure [bar]	NOx [µg/strk]	Relative Error	Rail Pressure [bar]	NOx [µg/strk]	Relative Error
724.9 (nominal)	51.81	3.20%	1099 (nominal)	68.45	-0.96%
625.049	45.04	15.70%	949.981	63.03	-1.27
824.977	53.99	0.06%	1250.03	78.88	-6.36%

The trend of the percentage error when SOI_p gives the percentage error overcomes the fixed requirement of 10% relative error and it has a parabolic trend for the EoP 1600x4 and a linear trend for the EoP 2000x6. The highest error occurs close to the TDC and it gets lower if the injection takes place later.

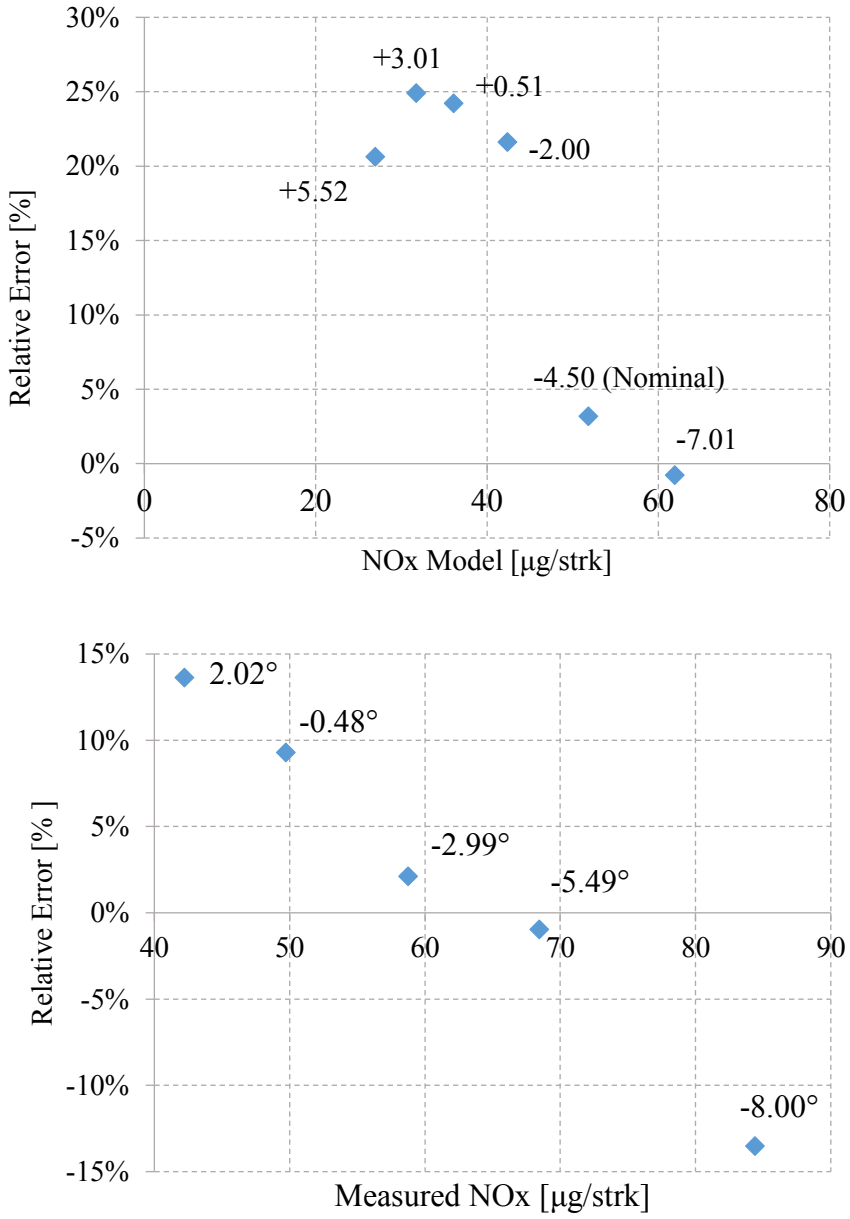

Figure 5.4 Percentage errors related to measurements with SOI variation for EOPs: 1600x4 *(up)* and 2000×6 *(down)* [rpm×bar]

When the injection occurs close the TDC, the mixing process is determined by the injection pressure and is amplified by the squish movement. If the injection is delayed, the mixing process is influenced by the rail pressure, but the effect of the squish movement can be negligible. Therefore, it is necessary to introduce a term able to distinguish if the injection is close to TDC or not. Since turbulence can be related to the kinetic energy, the squish velocity is a right candidate to model the turbulence caused by the piston movement. In literature [9] the following expression is proposed to describe the squish velocity as function of some geometrical parameter:

$$\frac{v_{sq}}{S_p} = \frac{D_B}{4z}\left[\left(\frac{B}{D_B}\right)^2 - 1\right]\frac{V_B}{A_C z + V_B} \qquad \text{Eq. 5.33}$$

where V_B is the bowl volume

A_C is the cylinder section area

S_p is the instant piston velocity

Z is the distance between the cylinder head and the piston

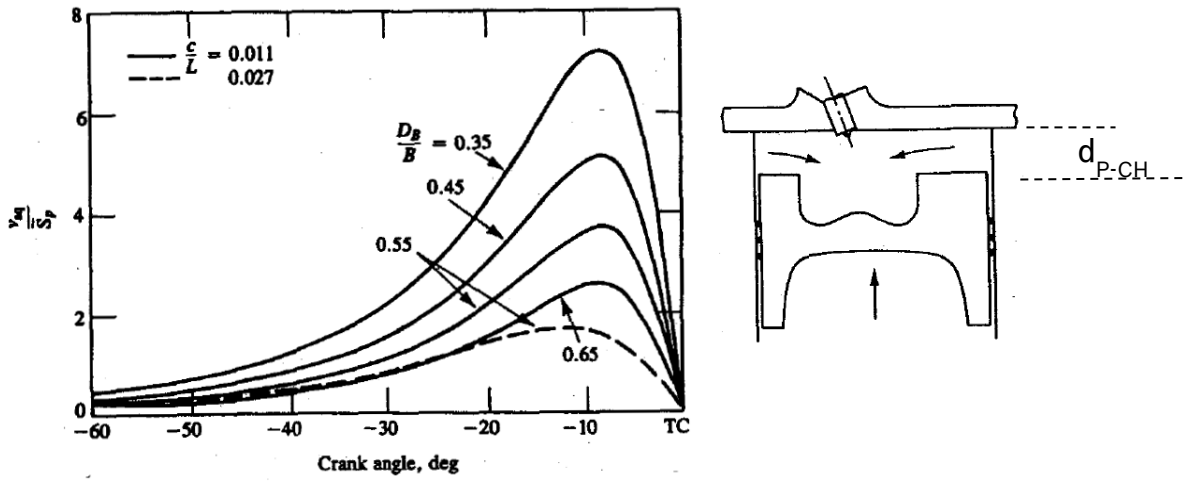

Figure 5.5 On the right, squish motions, coupled with piston stroke, are represented. On the left, theoretical squish velocity divided by mean piston speed is represented [9]

It is necessary to get a simpler mathematical expression for the implementation in the ECU due to its low computation capability. The squish velocity is proportional to the piston velocity S_p and to the reciprocal of the distance between the cylinder head and the piston Z:

$$v_{SQU} \propto \frac{S_p}{z^2} \sim \frac{S_p}{z} \propto \frac{dV_{CYL}(\theta)}{d\theta} \cdot \frac{1}{V_{CYL}(\theta)} \qquad \text{Eq. 5.34}$$

Eq. 5.34 is derived considering that piston speed depends on swept volume and d_{P-CH} is proportional to instantaneous volume. Associating squish to volume, its derivative is useful because their values are available in modern ECUs and their dependency is expressed by a dimensionless ratio.
This sub-model of turbulence is introduced in Eq. 5.1 so that the final expression is:

$$m_{NO_X} = K_1^* \cdot \int_{\theta} HRR(\theta) \cdot \left(1 + \frac{|dV_{CYL}(\theta)|}{V_{CYL}(\theta)}\right)^{K_4} \cdot \exp\left(\frac{K_3}{T_{AD}(\theta)}\right) \cdot d\theta \qquad \text{Eq. 5.35}$$

Modulus of volume derivate, $dV_{CYL}(\theta)$, is considered in Eq. 5.35 because the flow direction is not of interest; but it is considered the capacity to enhance the flame front volume. Therefore the reaction volume is $HRR(\theta) \cdot \left(1 + \frac{|dV_{CYL}(\theta)|}{V_{CYL}(\theta)}\right)^{K_4}$. The introduction of the new parameter, K_4, is necessary because the new term is constant respect to the crack angle. In Eq. 5.35, the influence of engine speed on NOx formation is incorporated in K_1^*. The performance of Eq. 5.35 is represented in Figure 5.6: the proposed improvement is able not only to cancel the parabolic trend but also to reduce the percentage error. Also events with injections which occur "far" from TDC benefit from the introduced term. For these reason, the model as in Eq. 5.35 is called "improved model" in the next sections.

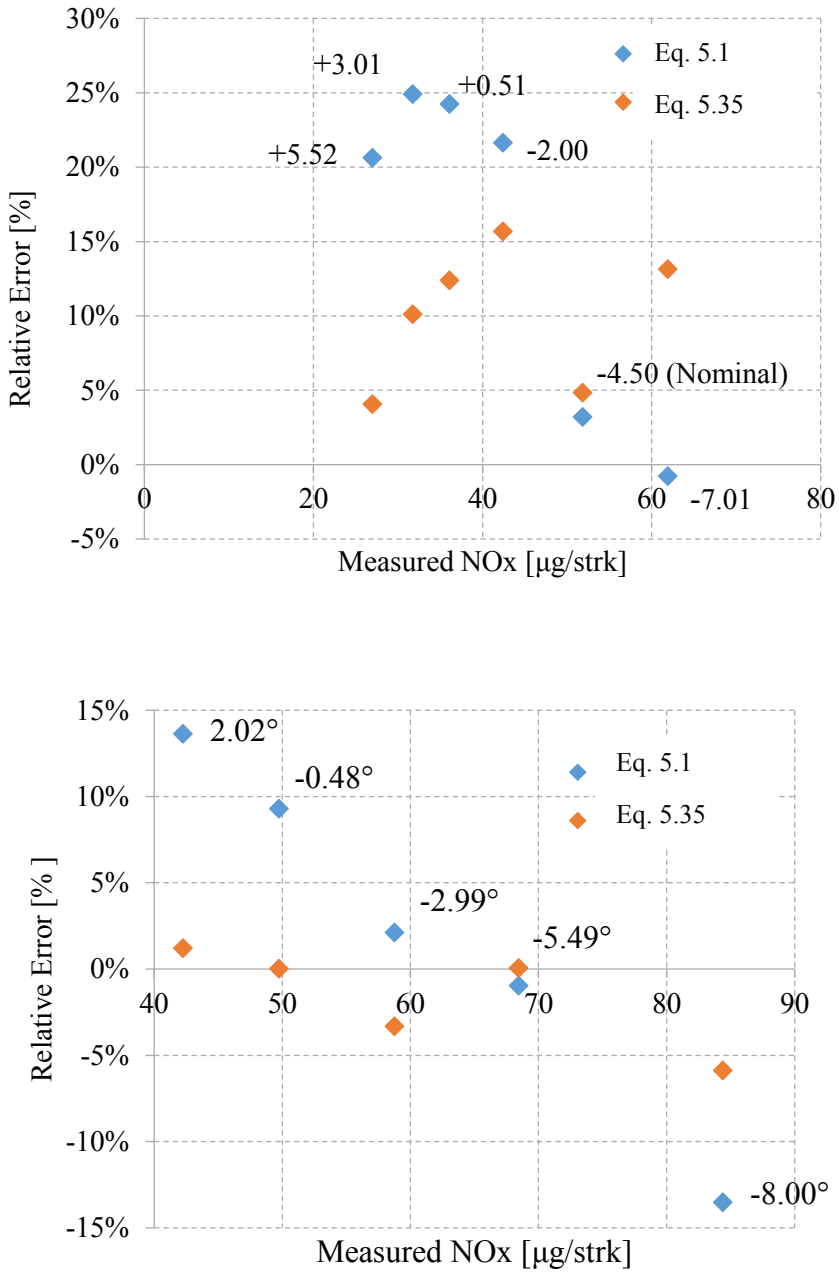

Figure 5.6 Comparison between base and improved model; labels are main injection timing in [° CAD BTDC].

5.3. Calibration on a partial DoE

The "improved model" is trained with the "partial DoE" -Table 5.1- to compare it with the base model. During the training phase, a local optimisation is used for the computation of K_1 and K_4 maps while K_3 has a constant value.

The statistical parameters, shown in Table 5.5, confirm the better performance achieved thanks to the term which describes the squish motion: the RMSE is reduced of 56% and R^2 is higher than the fixed required limit (0.95) in the validation phase. The improvement of the performance is achieved on all the EoPs as presented in Figure 5.7 and Figure 5.8 which show the absolute error over measured NOx for some DoE points when "base model" and "improved model" are used respectively.

Table 5.5 Comparison between base and improved model tested on the same experimental data.

	Base model - Eq. 5.1		**Improved model -Eq. 5.35**	
Parameter	**Training**	**Test**	**Training**	**Test**
RMSE [ppm]	70	90	37	39
RMSE % [-]	24.8	28.6	18.8	18.3
R^2	0.91	0.86	0.97	0.97

The "improved model" exhibits good performance as speed gets higher (most of the green points at 3000 rpm in Figure 5.8 have an error less than 10%). An explanation for this trend is that the new term formulation depends primary on piston speed and so the capacity to capture squish movements is better at higher engine speed. Moreover, the error increases as load (whatever the engine speed, squared points are outside the 20% error line) because, as already written in Chapter 3, there is a higher variability of produced NOx for high load than for low loads which allows a better accuracy.

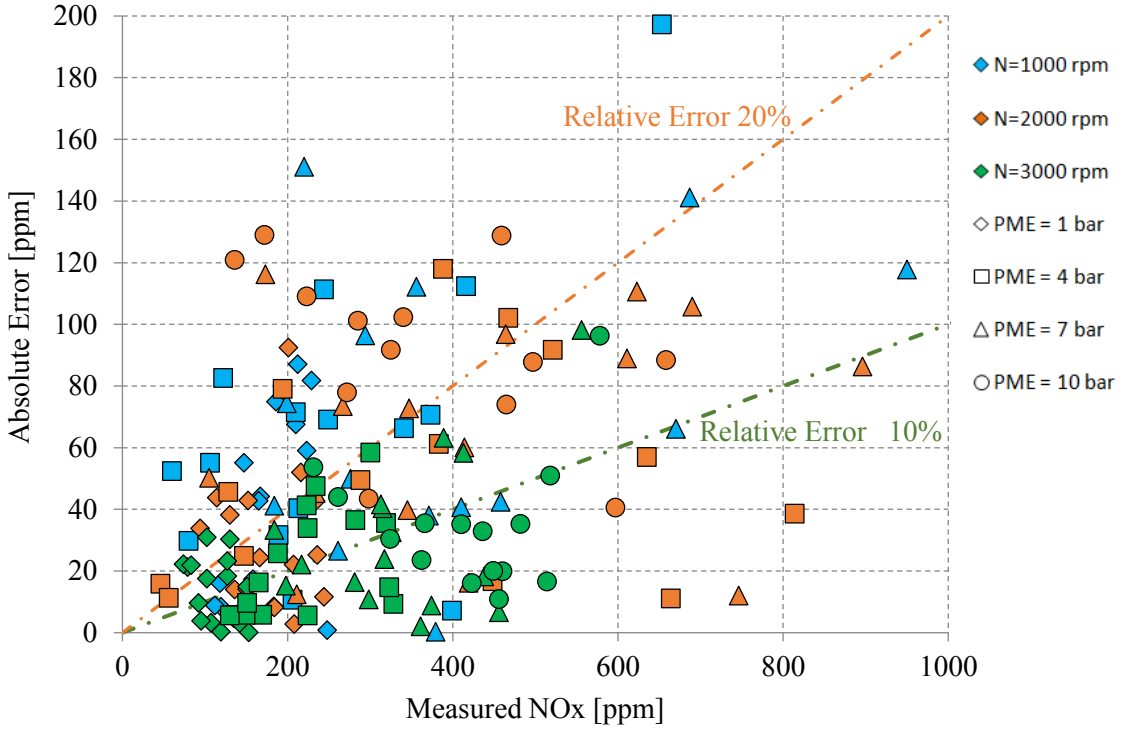

Figure 5.7 Base model prediction in validation phase on experimental data of the "partial DoE"

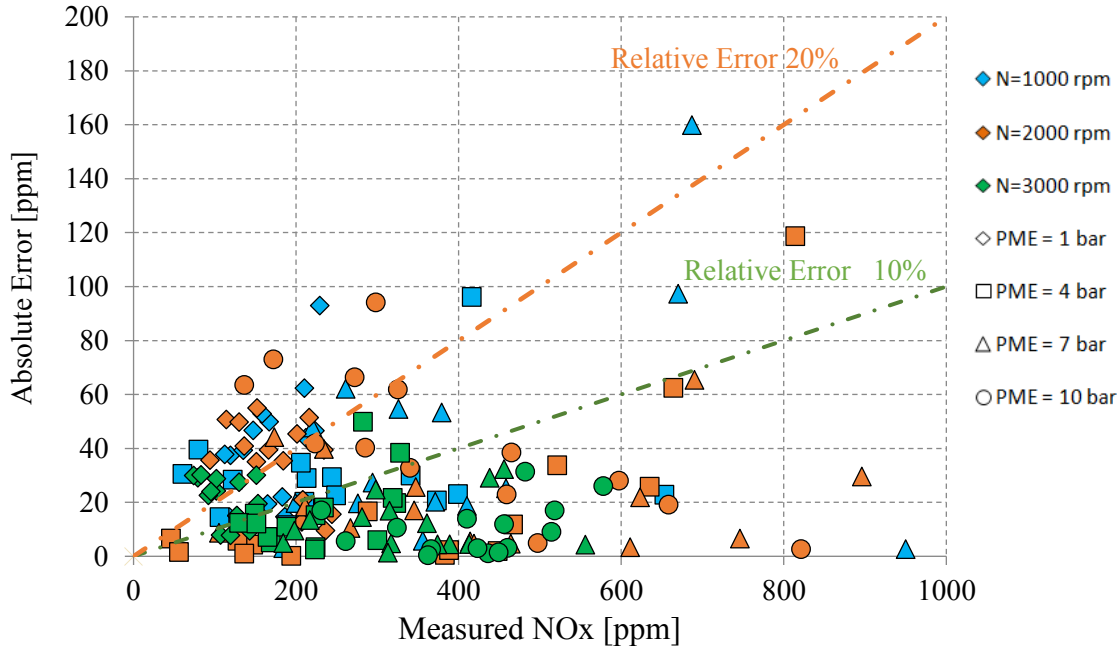

Figure 5.8 Improved model prediction in validation phase on experimental data of the "partial DoE"

5.4. Calibration on a complete DoE

The calibration of the "improved model" is conducted on the "complete DoE" to evaluate model capability in predicting NOx production when variations on fuel and air path are imposed. Then, a preliminary validation on nominal EoP and a final validation on dynamic standard cycles are conducted.

Table 5.6 shows the setting which characterizes the "complete" DoE. For all the imposed variations and for some EoPs, the inferior limit has a more stringent value than the one written in Table 5.6, if the declared value induces an unstable combustion. Looking the fuel parameters, the two pilot injections have the same quantity and their range is determined by experience. For each pilot injection, the maximum dwell time is fixed in correspondence of a delta of 8° in the injection advance while the main injection timing is limited because of the realization of combustion instability.
Boost pressure and air mass quantity are dependent on EOP considered. The variation of these two parameters is defined between the variables value in nominal calibration and the limit value established in a preliminary phase in which the condition of unstable combustion is verified.

Table 5.6 "Complete" DoE parameter settings for improved model calibration.

Engine parameter	Unit	Variation range
Engine speed	[rpm]	1000…3000, step 500
Load (BMEP)	[bar]	1…13 (7 for 1000 [rpm]), step 3
Pilot 1/Pilot 2 dwell time	[μs]	500 (min value) / t_{max} ($\Delta\theta = 8°$)
Pilot 1/Pilot 2 quantity	[mg/hub]	1-2
Main timing	[°CA BTDC]	± 6 nominal calibration
Rail Pressure	[bar]	± 200 nominal calibration (200 as inferior limit)
Boost Pressure	[mbar]	± 100 nominal calibration (1000 as inferior limit)
Air mass quantity	[mg/hub]	Qmax (EGR rat. = 0%) Qmin (EGR rat. = nom.+ 5%)

In Figure 5.9, the correlation between the estimated and measured NOx is shown: a good trend fitting line is noted because the R^2 is higher than 0.95; but a noticeable underestimation appears at high NOx

levels which can be caused by an underestimation of the intake oxygen ratio. In Table 5.7, the main statistical parameters are summarized: the total average relative error is in line with the semi-empiric model performance available in literature. However, from Figure 5.10 Absolute error related to the value of NOx raw emissionsit can be read how the relative error exceeds 40% at low NOx emissions; this confirms how difficult is the development of a model able to estimate low NOx emission. In this case, the prediction is not acceptable because this EoPs operate in nominal condition which are the common driving EoPs.

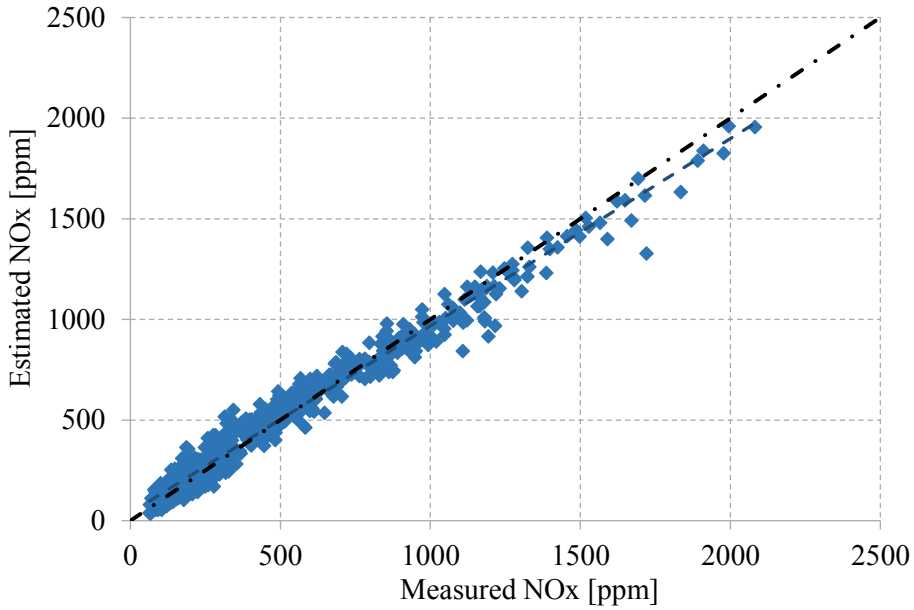

Figure 5.9 "Improved model" prediction calibrated on the "complete DoE".

Table 5.7 "Improved model" performance after the training phase on the "complete DoE".

Parameter	"Improved model"
RMSE [ppm]	69
RMSE [%]	21.84
Average relative error [%]	15.48
Relative standard deviation [%]	15.40
R^2	0.9702

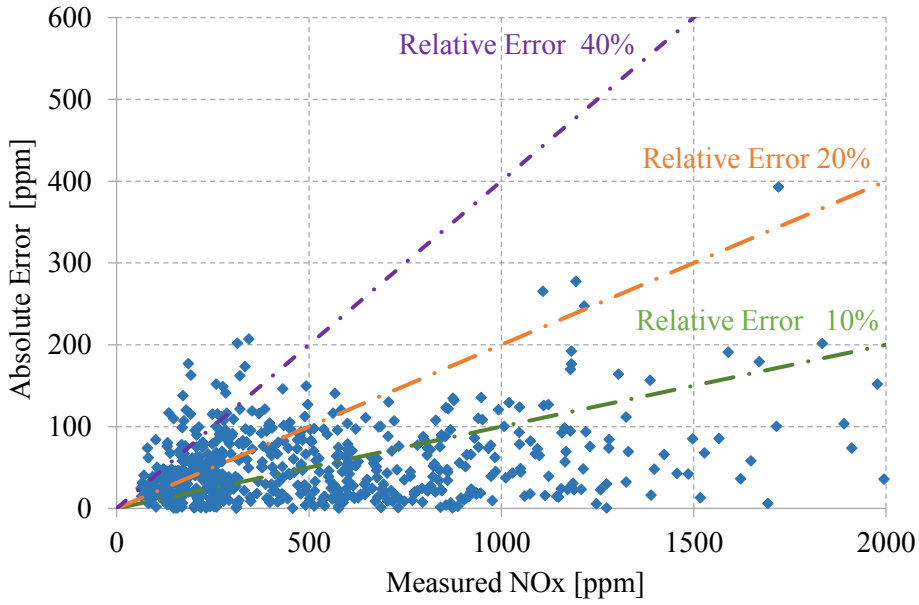

Figure 5.10 Absolute error related to the value of NOx raw emissions. Experimental data: "Complete DoE". Model: "Improved Model"

Once that K_1 and K_4 map and K_3 value has been evaluated, a preliminary validation is conducted giving as input a "mapping" with EGR. The aim of this kind of experimental measurements is to define engine behavior in nominal calibration. In particular, neither air or fuel variation are conducted in any EoP Table 5.8 shows the adopted plan.

Table 5.8 Nominal condition parameter settings for a preliminary validation of the "improved model".

Engine parameter	Unit	Variation range
Engine speed	[rpm]	1000…3000, step 500
Load (BMEP)	[bar]	1…13 (7 for 1000 [rpm]), step 3

In this case, the trend fitting line of the plot in Figure 5.11 is worse than the trend fitting line of the calibration plot - Figure 5.9- and the dispersion of the dataset is more pronounced as R^2 and RMSE values confirm in Table 5.9 where the comparison between the calibration and preliminary validation is presented. The worsening of the prediction is highlighted by the total average relative error which is doubled in the preliminary validation phase and by the relative standard deviation which is increased. Moreover, an intense overestimation is clear at low NOx levels which characterized the EoPs of the preliminary validation phase as the comparison between Figure 5.11 and Figure 5.9

shows. This result suggests that information about the nominal condition are missed during the calibration phase.

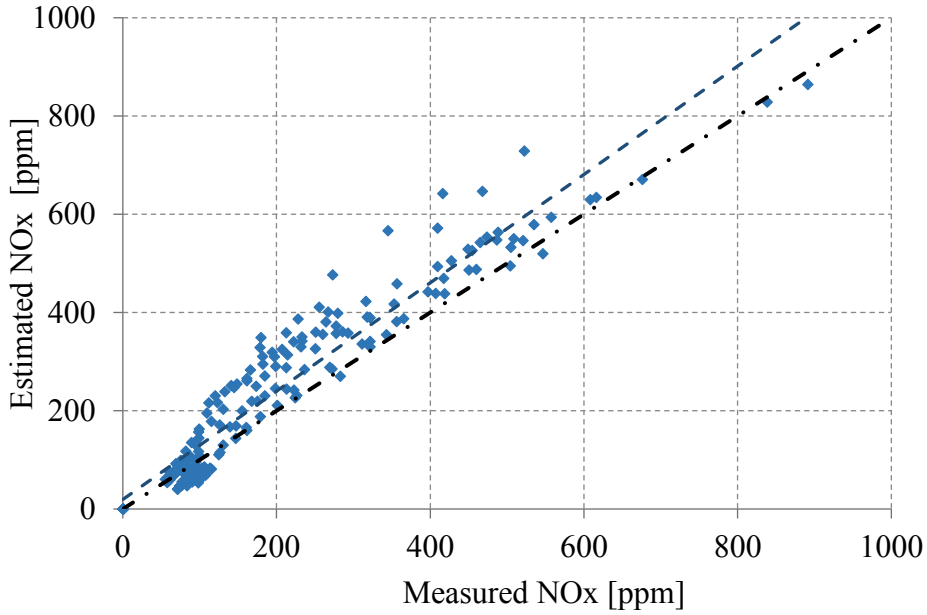

Figure 5.11 Preliminary validation of the "Improved model" conducted on mapping test

Table 5.9 Performance of the "improved model" in calibration and preliminary validation phases

Parameter	Calibration	Preliminary validation
RMSE [ppm]	69	74
RMSE [%]	21.84	37.48
Average relative error [%]	15.48	29.57
Relative standard deviation [%]	15.40	23.04
R^2	0.9702	0.9143

Finally, looking at the absolute error over the measured NOx in Figure 5.12, the relative error is not admissible because it exceeds 20 % up to 80%. In particular, this condition characterizes EoPs at low NOx emission and, then, high EGR rate values. This can be caused by a low accuracy of the oxygen rate at the intake.

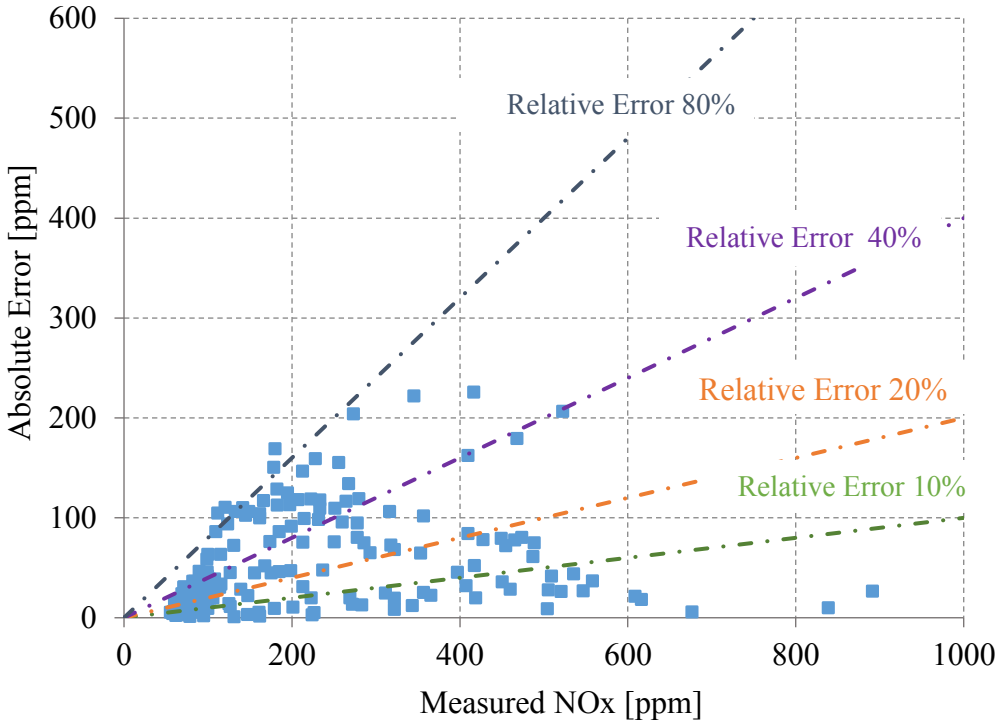

Figure 5.12 Relative error related to the value of NOx raw emissions. Measurements: "complete DoE". Model: "Improved model"

5.4.1 First approach: K_1 map recalibration

As a first attempt to address higher accuracy, a recalibration of the improved model has been computed with the following expression which consider the nominal condition as a reference condition:

$$K_{1,new} = K_1 \frac{NOx_{\ Meas}}{NOx_{\ Mdl}}\Big|_{nominal\ condition} \qquad \text{Eq. 5.36}$$

where $K_{1,new}$ is the new value for the K_1 map

$NOx_{\ Meas}$ is the measured NOx in nominal condition – mapping-

$NOx_{\ Mdl}$ is the estimated NOx in nominal condition –mapping-

K_3 value and K_4 are maintained. With the correction of the proportional parameter $K_{1,new}$, the high reduction of the error in nominal conditions is obvious as it is possible to see comparing Figure 5.11 and Figure 5.13.

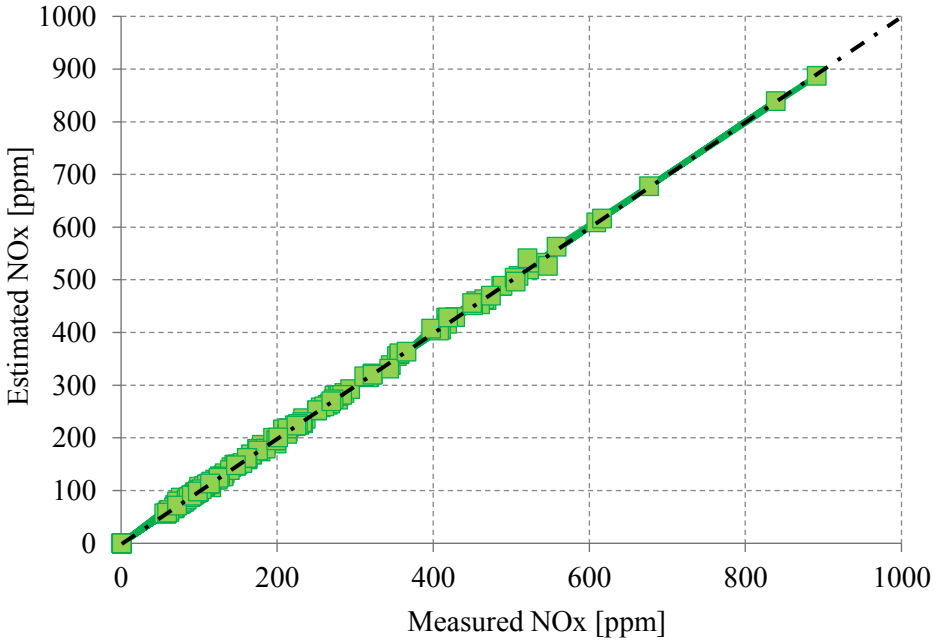

Figure 5.13 NOx estimation after K_1 recalibration, on mapping test with EGR. Model: "Improved model"

After K_1 recalibration, the model prediction is tested again on the "complete" DoE measurements of Table 5.6 "Complete" DoE parameter settings for improved model calibration. to verify if the model performance is improved. The trend fitting line is more distant from the bisector line, comparing Figure 5.9 and Figure 5.14. Modifying the proportional variable K_1, the angular coefficient of the tendency line is lower because the aim of the previous passage is to correct the overestimation in nominal condition.

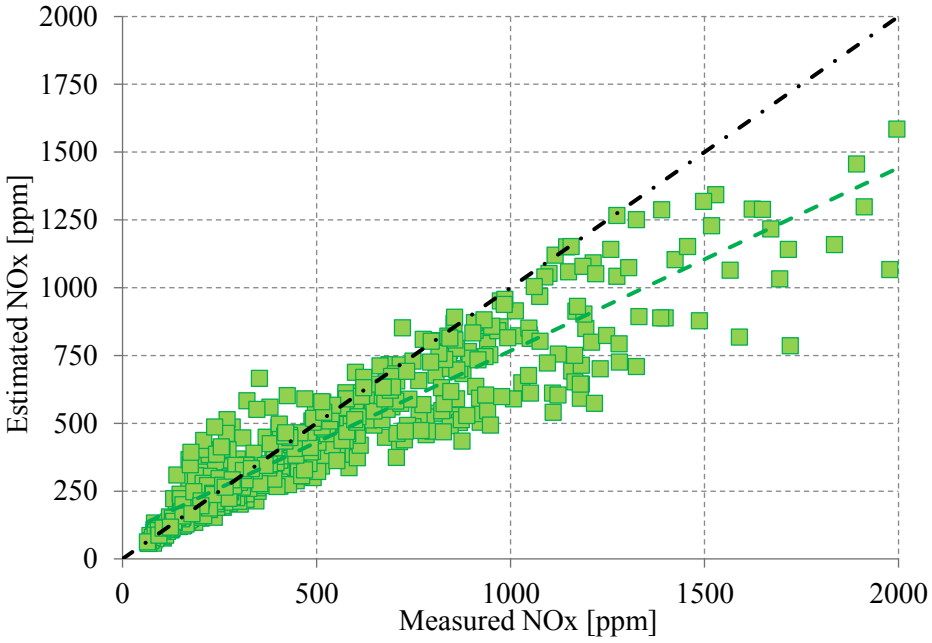

Figure 5.14 Improved model prediction, after K_1 recalibration, on the "complete DoE"

Moreover, a worsening of the dispersion cloud is registered, due to the high weight of K_1 in the NOx prediction formula. The ability of the model to estimate NOx is worsened globally: at high NOx levels the underestimation is such that the relative error reaches 80% and at low NOx emissions the overestimation is such that the relative error overcomes 40%. Results of this attempt are not satisfying as the comparison between the results before and after the recalibration confirms, Table 5.10. This approach increases the "weight" of the nominal condition information during the calibration phase reducing the capability of the model to predict NOx emission far from the nominal condition characterized by low EGR rate values.

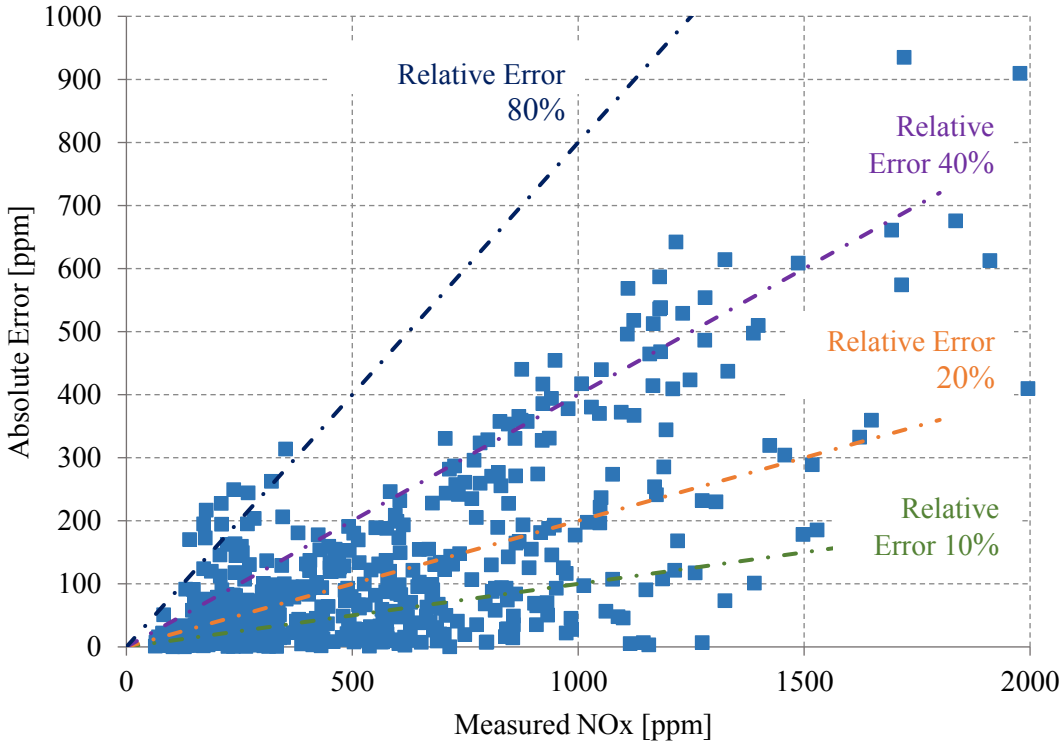

Figure 5.15 Absolute error related to the value of NOx raw emissions for data of the "complete DoE". Model: "improved model", after recalibration

Table 5.10 Statistic parameter, after and before K_1 recalibration, on experimental data of the "complete DoE"

Parameter	After K_1 recalibration	Before K_1 recalibration
RMSE [ppm]	182	74
RMSE [%]	27.15	37.48
Average relative error [%]	19.78	29.57
Relative standard deviation [%]	18.59	23.04
R^2	0.86	0.9143

5.4.2 Second approach: NOx model reformulation

The goal of reducing error not only in nominal condition, but in any other condition remained of primary importance. In fact, the "complete DoE" has been realized to test the prediction model capability in operating conditions different from the nominal calibration, that occurs during real operating conditions. As suggested in [5], a linear constrain is imposed between estimated and measured NOx:

$$\frac{m_{NOx}}{m_{NOx,ref}} = \frac{m_{NOx_{Mdl}}}{m_{NOx_{Mdl},ref}} \qquad \text{Eq. 5.37}$$

where m_{NOx} is the NOx production at the considered EoP

$m_{NOx,ref}$ stands for measured NOx at the nominal conditions.

$m_{NOx_{Mdl}}$ is the prediction delivered by the model for the considered EoP

$m_{NOx_{Mdl},ref}$ stands for the model prediction at the nominal conditions.

Therefore:

$$m_{NOx} = m_{NOx,ref} \cdot \frac{m_{NOx_{Mdl}}}{m_{NOx_{Mdl},ref}} \qquad \text{Eq. 5.38}$$

Combining expression Eq. 5.38 with the model according to equation Eq. 5.35, and considering that term K_1 was cancelled because both the nominal point and the considered conditions share the same engine speed and constants:

$$m_{NOx} = m_{NOx,ref} \cdot \frac{K_1 \int_{MFB\ 20}^{MFB\ 80} HRR(\theta) \left(1 + \frac{|dV(\theta)|}{V}\right)^{K_4} e^{\frac{K_3}{T_{AD}(\theta)}} d\theta}{K_1 \int_{MFB\ 20}^{MFB\ 80} HRR(\theta)_{ref} \left(1 + \frac{|dV(\theta)|}{V}\right)^{K_4} e^{\frac{K_3}{T_{AD,ref}(\theta)}} d\theta} =$$

$$= m_{NOx,ref} \cdot \frac{\int_{MFB\ 20}^{MFB\ 80} HRR(\theta) \left(1 + \frac{|dV(\theta)|}{V}\right)^{K_4} e^{\frac{K_3}{T_{AD}(\theta)}} d\theta}{\int_{MFB\ 20}^{MFB\ 80} HRR(\theta)_{ref} \left(1 + \frac{|dV(\theta)|}{V}\right)^{K_4} e^{\frac{K_3}{T_{AD,ref}(\theta)}} d\theta} =$$

$$= K_1{}' \cdot \int_{MFB\ 20}^{MFB\ 80} HRR(\theta)\left(1 + \frac{|dV(\theta)|}{V}\right)^{K_4} e^{\frac{K_3}{T_{AD}(\theta)}}\, d\theta \qquad \text{Eq. 5.39}$$

With $K_1{}'$ equal to:

$$K_1{}' = \frac{m_{NOx,ref}}{\int_{MFB\ 20}^{MFB\ 80} HRR(\theta)_{ref}\left(1 + \frac{|dV(\theta)|}{V}\right)^{K_4} e^{\frac{K_3}{T_{AD,ref}(\theta)}}\, d\theta} \qquad \text{Eq. 5.40}$$

As hereinafter, the expression in Eq. 5.39 will be referred as "new version" or v2 while the expression v1 is for Eq. 5.35. The introduction of the constrain needs the calibration of a new parameter, $K_1{}'$. It is a proportional factor as K_1, but $K_1{}'$ is fixed automatically once K_3 and K_4 are established in the first part of the training phase. In this way, one of the two degrees of freedom in the model, that characterized local influences of operating variables variation (fixed EOP), is substituted by a constrained parameter.

The implication Eq. 5.39 cancels any bias error between the NOx measured and modelled for the nominal condition because the two values match perfectly. In this case:

$$m_{NOx_{Mdl},ref} = m_{NOx_{Mdl}} \qquad \text{Eq. 5.41}$$

So:

$$m_{NOx} = m_{NOx,ref} \cdot \frac{m_{NOx_{Mdl},ref}}{m_{NOx_{Mdl},ref}} = m_{NOx,ref} \qquad \text{Eq. 5.42}$$

In particular, the calibration consists in the computation of K_3 and K_4 map using the measurement of the "complete DoE". Then the $K_1{}'$ map was calculated using Eq. 5.40.

In the following part of this dissertation, the computed maps are shown. They are calculated starting from the results obtained in Matlab. In order to reduce computational effort, due to the low number of reference points the map delivered by Matlab are not smooth. To overcome the problem, the final maps are computed with a different tool: Mapfit. Mapfit is a tool implemented in Excel that generates a map giving in input n reference points. For each point, values of x, y, z coordinates must be specified. Global continuity conditions on the map can be influenced directly through a smoothness

factor. Finally, an error analysis allows to understand the reliability of the interpolation carried out between the reference points. The analysis starts from the parameter K_4. It incorporates the amplification of the volume of reaction due to the charge bulk motion and it takes into account mainly the effect of main injection timing.

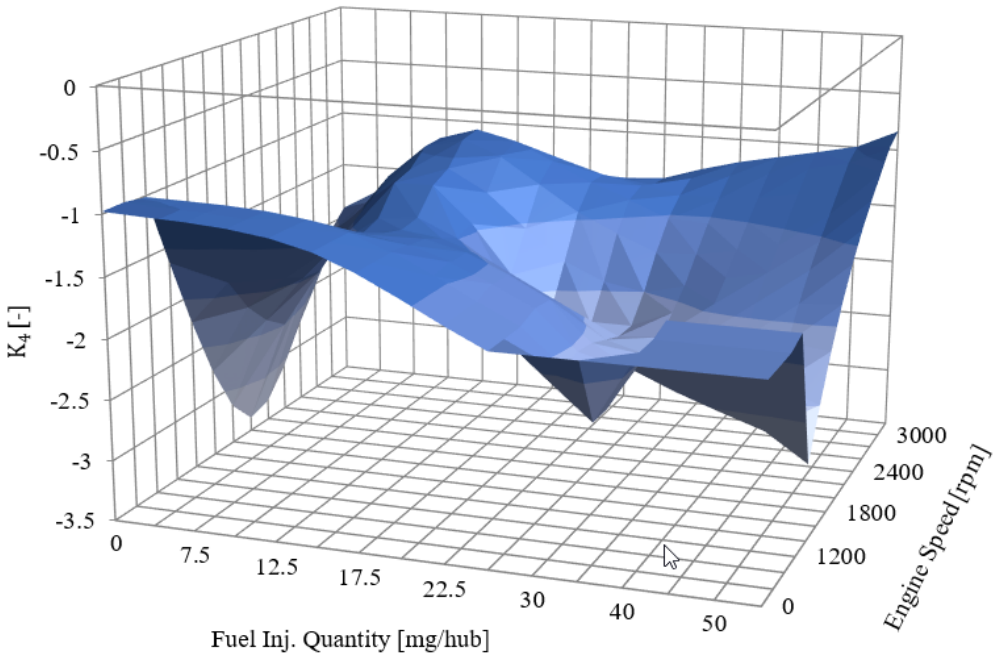

Figure 5.16 Map of parameter K_4

The coefficient K_3 is the activation energy and it should be negative as presented in the literature. In the first part of the development of the model, it is the result of a global training (section 5.4) while in this part of the work it is trained locally for a better adaptation of the mathematical formula on the experimental data. The K_3 map shows a higher variation range than K_4.

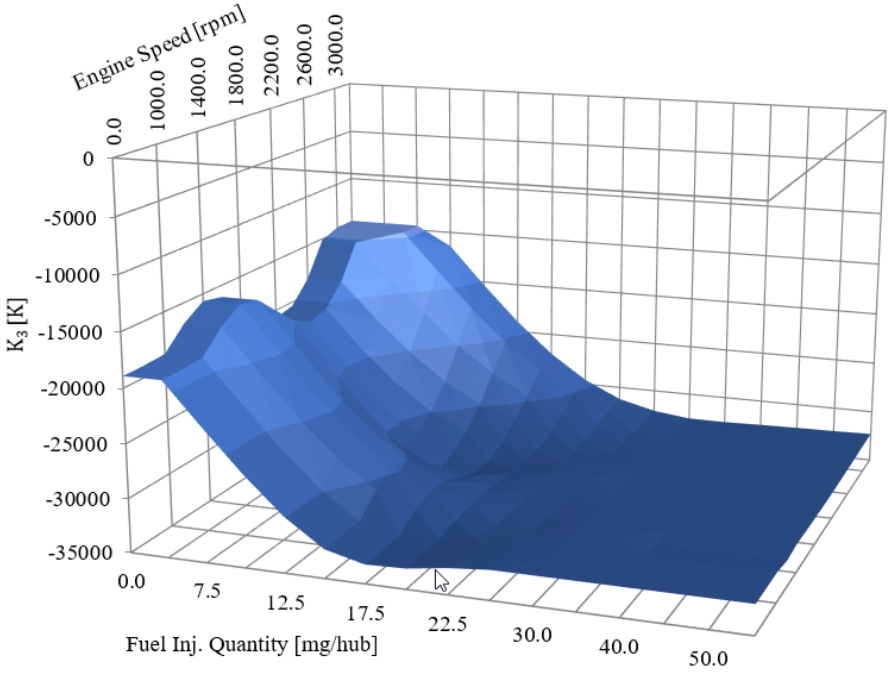

Figure 5.17 Map of parameter K_3

Finally, the parameter K_1' is related to the slope of the trend line in the plot where estimated and measured NOx are compared. It must be positive; but it should have the less wide range of variation in order to limit the interpolation error during the validation on dynamic traces.

Unlikely, resulting K_1' map is characterized by values quickly varying in the range of $10^{-1} \div 10^{8}$ ppm/mJ.

At this point, to have a smaller variation of K_1' and a smoother map it is necessary to limit K_3 values. In fact, K_1' variability depends on K_3 and K_4 variability. For each EOP, K_3 and K_1'influenced the shape and the slope of the trend fitting line respectively.

It is observed that limiting the minimum value of K_3 is reduced the maximum value of K_1'. So, different attempts are performed to choose a lower limit for K_3 that allowed to keep good performance.

The optimal range of K_3, is -14000 ÷ -32500 K , corresponding to K_1 values in the range 0,5 ÷ 800 ppm/mJ as can be seen in Figure 5.18.

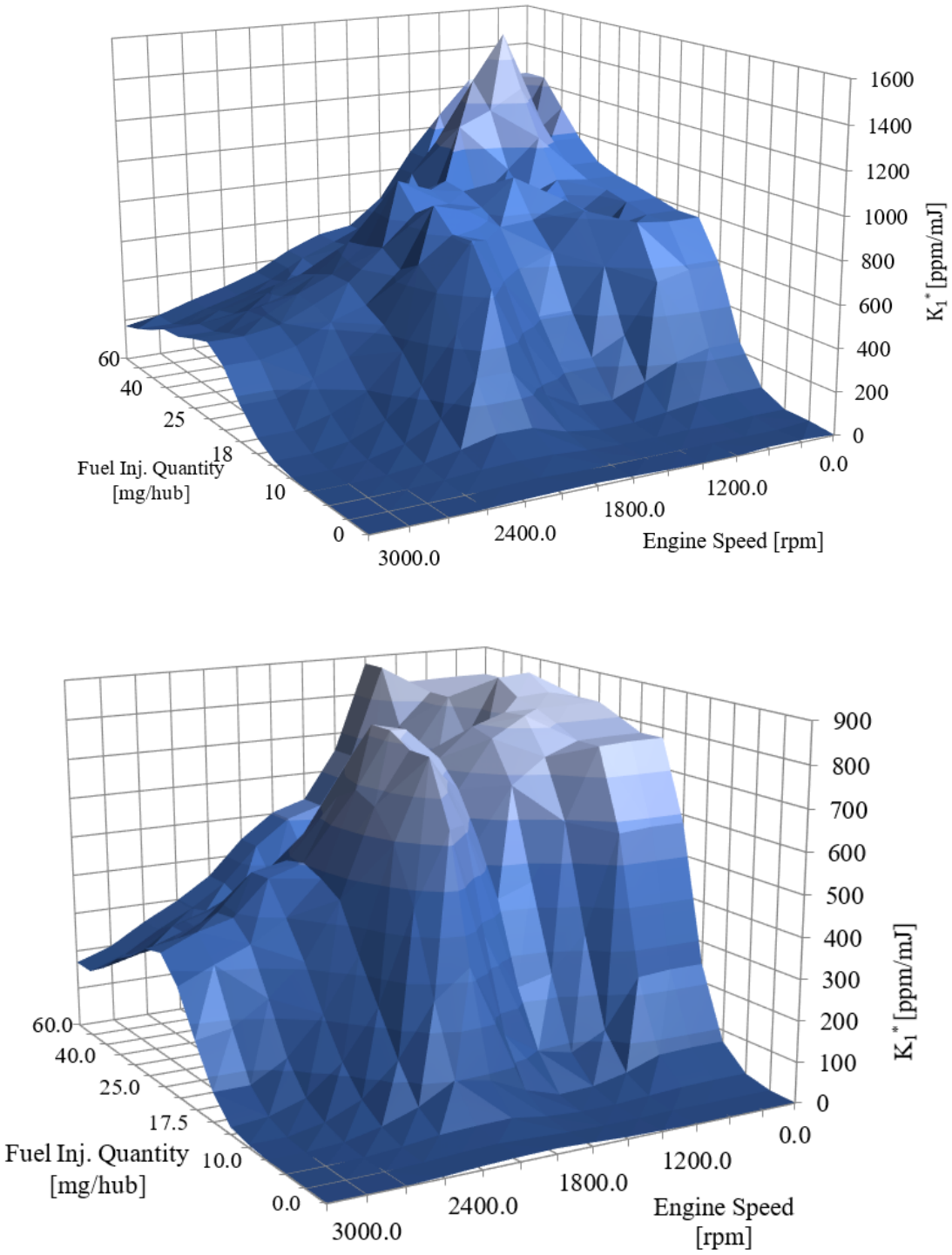

Figure 5.18 K_1' map before (a) and after (b) K_3 limitation

Performance of the new formulation in the training phase is shown below. In Figure 5.19, the trend line fitting is acceptable because the R^2 is 0.95. Comparing Table 5.10 and Table 5.11, it is clear that the new approach allows to reduce both relative average error and relative standard deviation so the 'cloud' is more concentrated around the bisector line. In this case, RMSE is higher in absolute value but in the relative form it has a lower value because major deviation occurred at higher NOx levels.

Moreover, at high NOx levels K_3 is saturated at -32500 K. So in conditions far from nominal calibration the only parameter K_4 is unable to describe the engine-out emissions variation thus relative error reaches 40%. The model, in the version v1, is more accurate at high NOx levels while the last formulation –v2- leads to more precise prediction at low NOx emissions as it appears in Figure 5.20 which shows the absolute error over measured NOx. Therefore, the model in the version v2 is the final version with which the dynamic validation will be conducted.

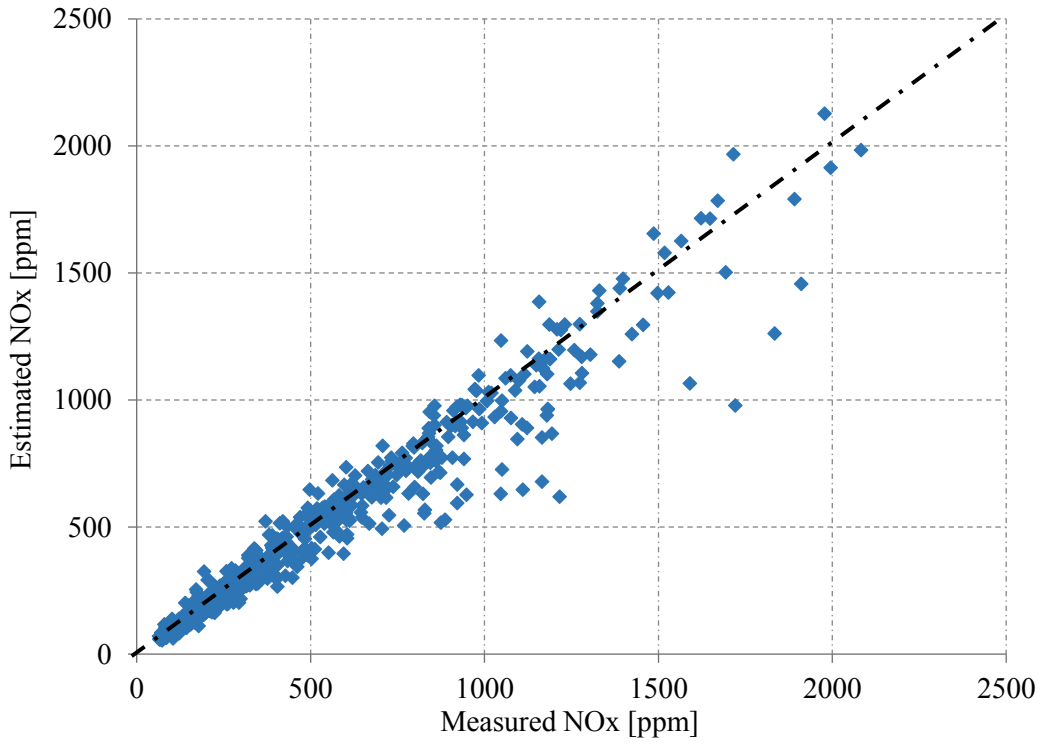

Figure 5.19 New model prediction on experimental data of the "complete DoE".

Table 5.11 New model performance in training phase on experimental data of the "Complete DoE".

Parameter	Model v1	Model v2
RMSE [ppm]	69	97
RMSE [%]	21.84	14.52
Average relative error [%]	15.48	10.78
Relative standard deviation [%]	15.40	10.05
R2	0.9702	0.95

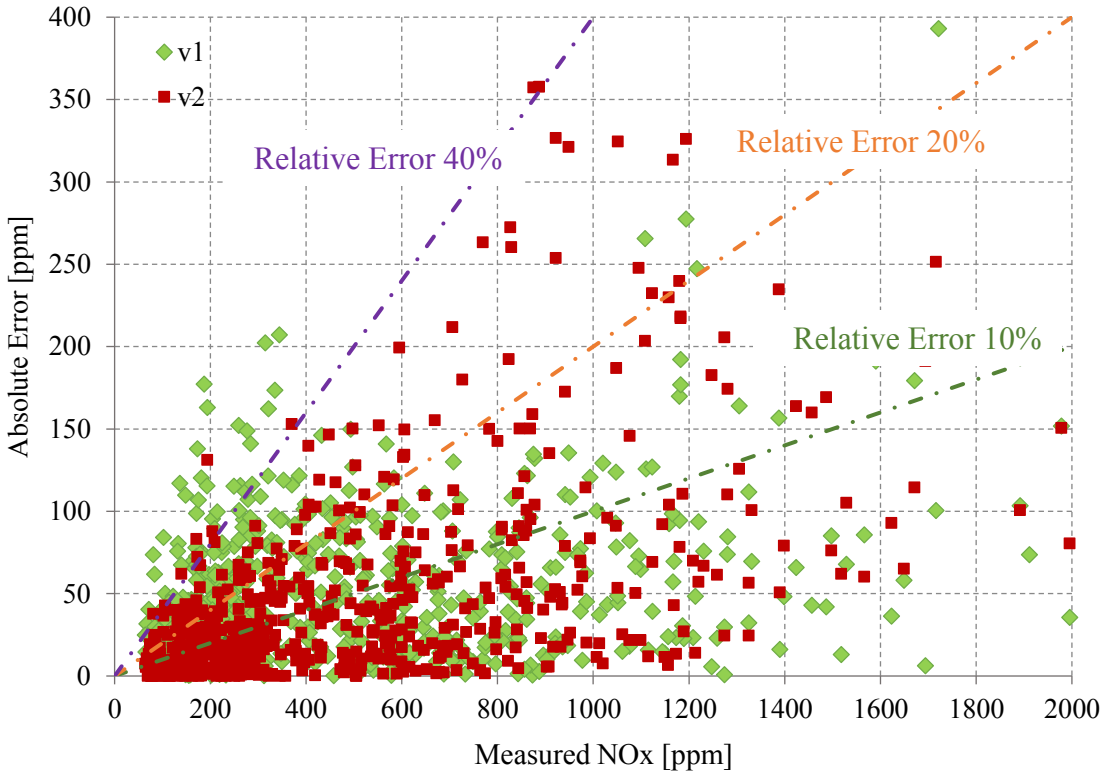

Figure 5.20 Comparison between relative error of model version v2 in red and model version v1

In Figure 5.21 as an example, the DoE points which composed the group 1000x1 [rpmxbar] are represented. The orange square surrenders the EoP in nominal condition: the version v2 cancels the bias error for this kind of EoP. Moreover, the dispersion around the bisector line is lower than in the case v1. From Figure 5.21, it is clear how the coefficient k_1^* affects the slope of the trend line.

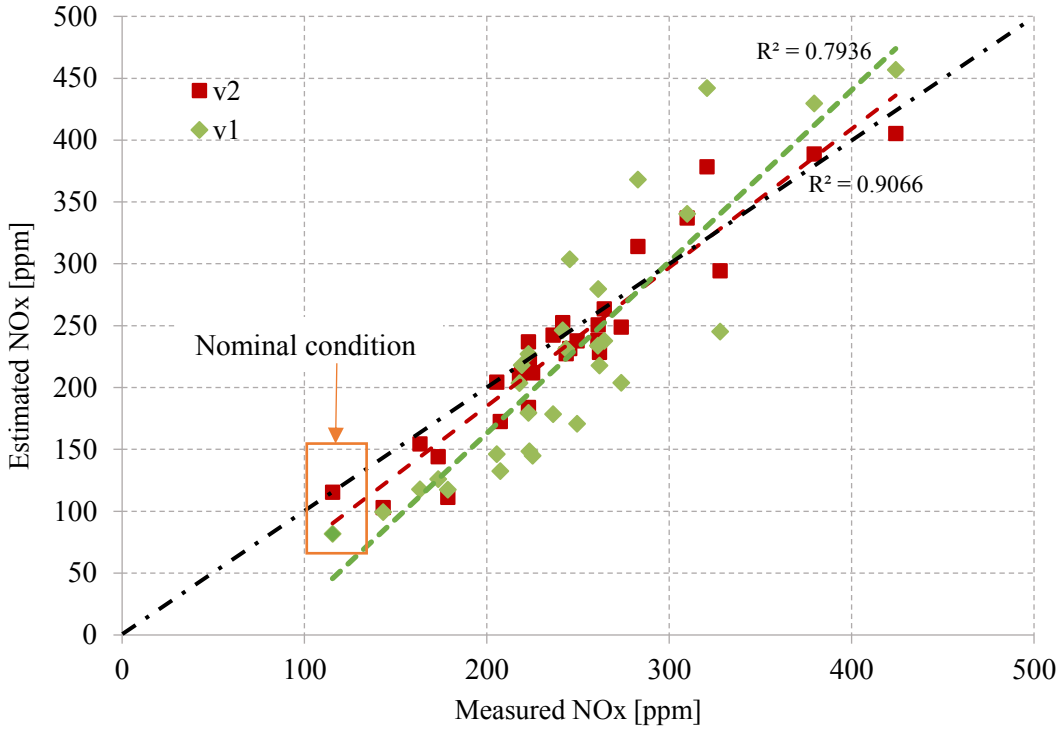

Figure 5.21 Example of NOx Estimation vs NOx Measured for EoP cloud of 1000x1 [rpmxbar]

The analysis between the relative error and each DoE input parameters is particularly useful. Looking in the details, there are not clear trends with one exception: the intake air mass flow. Figure 5.22(a) shows the results after the model training in the version v1 while Figure 5.22 (b) in the version v2. The shown DoE points are characterized by 2000 rpm and 10 bar. In the version v1, there is a reduction of the relative error when the intake mass flow increases –low EGR- that are EoP not so much frequent in a common driving. This trend disappears, if the version v2 is used for the training phase: the relative error is cut down for the EoPs with high value of EGR – low intake mass flow. The error, instead, is slightly increased for the DoE points far from the EoP in the nominal condition. This is the logical consequence of the new approach which is able to cancel the bias error in nominal condition and to make it "center of gravity" for all the DoE points of the considerate group. The same trend characterizes all the map and, then, the same consideration can be extended for them.

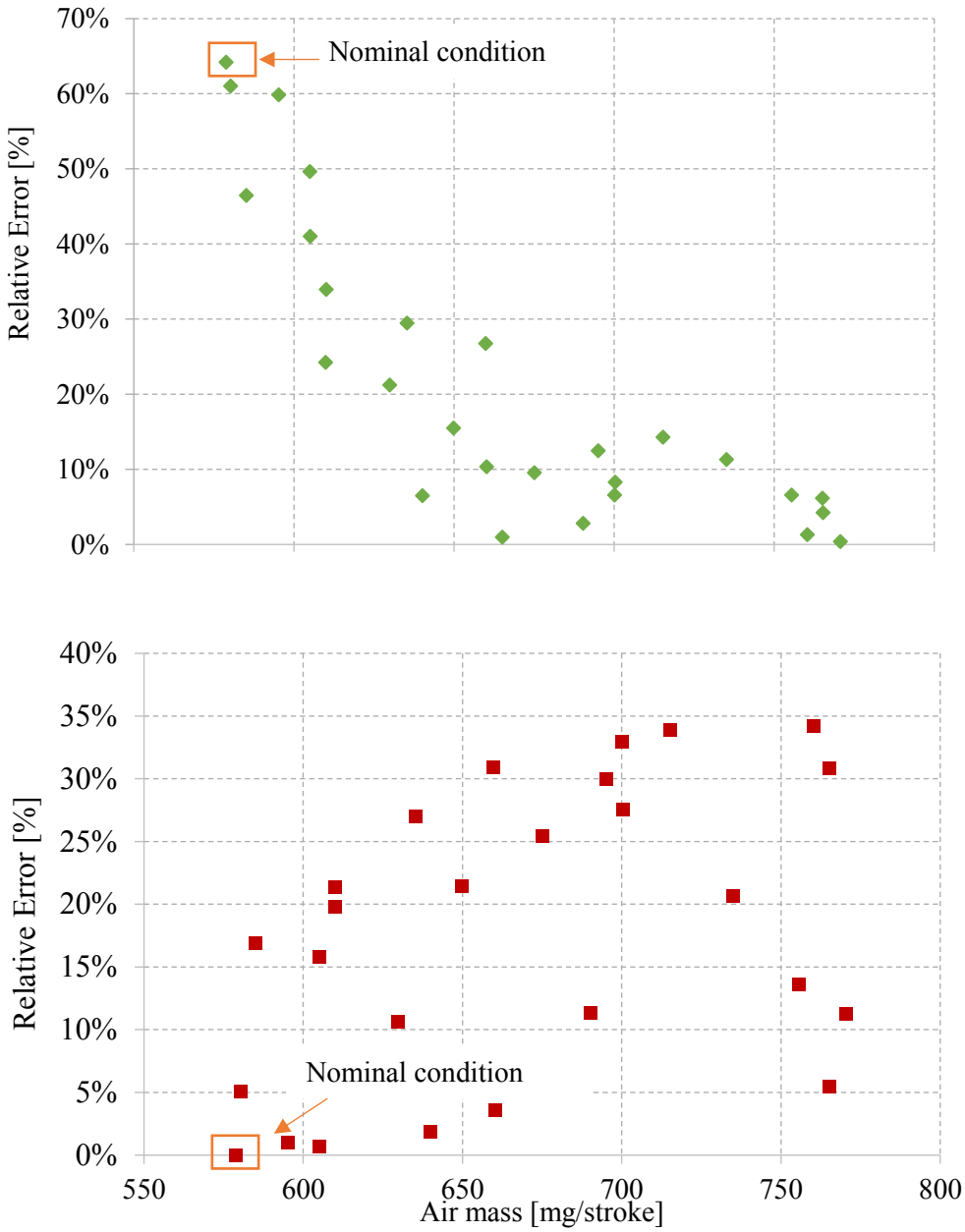

Figure 5.22 Relative error as function of air mass intake for EoP 2000x10 [rpmxbar] a) model version v1 and b)model version v2

6. Validation on Dynamic Standard Cycles

6.1 Preliminary Consideration

The model validation on dynamic cycles is a preliminary step to understand if the model is suitable for a real application. The model does not contain differential terms, but takes as input dynamic signals. Inputs of the model are different instantaneous signals, acquired by the measurement devices and monitored by the interface of the corresponding software. During test bench acquisition, data are monitored and stored by three software: INCA, IndiCom, AVL Puma as already described in Chapter 2. From IndiCom, the in-cylinder pressure signal is acquired. From INCA, the total quantity of injected fuel, fuel/air equivalence ratio in the exhaust pipe, O_2 mass ratio in the intake manifold (rO_2) –the only one that is estimated- and temperature in the intake manifold (T_{intk}) are obtained. In AVL Puma database, species of raw pollutants measured by specific analysers are recorded.
The engine speed (N) signal is recorded by all the three software. The IndiCom engine speed is used as a reference signal with respect to the other two engine speed signals so that they are shifted to have a coherent signal alignment. In this way the asynchronous start of the acquisition tools is corrected but another revision must be made. It has to take into account that emissions measurements are affected by a delay τ_{tot} as a result of:

$$\tau_{tot} = \tau_{meas} + \tau_{transp} + \tau_{mix} \qquad \text{Eq. 6.1}$$

where:

τ_{meas} is a constant response time typical of the instrument,

τ_{trans} is a variable delay due to gas transport through pipes from the engine to the sensor,

τ_{mix} is a variable delay due to gas mixing in volumes existing in the exhaust system.

The first and the second delay cause only a time-shift in the signals as illustrated in Figure 6.1a. The mixing delay determines a change in the shape of the real concentration curve instead, Figure 6.1b. Because of dilution phenomena, the measured concentration is characterized by a flattening and an 'enlargement' with respect to the original curve. Globally the areas under the two curves remain the same since the conservation of total amount of pollutant specie produced is valid.

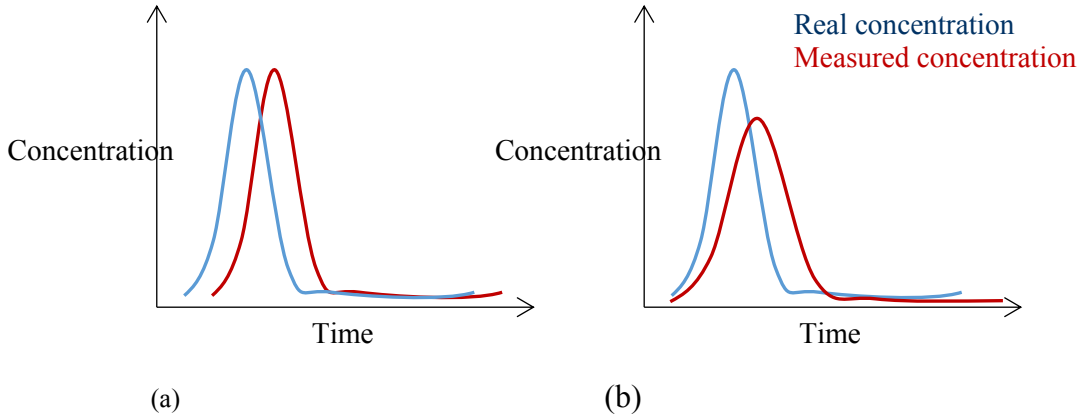

Figure 6.1 Comparison between real and measured concentration of pollutant specie considering: only transport effect (a) and mixing effect (b).

τ_{meas} is corrected simply comparing engine speed tracks. On the basis of the transport model, it is found that τ_{transp} is a function of flow rate of exhaust gas that are extracted and arrived at the measurement device as described in the following equation:

$$\tau_{transp} = \frac{L}{u} = \frac{LS}{uS} = \frac{V_{transp}}{\dot{q}} \qquad \text{Eq. 6.2}$$

Where L and S are the length and the section area of the pipe that the exhaust gas has to pass as illustrated in Figure 6.2.

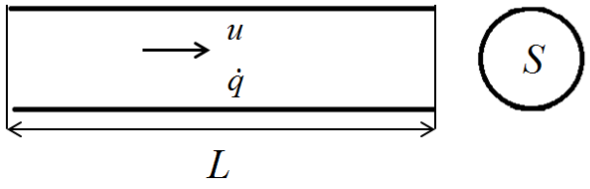

Figure 6.2 Simplified representation of the pipe that between engine and measurement device.

About mixing phenomena, it can be used a simplified model considering perfecting mixing in the passage volume and the absence of net storage. If c is the emission concentration, the two conditions result in the following equations respectively:

1. $c_{out} = c$
2. $\dot{q}_{in} = \dot{q}_{out} = \dot{q}$.

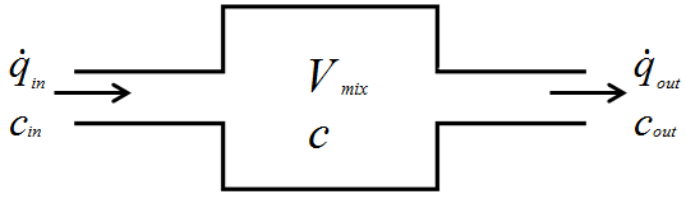

Figure 6.3 Simplified representation of mixing volume that the exhaust gas has to pass to arrive at the measurement device.

The continuity equation is:

$$V_{mix}\frac{dc_{out}}{dt} = \dot{q}_{in}c_{in} - \dot{q}_{out}c_{out} \qquad \text{Eq. 6.3}$$

The imposed conditions, Eq. 6.3 becomes:

$$\frac{V_{mix}}{\dot{q}}\frac{dc_{out}}{dt} = c_{in} - c_{out} \qquad \text{Eq. 6.4}$$

$$\tau_{mix}\frac{dc_{out}}{dt} = c_{in} - c_{out} \qquad \text{Eq. 6.5}$$

According to Eq. 6.1, the delay that must be corrected is different for NOx, CO, CO_2, HC. About NOx measured emission, both physical time associated to measurement device necessary to realize the measure and delay caused by transport process are considered constant and are deleted with two passages. The first consisted in applying the cross correlation between the quantity of fuel injected and CO_2. The general relationship, high NOx and CO_2 levels, is used to time align correctly NOx signal.

Besides on experimental results, it resulted that τ_{mix} has not a relevant effect on the measured NOx concentration and it is not considered in this case. In particular, Engine 1 is used to perform a WLTC cycle on the roller bench. In this occasion NOx emissions are measured simultaneously with a sensor mounted upstream SCR and with the analyser *HORIBA Mexa 7200 D* through an exhaust gas spilling. The two emission concentration signals are compared and they matched perfectly. In Figure 6.4 a WLTC time window is shown to confirm the previous conclusion.

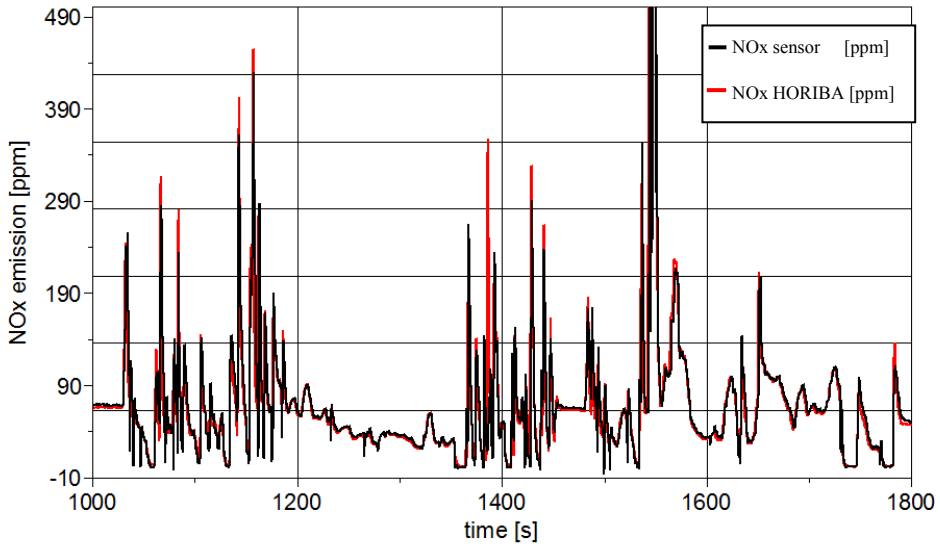

Figure 6.4 Comparison between NOx instantaneous signal measured by the sensor and the analyzer. The green squares select the CWSC that have a duration longer than 10s

However, a resampling of the signals is necessary before applying the alignment. The sampling characteristics adopted by the different software are reported in Table 6.1.

Table 6.1 Description of sampling methods of the three software.

Software	**Sampling base**	**Sampling delta**	**Measure unit**
INCA	Cycle base	8	samples/cycle
IndiCom	Cycle base	1	samples/cycle
AVL Puma	Time base	50	ms

INCA and AVL Puma variables are resampled according to the IndiCom sampling method in order to be not dependent on the calibration of the Air System Model implemented in the ECU, a simplified external model is used to describe the engine filling phenomena. A function of fuel/air equivalence ratio and EGR rate is created with ASCMO to define O_2 mass ratio. 190 reference point measurements are used to generate this black box function. For each point, values of the two inputs and output are specified. λ value is measured while EGR rate is estimated. It is known that:

$$r_{EGR} = \frac{\dot{m}_{tot} - \dot{m}_{air}}{\dot{m}_{tot}} \qquad \text{Eq. 6.6}$$

$\dot{m}_{air}$ is the air mass flow rate, measured by the Sensyflow and $\dot{m}_{tot}$ is the sum of air and fuel mass flow rate. The last parameter is deduced from the intake conditions. It is hypothesized that $\dot{m}_{tot}$ in the engine does not change if the charge at the intake is a mixture of air and exhaust gas recirculated by EGR valve or is only air, for a given intake pressure and temperature. So the characterization of the filling phase for the engine is conducted considering only fresh air. The total air mass flow rate that fills up the combustion chamber is defined:

$$\dot{m}_{22} = \frac{N \cdot V_{eng} \cdot p_2}{95{,}67 \cdot (T_{21} + 273{,}15)} \cdot \lambda_{a,1} \qquad \text{Eq. 6.7}$$

where n is engine speed [rpm],

V_{eng} is engine displacement [l],

p_2 is boost pressure [hPa],

T_{21} is charge air temperature [°C].

The engine volumetric efficiency variation, caused by the variation of intake temperature, is considered with the following mathematical expression.

$$\lambda_{a,1} = \lambda_{a,rif} \cdot \left(\frac{T_{21} - T_{21,rif}}{T_{21,rif} + 273{,}15} \cdot fac + 1 \right) \qquad \text{Eq. 6.8}$$

Where $\lambda_{a,rif}$ is the volumetric efficiency based on $T_{21,rif}$,

$\lambda_{a,1}$ is the volumetric efficiency based on $T_{21,1}$,

$T_{21,rif}$ is a reference intake temperature,

T_{21} is a generic intake temperature,

fac is a parameter that must be calibrated to typify the specific engine application.

Mapping measurements in EOPs shown in Table 5.8 are used in this phase. Using the intake conditions, the $\lambda_{a,rif}$ map and the map of $T_{21,rif}$ are obtained. Then different measures are carried out in operating conditions where the intake temperature is varied. During this second test, $\dot{m}_{22}$ is monitored by the Sensyflow. fac is determinated so that $\dot{m}_{22}$, calculated with Eq. 6.7, fits the acquired fresh air mass flow rate.

6.2 Experimental plan

To prove the performance of the NOx raw emission model estimation during dynamic conditions, the model is tested on two types of driving cycle. In particular:

- 4 repetitions of MNEDC cycle
- 4 repetitions of WLTC cycle.

These tests are conducted at the test bench with warm engine condition (with coolant water temperature of 90 °C) simulating an automatic transmission. The transmission type has an important influence on the engine behaviour. In fact, an automatic transmission determines an engine speed trace that reaches a lower value than N track with a manual transmission. The selected cycles are characterized by very different input parameters thus different information are deduced from each one.

6.2.1 Model validated on MNEDC cycle

The test provides a model of track engine speed stylized with low acceleration, windows at a constant speed, and many events in idle even if accelerations during real driving are more intense and more dynamic.

This cycle includes several steady states and linear increase of engine speed. So it is possible to produce:

- analysis on Cycle Windows with Steady Conditions (CWSC)
- analysis on Cycle Windows with Transient Conditions (CWTC)

Before starting the analysis, it is important to overlap the cycle traces (in terms of engine speed and total fuel injected quantity) and the engine map on which the measurements in nominal calibration is performed and the model is correspondingly trained, Figure 6.5.

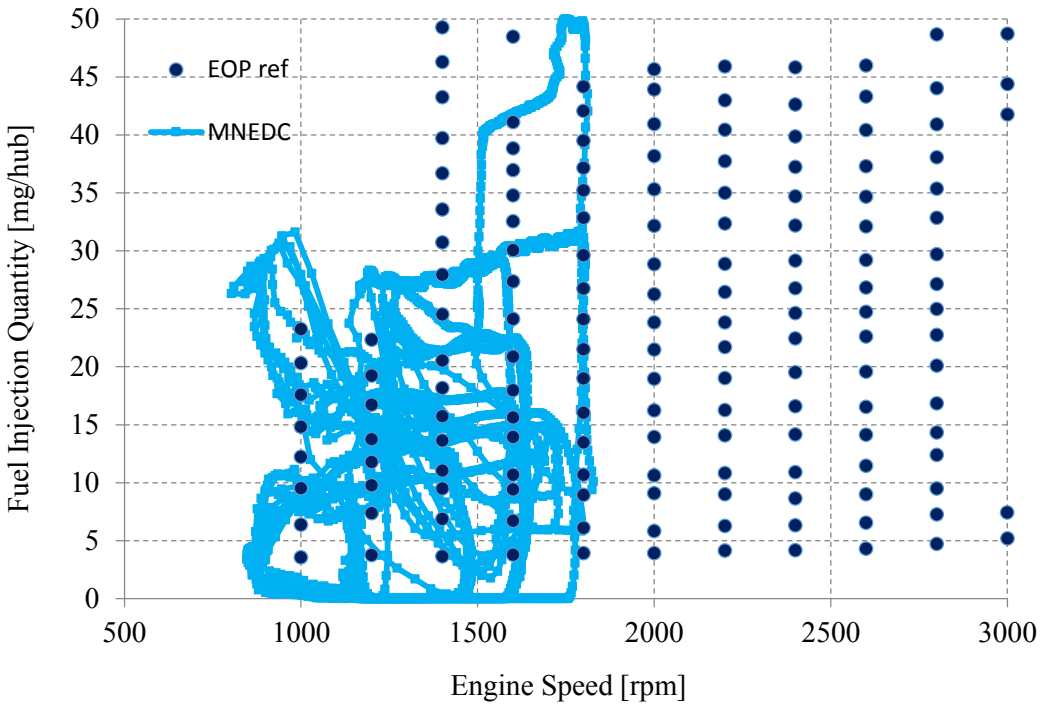

Figure 6.5 MNEDC cycle trace overlapped on the engine map characterized with experimental measurements.

It results that additional measurements are necessary in two areas of the map:

1. map area for engine speed lower than 1000 rpm but higher than 876 rpm (where idle condition is reached) and fuel injection quantity between 0 and 35 mg/hub.
2. map area for engine speed in the range 1000÷1500 rpm at high load.

This check is done also for the WLTC cycle but, in this case, the cycle trace is included completely in the area where measurements were realized. NOx emission signal acquired by AVL Puma has been compared with estimated NOx signal, Figure 6.6. The two NOx signals fit on the first glance; but a deep investigation is essential to define the model performance properly.

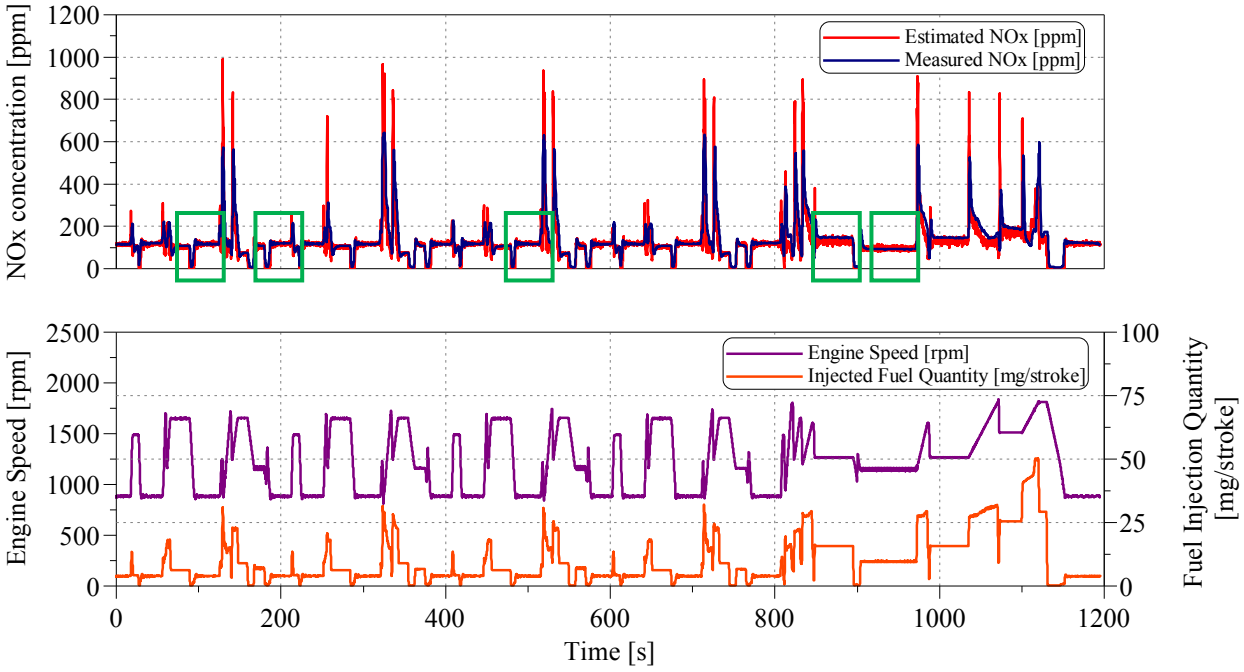

Figure 6.6 Main signals recorded during MNEDC cycle on test bench. In particular, measured and predicted instantaneous NOx are compared (after model calibration in idle condition).

Figure 6.7 shows an example of steady state condition during the MNEDC: the instantaneous value of relative error is included in the range of ± 10 % mainly, even if to include its variation completely a max tolerance of ± 20 % has to be considered.

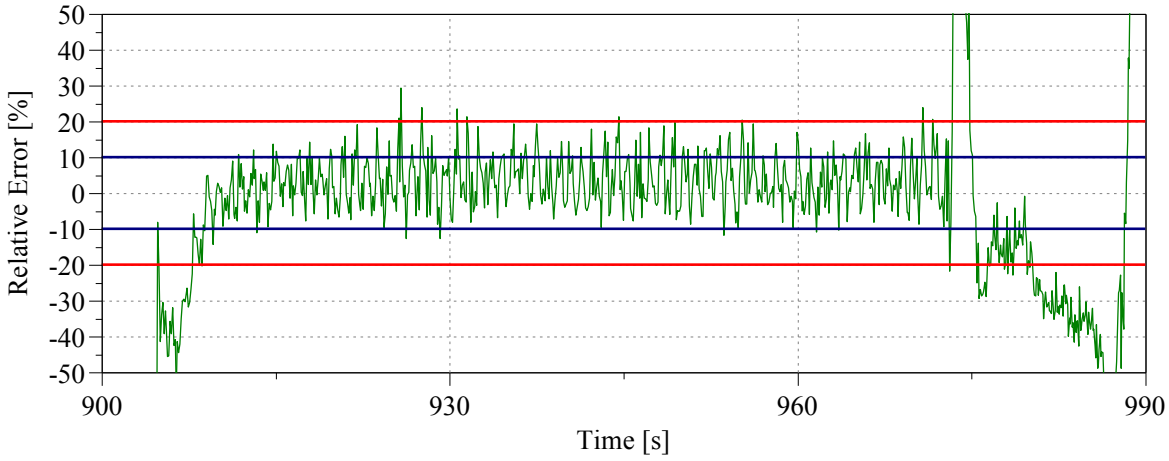

Figure 6.7 Instantaneous relative error related to the instantaneous value of NOx raw emissions.

On each CWSC Figure 6.6 that are characterized by a duration longer than 10 s, the average relative error is calculated and plotted in Figure 6.8. The model generally underestimates the NOx emissions at high NOx levels. The maximum error is -12,1 % at 147 ppm of NOx amount.

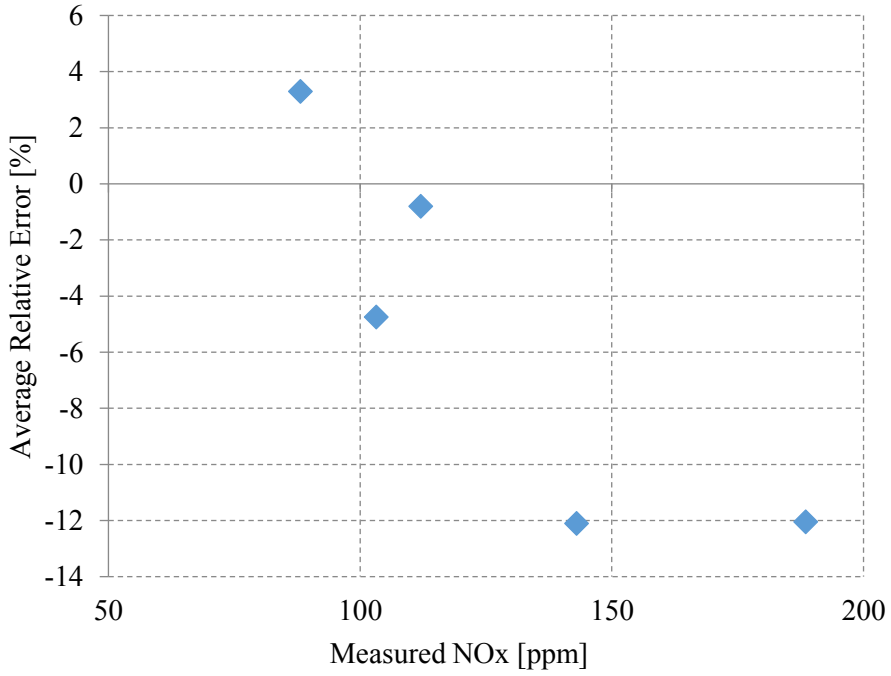

Figure 6.8 Average relative error calculated on the selected CWSC shown in Figure 6.6

About NOx model prediction in transient condition, it appears in Figure 6.9 that the cumulative trend of the two NOx curves and the two absolute instantaneous emissions, measured and estimated, it is possible to identify time instants in which the cumulative error increases. In transient conditions, the distance between the two cumulative curves increases due to the underestimation of the model while during steady state conditions, instead, the distance remained approximately constant.
The conclusion is that the cumulated error during CWTC is increased even if the transient conditions have shorter duration.

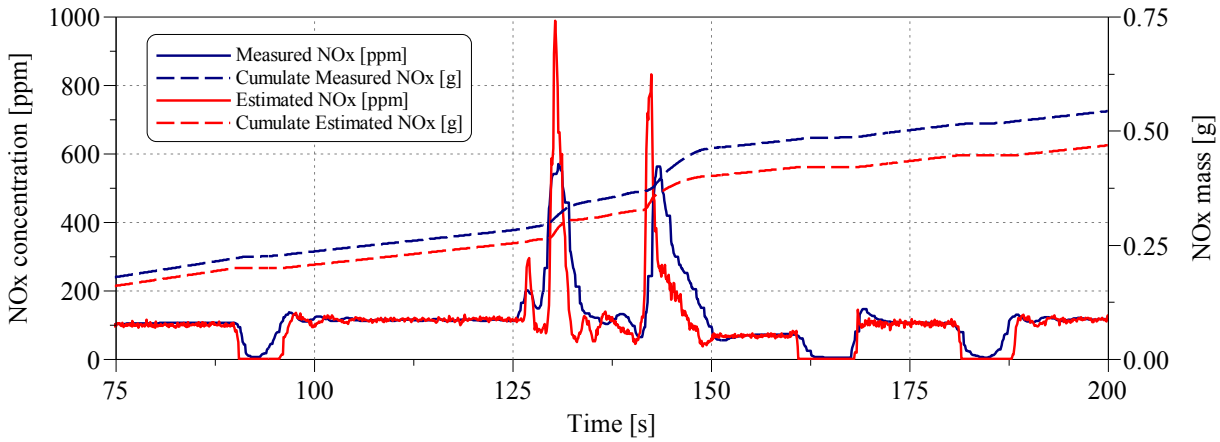

Figure 6.9 Comparison between measured and predicted NOx emissions. Cumulative curves are represented to understand when difference between them increases.

To have more information about how the model responds in transient operating conditions, a map (engine speed-fuel injection quantity) in nominal calibration is obtained for each one of the following parameters:

- NOx emission
- λ at the engine-out section
- rO_2 at the intake manifold
- rEGR at the intake manifold

The signals are obtained supposing that quasi-steady state conditions occur during the entire cycle. Obviously during the cycle this hypothesis is true only when operating parameters reach the established value in nominal calibration. Values that resulted from these maps will be defined "reference" from now on. The objective of this analysis is to identify time windows where the engine operates far or close to the nominal condition and link model performance to particular conditions and/or parameters.

It is considered the window where the engine speed ramp is the slowest. Figure 6.10 compares estimated, measured and reference NOx: in the first part of the ramp, the engine operates far from the nominal condition because there is a difference between the blue and the black line, but it achieves the nominal condition at the end of the window because those lines are overlapped. The spike in the estimated trace is more narrow than the same spike in the measured trace because the estimation has mainly input variables from the ECU while the measurement is affected also by slower mixing effect.

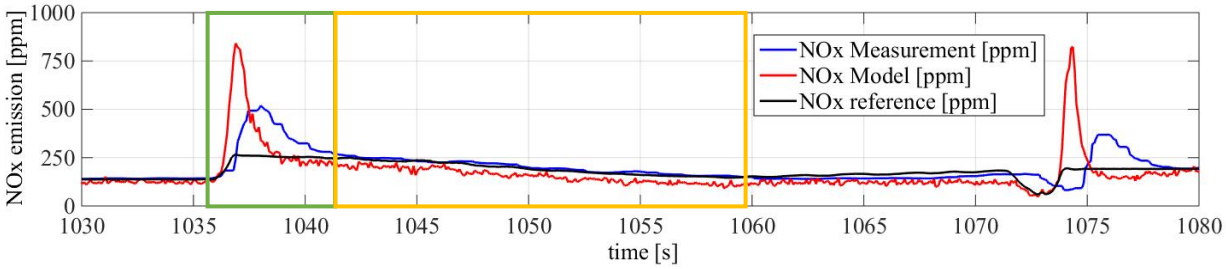

Figure 6.10 Visualization of NOx signals in correspondence of the selected window (slowest ramp)

The analysis starts from the O_2 mass ratio estimation. The oxygen ratio, rO_2, is a function of rEGR and λ. The range in which rO_2 varies is about 18-23.15 %, considering a maximum value of rEGR of 70%. Besides, it is verified that a rO_2 variation of 1%, fixed λ, corresponds to a variation of 10% in the T_{ad}, included in the argument of the model exponential term.

Considering Figure 6.11, in the first part of the ramp, it is possible to read a spike of the oxygen amount which corresponds to a spike of the produced NOx - Figure 6.10, line blue-. Here, the model overestimates the NOx measurement. The cause could be an overestimation of the oxygen. In the second part of the window, the engine operates in nominal condition and the oxygen is slightly underestimated. This leads to the underestimation of the NOx amount.

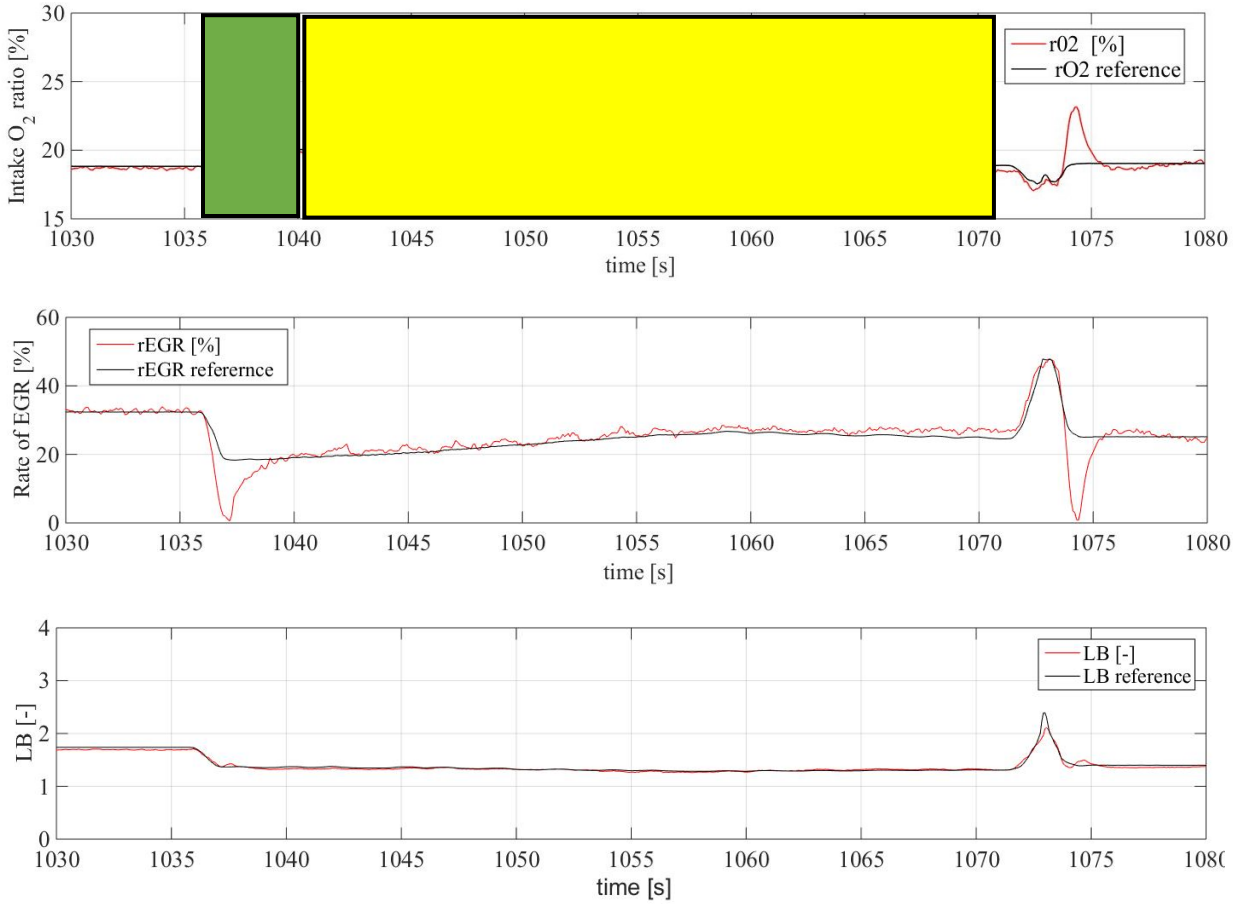

Figure 6.11 Visualization of rO_2, LB, rEGR signals.

It is important to state that the base air system model implemented in the ECU, generally used for the rEGR calculation, is characterized by a tolerance on this parameter estimation of 5% (in term of absolute value). The implemented rO_2 model in the NOx model:

1. is based on the hypothesis of air system stationary conditions.
2. includes only engine volumetric efficiency variation due to the variation of intake temperature.

This model is simplified because it does not take into consideration:

1. dynamic empting and filling phenomena,
2. thermal inertial effects.

So the tolerance on the rEGR estimation is presumably higher. A similar tolerance on this variable is problematic due to the high weight that rO_2 has on the NOx prediction.

To characterize the global prediction of the model, the total quantity of NOx produced during the cycle (expressed in grams) is calculated integrating the curves in Figure 6.6 on the MNEDC duration. Data are shown below in Table 6.2.

Table 6.2 Comparison between model accuracies in the calculation of total amount of NOx produced on the entire cycle.

Repetition n.	NOx Puma Integral [g]	NOx Integral [g]	Relative average error [%]
1	4.462	3.891	-12.8
2	4.451	3.996	-10.2
3	4.417	3.852	-12.8
4	4.381	3.839	-12.4

6.2.2 Model validated on WLTC cycle

This cycle is different from MNEDC for two fundamental reasons:

1. the absence of defined CWSC,
2. the adoption of a smoother speed trace.

In fact, the speed trace is not stylised as MNEDC, increase and decrease of the engine speed have a nonlinear trend. So another type of investigation is judged more appropriate: an analysis on Cycle Windows with Quasi-Stationary Conditions (CWQSC).

This cycle has not only more irregular driving conditions but the engine speed and the fuel injected quantity input curves reach higher values. MNEDC has a maximum N and fuel injection quantity of about 1820 rpm and 50 mg/hub. These conditions are concentrated only in the last part of the cycle. WLTC is characterized by different N peaks that reach 2490 rpm and 53 mg/hub of fuel injection quantity.

In Figure 6.12, the cumulative trend of the two NOx curves, the measured and estimated instantaneous emissions are plotted. The previous results are confirmed. The model underestimates the measurement. Also in this case, the distance between the two cumulative curves increases due to the high underestimation of the model during transient conditions – CWCT- as Figure 6.13 shows.

Moreover, since there are cycle windows in steady state conditions, the total error collected on the NOx amount produced during WLTC is higher than that one calculated for MNEDC.

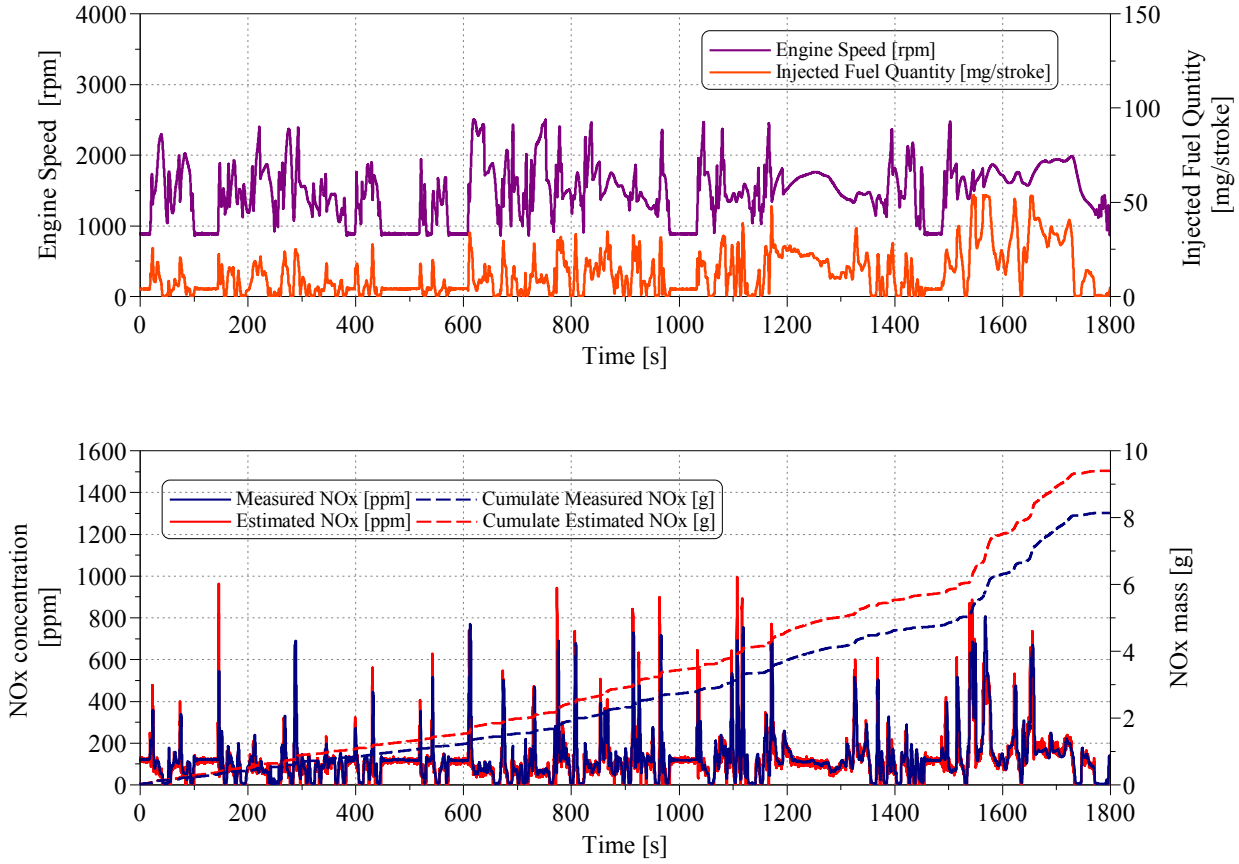

Figure 6.12 Main parameter signals recorded during WLTC cycle on test bench. In particular, measured and predicted instantaneous NOx are compared.

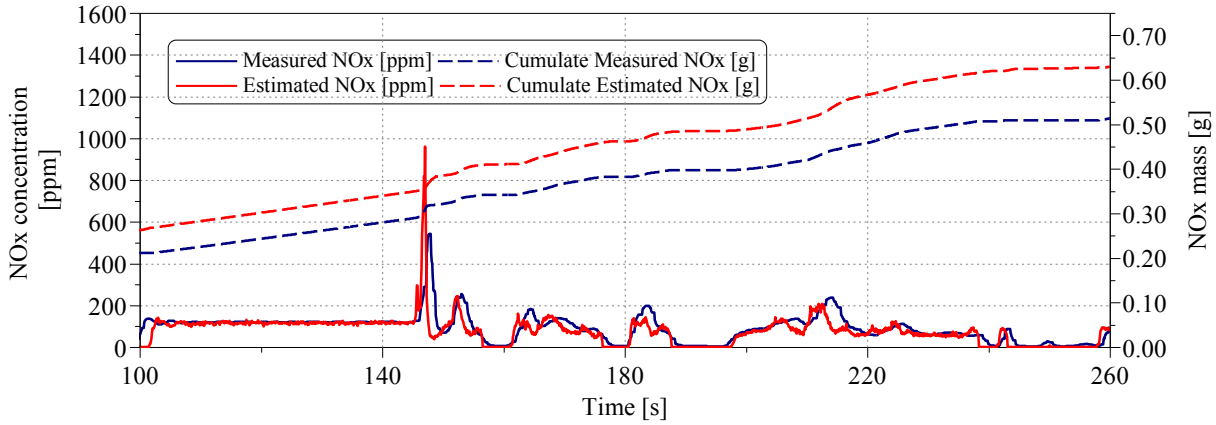

Figure 6.13 Comparison between measured and predicted NOx emissions. Cumulative curves are represented to understand when difference between them increases.

Due to the absence of CWSW, the analysis has been focused on CWQSC windows. In particular, CWQSC between 1210 s and 1276 s is chosen: only in this cycle window, the input variation occurs so slowly that it is possible to consider that the system has time to stabilise its behaviour.

The representation of the instantaneous relative error fluctuates between ± 20 %. The performance in this cycle window respects the tolerance observed in Figure 6.14.

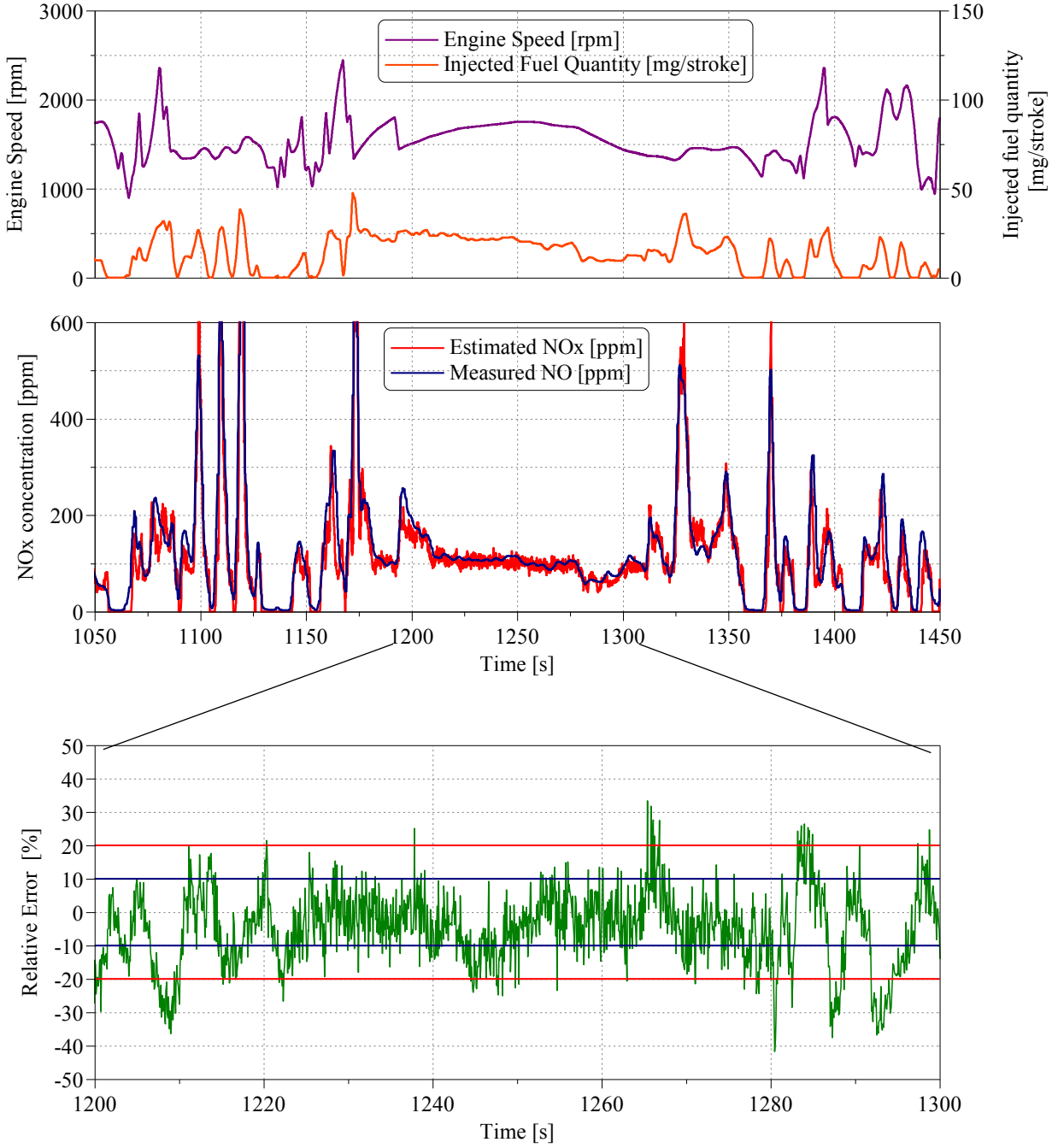

Figure 6.14 Instantaneous relative error related to the instantaneous value of NOx raw emissions with special attention to a CWQSC.

Finally, the total quantity of NOx produced during the cycle (expressed in g) is calculated integrating the curves in Figure 6.12 on the WLTC duration for each four repetitions. Data are shown below in Table 6.3.

Table 6.3 Comparison between models accuracy in the calculation of total amount of NOx produced on the entire cycle.

Repetitions	NOx Puma Integral [g]	NOx Integral [g]	Relative average error [%]
1	9.408	8.142	-13.5
2	9.344	7.875	-15.7
3	9.433	7.790	-17.4
4	9.351	7.806	-16.5

Thanks to the analysis of MNEDC cycle it is concluded that the two models have the same accuracy in CWSC and different behaviour in CWTC.

Conclusion

The aim of this part of the study has been to develop a model able to estimate NOx engine out emission. Particular attention has been focused on the development of a model characterized by a balance between high accuracy and low number of experimental data for the calibration phase. For this reason, after a deep investigation through the literature, a grey box model has been preferred. The starting point has been the grey box model based on in cylinder pressure developed by Guardiola et al.

As first step, different attempts have been performed to improve the reference model performance because experimental test has proved its incapability to catch turbulence effect caused by injection timing variation. A special attention has been paid to the accuracy of the estimation in nominal calibration condition that initially has been far from the requirement of substituting the engine-out NOx sensor with the model. The use of a set point-relative formulation resulted the best solution because it permits to guarantee a low tolerance in nominal condition without causing a worsening of the estimation in the other operating conditions.

The validation of the model has been performed on two specific driving cycles. They have been selected for their different characteristic tracks of engine speed and total injected fuel quantity. In this way the model capability has been studied for very different transient conditions. In the first part of the analysis, when the prediction has been tested in steady state condition, relative error is concentrated in the range $\pm$ 20 % but the maximum error identified in all the range of EGR rate is 40 %. From prediction testing on dynamic cycles, the model performance verified in the examined CWSC gives a maximum average relative error of 5 % and 12,3 % in correspondence of an absolute value of NOx emission respectively lower and higher than 100 ppm. In transient windows it appeared that measured and estimated NOx raw emissions could not be compared instantaneously. From the calculation of total amount of NOx produced in the selected CWTC, it resulted that the model typically underestimates and this underestimation played a significant role on the entire cycle.

Further development should be conducted to obtain results which can be exploited in real applications because the fixed requirement to replace or to diagnose the upstream NOx sensor are: a maximum

relative error of 10 % for the estimation of NOx amount higher than 100 ppm and maximum relative error of 20 % for the estimation of NOx amount lower than 100 ppm.

Improvement of a SCR Kinetic Model: Introduction

Real time characterization of the SCR behaviour allows to obtain an efficient control of the urea dosing strategy. This is particularly true when the after treatment layout is composed by a SCR on Filter –SCRoF- followed by a SCR under floor –SCRuF- because it is relevant to know the amount of slipped NH_3 from the first catalyst which is the unique way to deliver urea to the SCRuF.

Literature and experience have already demonstrated that the introduction of the "physics/chemistry" in ECU models allows to increase the capability to estimate emissions with high accuracy also outside the training area. This meets the need to know then emission situation in every driving condition.

In particular, the aim of this work is to introduce the complete NOx reduction scheme in an already implemented in the ECU. The work environment is Simulink. After a brief description of the SCR and of the starting model, the calibration of the modified model is presented.

7. Selective Catalytic Reduction Description

7.1 General Information

The Selective catalytic reduction (SCR) is a chemical process through which NO_x are reduced by nitrogen compounds, such as *ammonia.* It has been initially applied for industrial stationary engine, but in the last years, car companies have adopted this technology also for mobile diesel engine applications. The Urea-SCR has been selected as the technology of choice for meeting the Euro V NOx limits for heavy-duty truck and bus engines. [1]

The SCR has a typical honeycomb structure: thousands of channels compose the reactor, as it is shown in Figure 7.1.

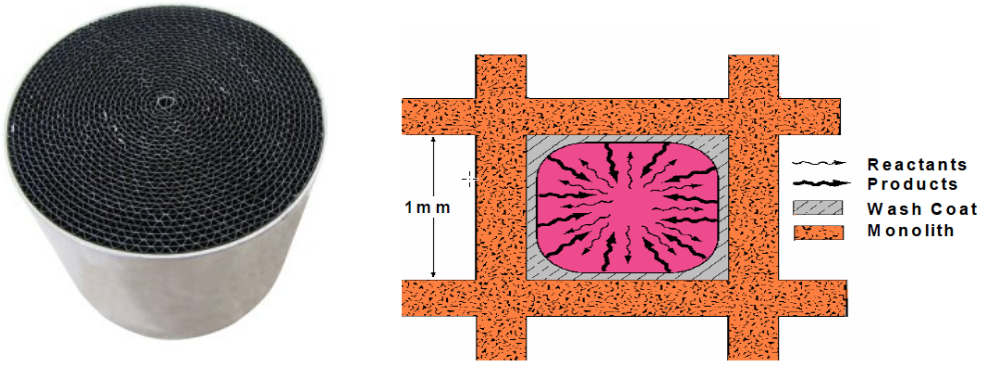

Figure 7.1 SCR section (left). Scheme of SCR channel structure (right) [55]

Each channel is formed by a solid substrate matrix –the monolith- which is covered by a washcoat. The monolith can be built with ceramic or metallic substance. The first function of the reactor is to load ammonia. Therefore, a porous substance which cover the reactor able to adsorb the ammonia is necessary. Zeolites meets this need. Zeolites can be synthetic or naturally occurring alumina-silicate compounds with well-defined crystalline structures and pore sizes. The dimensions of zeolite pores are typically between 3 and 8Å, which falls into the range of molecular sizes. Any molecule of a larger cross-sectional area is prevented from entering of the zeolite cage. [1]

An important characterization of zeolites is based on the number of silica ($SiO_{4/2}$) and alumina ($AlO_{4/2}$) tetrahedrons (T-units) which builds the pore framework. Zeolites are characterized by high

specific surface areas. For example, the ZSM-5 zeolite has surface area of ~400 m^2/g, zeolite mordenite 400-500 m^2/g. Most zeolites are thermally stable up to 500°C. [1] The reaction between NOx and ammonia occurs on the Zeolite's pores occupied by ammonia. Due to its toxic nature, it is not injected directly, but by a precursor: a solution of urea, $CO(NH_2)_2$. In order to avoid the formation of an urea layer around both the intake SCR manifold and the SCR and to improve the mixing between the urea and the exhaust gas, a mixer is mounted at the SCR intake.

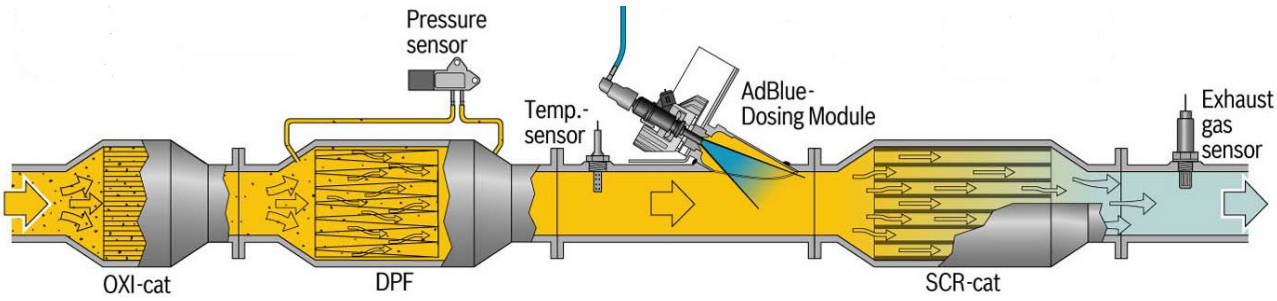

Figure 7.2 Example of after treatment layout involving a SCR

7.1.1 Thermolysis / hydrolysis

A urea-water solution is used which an aqueous urea solution at 32.5% wt concentration. At this concentration urea forms a eutectic solution characterized by the lowest crystallization point of -11°C as Figure 7.3 shows:

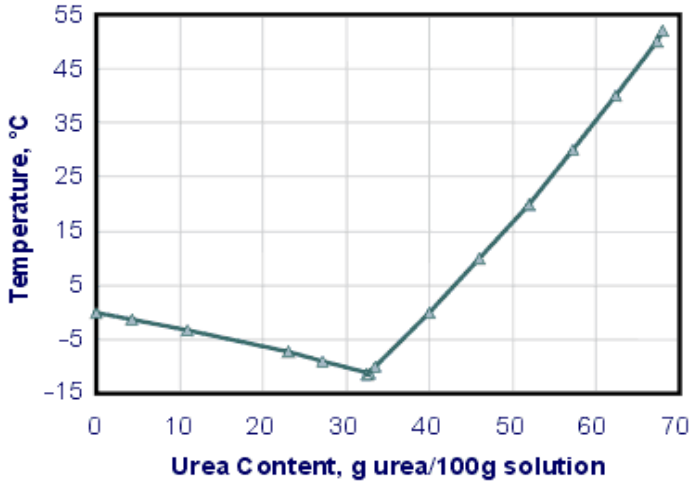

Figure 7.3 Freezing Point of Urea Solutions [1]

The use of eutectic solution provides an additional advantage of equal concentrations in the liquid and solid phases during crystallization. Even if partial freezing occurred in the urea tank, crystallization would not change the concentration of urea solution fed to the SCR system. After the aqueous urea is injected into the exhaust gas flow, the urea is decomposed by the following reaction:

$$CO(NH_2)_2 + H_2O \rightarrow 2NH_3 + CO_2 \qquad \text{R 7.1}$$

In practice, the decomposition of urea proceeds through two separate reaction steps, involving an isocyanic acid (HNCO) intermediate:

$$CO(NH_2)_2 \rightarrow NH_3 + HNCO \qquad \text{R 7.2}$$

$$HNCO + H_2O \rightarrow NH_3 + CO_2 \qquad \text{R 7.3}$$

While urea starts to decompose already at around 160°C, the decomposition cannot reach completion in the gas phase at temperatures typical for diesel exhaust and at the residence time in SCR systems; in fact only up to about 20% of the urea decomposes to HNCO and NH_3 in the gas phase at 330°C, and only about 50% decomposes at 400°C. The remaining urea decomposes only after reaching the surface of the catalyst. [1]

7.1.2 Adsorption/ Desorption

Interactions between gaseous molecules and the catalyst surface proceed via two different mechanisms: Langmuir-Hinshelwood and Eley-Rideal. In the Langmuir-Hinshelwood mechanism, schematized in Figure 7.4, both the gaseous reagents interact with the surface. Therefore, two active free sites are necessary for the storage and for the reaction. The rate of reaction depends on the loading coefficient of both species.

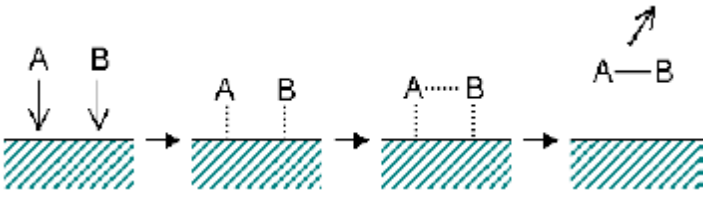

Figure 7.4 Langmuir-Hinshelwood mechanism

The Eley-Rideal mechanism is the process involved in the SCR. In the Eley-Rideal mechanism, the reagent A has a higher propensity to be absorbed on the surface while the reagent B is not absorbed. In this case, only one active site is occupied and rate of reaction depends on the number of active site occupied by the reagent and the partial pressure of the specie B as illustrated in Figure 7.5.

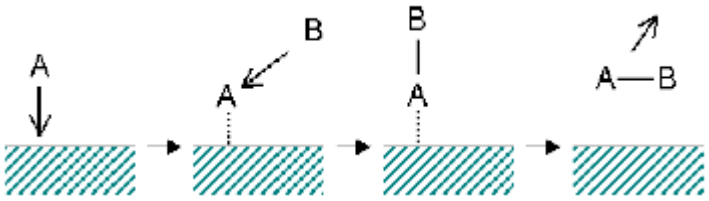

Figure 7.5 Eley-Rideal mechanism

The basis of transient ad/desorption model is the introduction of surface sites and surface site equations. A general surface site (S) is used which comprises the different active sites in a lumped consideration. The stoichiometry of the adsorption and desorption are given by:

$$NH_3 + S \rightarrow NH_3(S) \qquad \text{R 7.4}$$

$$NH_3(S) \rightarrow NH_3 + S \qquad \text{R 7.5}$$

7.1.3 NO_x -Reaction

The reduction of NOx in the gas phase takes place with absorbed ammonia by the Eley-Rideal-mechanism. Therefore, NO_x which is not absorbed on the surface and ammonia in the gas phase does not contribute to the reaction. A number of chemical reactions occur in the ammonia SCR system which reduce NOx to elemental nitrogen:

$$4NO + 4NH_3 + O_2 \rightarrow 4N_2 + 6H_2O \qquad \text{R 7.6}$$

$$NO + NO_2 + 2NH_3 \rightarrow 2N_2 + 3H_2O \qquad \text{R 7.7}$$

$$6NO_2 + 8NH_3 \rightarrow 7N_2 + 12H_2O \qquad \text{R 7.8}$$

$$6NO + 4NH_3 \rightarrow 5N_2 + 6H_2O \quad \text{R 7.9}$$

$$2NO_2 + 4NH_3 + O_2 \rightarrow 3N_2 + 6H_2O \quad \text{R 7.10}$$

The first three reactions are the widely used in the literature for the description of the SCR reaction scheme.

In particular, R 7.6 covers the reduction of NO in an equimolar ratio with ammonia. It is called "standard SCR reaction" because in typical engine exhaust gases NO is the dominant NOx component (NO/NO_x≈90%).[54] The second reaction R 7.7 includes both the reduction of NO and NO_2. It is called "fast reaction" according to experimental investigations that show increased reaction rates in the presence of NO_2. At NO_2/NO_x ratio higher than 50% the $deNO_x$ behavior is lowered again because of the stronger involvement of the "slow reaction" R 7.8 reducing NO_2 only. [54]

Normally, the NO_2 concentration in diesel exhaust gas is low. In some diesel SCR systems, NO_2 levels are purposely to enhance NO_x conversion at low temperatures. In case, the NO_2 content has been increased to exceed the NO level in the feed gas, N_2O formation is also possible:

$$8NO_2 + 6NH_3 \rightarrow 7N_2O + 9H_2O \quad \text{R 7.11}$$

$$4NO_2 + 4NH_3 + O_2 \rightarrow 4N_2O + 6H_2O \quad \text{R 7.12}$$

Undesirable processes could also occur in SCR systems including several competitive, nonselective reactions with O_2, which is abundant in the system. These reactions can either produce secondary emissions or unproductively consume ammonia:

$$2NH_3 + 2O_2 \rightarrow N_2O + 3H_2O \quad \text{R 7.13}$$

$$4NH_3 + 3O_2 \rightarrow 2N_2 + 6H_2O \quad \text{R 7.14}$$

$$4NH_3 + 5O_2 \rightarrow 4NO + 6H_2O \quad \text{R 7.15}$$

$$2NH_3 + 2NO_2 + H_2O \rightarrow NH_4NO_3 + NH_4NO_2 \quad \text{R 7.16}$$

Ammonium nitrate formation can be avoided by making sure that the temperature never falls below 200°C. The tendency of NH_4NO_3 formation can also be minimized by supplying into the gas stream less than the precise amount of NH_3 necessary for the stoichiometric reaction with NO_x (1 to 1 mole ratio). [1]

When the flue gas contains sulfur, as is the case with diesel exhaust, SO_2 can be oxidized to SO_3 with the following formation of H_2SO_4 caused by reaction with H_2O. Ammonia can also react with SO_3 to form solid compounds which deposit on and foul the catalyst:

$$NH_3 + SO_3 + H_2O \rightarrow NH_4HSO_4 \qquad \text{R 7.17}$$

$$2NH_3 + SO_3 + H_2O \rightarrow (NH_4)_2SO_4 \qquad \text{R 7.18}$$

7.2 SCR After-treatment Layout

The following section is a brief overview of the possible ATS which involves the SCR.

In the proposed layouts, devices like Diesel Oxidation Catalyst –DOC-and a Diesel Particle Filter – DPF- are adopted for the reduction of particular matter and hydrocarbon emission.

The DOC promotes a range of oxidation reactions utilizing oxygen which is in ample supply in diesel exhaust gas at almostall engine operating conditions. As schematized in Figure 7.6, it:

- oxidases CO and HC in CO_2 and H_2O
- oxidases NO in NO_2. This leads to an increase of NO_2/NO at low temperature
- increases exhaust average temperature.

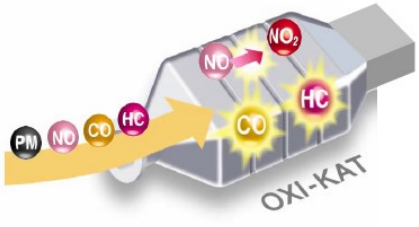

Figure 7.6 Functional scheme of a DOC

DPF is a filter that captures particle emissions. Due to the low bulk density of diesel particulates, DPF can quickly accumulate considerable volumes of soot. The collected particulates would eventually cause excessively high exhaust gas pressure drop in the filter, which would negatively affect the engine operation. Therefore, diesel particulate filter systems have to provide a way of removing particulates from the filter to restore its soot collection capacity. This removal of particulates is known as DPF *regeneration*. Thermal regeneration of DPF is typically employed, where the collected particulates are oxidized to gaseous products, primarily to carbon dioxide:

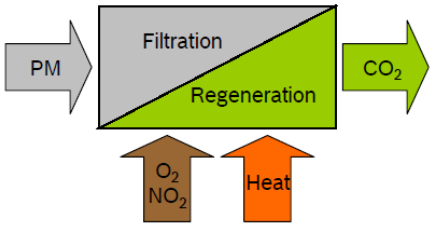

Figure 7.7 Physical scheme of DPF

The first layout, in Figure 8.8, consist in a DOC followed by a SCR and a DPF. In general, if the SCR is mounted close to the engine as in Figure 7.10 and Figure 7.11, the NOx conversion is higher during cold start phase because the hot exhaust gas heats the SCR and the temperature limit, above which the reactions starts, is reached earlier. It can be a disadvantage in full load because too much heat passes through the SCR and this leads to an oxidation of ammonia and low NOx conversion efficiency. The same problem can occur during the DPF regeneration because the heat passes through the SCR catalyst at an average temperature of 700°C.

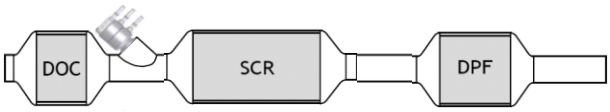

Figure 8.8 Layout number 1

In order to have a lower volume than the one in Figure 7.9, a large SCR is adopted after a coupling of a DOC and a DPF. This architecture is advantageous for the urea mixing and decomposition to NH3. It suffers from a delayed light-off due to the presence of high thermal inertia components located upstream of the SCR. In moderate / low load operation, the thermal losses generated by the intermediate pipe also affect negatively the performance of the SCR. [3]

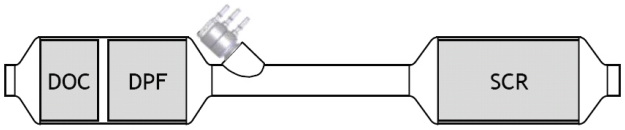

Figure 7.9 Layout number 3 [57]

The solution SCRoF combines the functions of the DPF and SCR because it is a DPF covered by SCR washcoat in Figure 7.10. In this way, the filter is no longer loaded with precious metals and the total system cost, the package volume and weight are reduced.
This layout benefits from a fast light-off and higher temperatures due to the less total thermal mass. This promotes a high NOx conversion especially in cold start. The limited length available for urea mixing and decomposition to NH_3 also requires an optimized dosing system and an exhaust mixing device. [3][56]

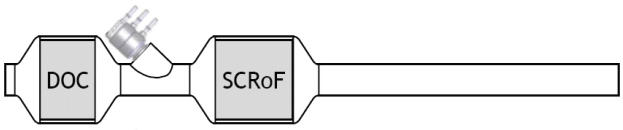

Figure 7.10 Layout number 4 [57]

The last layout consists of a SCRoF-SCRuF combination system as shown in Figure 7.11. The dosage takes place before the SCRoF, so that the supply of the SCR with ammonia is done only through the SCRoF slip. The performance of the SCRuF will be driven by the calibration of the SCRoF control: a low NH_3 coverage of the SCRoF will lead to low NH_3 feed for the SCRuF and low NOx conversion in the SCRuF whereas a high NH_3 coverage of the SCRoF will lead to higher NH3 feed for the SCRuF and increased efficiency of the under-floor SCR. For this reason, it is said that the SCRuF "works passively". [3]

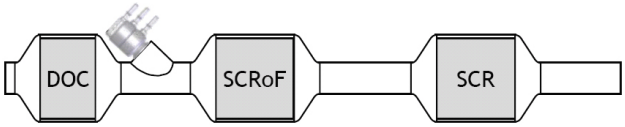

Figure 7.11 Layout number 5 [57]

The solution with a close-coupled SCRoF with an under-floor SCR provides the highest potential for the NOx reduction. [57] Finally, SCR systems may include an oxidation catalyst

downstream of the SCR catalyst to control ammonia slip. This catalyst is called “ammonia slip catalyst” (ASC). The ASC becomes increasingly important in SCR systems designed for high NOx conversion efficiency, operating at high NH_3-to-NOx ratio which tends to increase the ammonia slip. [1]

8. SCR Kinetic Model Description

The detailed chemical reactions scheme has been presented in the previous chapter while this chapter explains the assumptions and the chosen approach for the model implementation.

8.1 Hypothesis

As any other after treatment devices, the phenomena involved in a SCR are complex and it is impossible to describe them in detail. An ECU model should be as simple as possible. The basic aim is to estimate the surface storage and the catalytic conversion. Secondary phenomena such as convective, diffusive and conductive gas transport, boundary layer transfer, pore diffusion, heat loss in radial direction are neglected and the following general assumptions are made:

- the exhaust gas flow through the catalyst is homogeneous and independent of the radius
- the temperature is uniform across the catalyst and, thus, the heat transfer between gas and wall is ideal
- the ammonia loading of the catalyst is constant over the catalyst
- the SCRoF behaves like a catalyst in terms of temperature distribution and SCR -reactions; i.e. there are no effects through the wall passage or similar
- there are only two phases: the gas phase and the solid catalyst surface.

As already written, a SCR has a honeycomb structure composed by thousands of individual channels. In an 1D approach, only one channel among the thousands ones that compose the catalyst is considered for the development of the model. The resolution of the element balance is computed for a small, gaseous moving element V_B that flows in the channel as illustrated in Figure 9.1. Therefore, a Lagrangian approach is adopted.

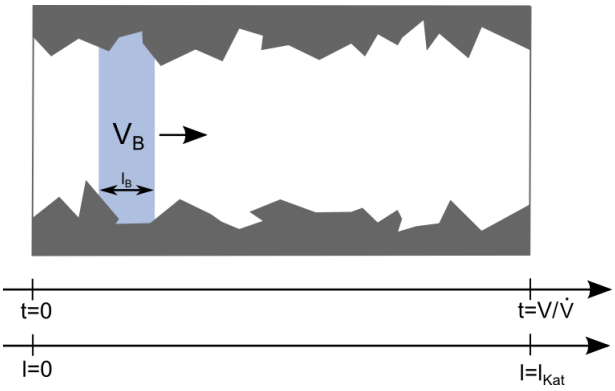

Figure 9.11-D approach for SCR kinetic model development

At time t=0s, the moving element starts with the input concentration of the respective substances and, at the end, leaves the catalyst with the concentrations resulting from the reaction rates. Therefore, the boundary condition is:

$$c_y(t = z = 0) = c_{y,Us} \qquad \text{Eq. 8.1}$$

Assuming that the moving element passes through the catalyst of volume V with a constant volume flow $\dot{V}$, it is deducted that it remains for the residence time $V/\dot{V}$ in the catalyst. Location and time are equivalent with this approach: a material transfer in the location coordinate does not have to be recorded as the balance element moves along with it. The number n_y of molecules for each species y in the balance area is

$$n_y = V_B c_y = l_B A_{channel} c_y \qquad \text{Eq. 8.2}$$

where $A_{channel}$ designates the cross-section of a channel

c_y is the concentration of the specie y

l_B is the length of the moving element V_B

The concentration of the specie c is a function of time (or of the respective location) and defined through the reaction rate, $\dot{r}$. Two different approach as can be adopted to express the reaction rates. Wurzenberger and Wanker suggest to apply the *steady-state Eley-Rideal mechanism* when the steps of ad/desorption are assumed to be in equilibrium and the *transient rate mechanism* when the rate

equation for ad/desorption are taken into account. The complete scheme adopted by Wurzenberger is the following in Table 8.1:

Table 8.1 Rate expressions (in mol/m^2/s) for catalytic reactions [54]

Steady State Rates	*NOx standard reduction*	$\dot{r}_{std} = K_{a,std} e^{\left(\frac{-E_{a,std}}{R\,T}\right)} c_{NO} \frac{K_{b,std} e^{\left(\frac{-E_{b,std}}{R\,T}\right)}}{1 + K_{b,std}\, e^{\left(\frac{-E_{b,std}}{R\,T}\right)}} c_{NH_3}$
	NOx fast reduction	$\dot{r}_{fast} = K_{a,fast} e^{\left(\frac{-E_{a,fast}}{R\,T}\right)} c_{NO} c_{NO_2} \frac{K_{b,fast} e^{\left(\frac{-E_{b,fast}}{R\,T}\right)}}{1 + K_{b,std}\, e^{\left(\frac{-E_{b,fast}}{R\,T}\right)}} c_{NH_3}$
	NOx slow reduction	$\dot{r}_{slow} = K_{a,slow} e^{\left(\frac{-E_{a,slow}}{R\,T}\right)} c_{NO_2} \frac{K_{b,slow} e^{\left(\frac{-E_{b,slow}}{R\,T}\right)}}{1 + K_{b,slow}\, e^{\left(\frac{-E_{b,slow}}{R\,T}\right)}} c_{NH_3}$
	NH_3 oxidation	$\dot{r}_{NH_3,oxi} = k_{NH_3,oxi} e^{\left(\frac{-E_{NH_3,oxi}}{R\,T}\right)} c_{NH_3}$
	Hydrolysis	$\dot{r}_{Hyd} = k_{Hyd} e^{\left(\frac{-E_{Hyd}}{R\,T}\right)} c_{HCNO} c_{H_2O}$
Transient Rates	*Adsorption*	$\dot{r}_{Ads} = k_{Ads} e^{\left(\frac{-E_{Ads}}{R\,T}\right)} c_{NH_3} [1 - \theta]$
	Desorption	$\dot{r}_{Des} = k_{Des} e^{\left[\frac{-E_{Ads}(1-\varepsilon\theta)}{R\,T}\right]} \theta$
	NOx standard reduction	$\dot{r}_{std} = k_{std} e^{\left(\frac{-E_{std}}{R\,T}\right)} c_{NO} \theta^* \left[1 - \frac{\theta}{\theta^*}\right]$
	NH_3 oxidation	$\dot{r}_{NH_3,oxi} = k_{NH_3,oxi} e^{\left[\frac{-E_{NH_3,oxi}}{RT}\right]} \theta$

The expressions collected in Table 8.1 are the results of experimental works; but it is possible to recognize the "classic Arrhenius" form:

$$\dot{r}_y = k_y e^{\left(\frac{-E_y}{R\,T}\right)} c_y\, c_{i\ldots} \qquad \text{Eq. 8.3}$$

where $\dot{r}$ is the reaction rate in [mol /m²/s]

k_{Hyd} is the frequency factor [1/s]

E is the activation energy [J/mol]

R is the universal gas constant, equals to 8.3144621 [J/mol/K]

T is the mean temperature of the catalyst [K].

8.1.1 Thermolysis and hydrolysis

The hydrolysis, the decomposition of $HCNO$ to NH_3 and CO_2, is represented using only one reaction instead of the complete scheme which involves three reactions as presented in the previous Chapter:

$$HNCO + H_2O \rightarrow NH_3 + CO_2 \qquad \text{R 8.1}$$

A further simplification is adopted because the dependency on the water has been neglected. Therefore, considering what is reported in Table 8.1 for the hydrolysis reaction, it is possible to write:

$$\dot{r}_{Hyd} = k_{Hyd} e^{\left(\frac{-E_{Hyd}}{R\,T}\right)} c_{HCNO} \qquad \text{Eq. 8.4}$$

8.1.2 Adsorption/ Desorption

According to the Eley-Rideal mechanism, the reaction between NOx and ammonia occurs only with loaded ammonia. The assumed hypothesis is that a fixed number of adsorption sites is available on a catalyst. This number can be parameterized as a mass equivalent in the form of the maximum storage capacity of the catalyst $m_{NH3,Max}$ in the model. With this determination, the surface coverage θ of the SCR-catalyst can be defined as the quotient of the current NH_3 -Loading m_{NH3} and maximum NH_3 -loading $m_{NH3,\,Max}$:

$$\theta = \frac{m_{NH_3}}{m_{NH_{3,max}}} \qquad \text{Eq. 8.5}$$

Considering Tronconi et al.' experimental results, the adsorption and desorption of ammonia on the surface of the SCR-catalyst are chemical reactions that are associated with an activation energy.[58][59][60]. Moreover, the same authors concluded that the rate of NH3 adsorption on active centers is similar to that of its surface reaction with NO, whereas the rate of NH3 desorption is nearly negligible. [58] The reaction rate for the adsorption reaction is formulated as:

$$\dot{r}_{Ads} = k_{Ads}\, c_{NH_3} (1-\theta) e^{\left(\frac{-E_{Ads}}{R\,T}\right)} \qquad \text{Eq. 8.6}$$

For the desorption reaction, it is applied a Temkin-type surface coverage dependency taken from Lietti at al. [58] In the cited paper, Lietti et al. concluded that the Temkin approach fits best to experimental data compared to other dependencies such as a modified Temkin-type and Freundlich

approach. In the Temkin approach, the non-linear dependency of the desorption on the surface coverage θ can be adjusted by the parameter ε.

$$\dot{r}_{Des} = k_{Des}\,\theta e^{\left(\frac{-E_{Ads}(1-\varepsilon\theta)}{R\,T}\right)} \qquad \text{Eq. 8.7}$$

The higher the surface coverage, the more dominant is the desorption against the adsorption. Thus, different temperatures lead to a different adsorption/desorption equilibrium which results in a different maximum (practically achievable) loading of the SCR catalyst.

8.1.3 NH_3-Oxidation

The oxidation of ammonia is of practical importance, especially during particle filter regeneration. In the SCRoF-system, it is also relevant, due to the higher temperatures because of its proximity to the engine. Due to the non-destructive limited relevance, a simple approach is proposed here, which assumes that the reaction takes place in the gas phase and there is no oxygen limitation:

$$\dot{r}_{Oxi} = k_{Oxi}\,c_{NH_3} e^{\left(\frac{-E_{Oxi}}{R\,T}\right)} \qquad \text{Eq. 8.8}$$

8.1.4 NO_x-Reaction

The reduction of NOx takes place with absorbed ammonia by the Eley-Rideal-mechanism: the reaction between NO_x and ammonia occurs only on the SCR surface. Ammonia reacts selectively with NOx in the presence of oxygen to nitrogen and vapor. The overall SCR reactions scheme is the following:

$$NH_3 + NO_x \rightarrow N_2 + H_2O \qquad \text{Eq. 8.9}$$

The reaction rate is modelled as follows:

$$\dot{r}_{NO_x} = k_{NO_x}\,c_{NO_x} e^{\left(\frac{-E_{NO_x}}{R\,T}\right)} \qquad \text{Eq. 8.10}$$

It is considered a simplified transient approach which does not take into account the different SCR behavior for different $^{NO}/_{NO_2}$ ratios.

8.2 Derivation of balance equations

For each chemical species involved in the problem, it is necessary to write the balance equation. The chemical species are:

- HNCO
- NOx
- NH3.

8.2.1 Balance of isocyanic acid

Only the reaction Eq. 8.1 is involved in the isocyanic acid balance. Replacing the expression for the hydrolysis reaction rate Eq. 8.4 into Eq. 8.2, the equation becomes:

$$l_B A_{channel} \frac{dc_{HCNO}}{dt} = -l_B a_{Cat} \dot{r} \Rightarrow \frac{dc_{HCNO}}{dt} = -\frac{a_{Cat}}{A_{channel}} k_{Hyd} e^{\left(\frac{-E_{Hyd}}{T}\right)} c_{HCNO} \qquad \text{Eq. 8.11}$$

where dc_y/dt is the absolute rate of reaction in [mol/m^3/s]

$\dot{r}$ is the reaction rate in [mol /m²/s]

a_{Cat} is the washcoat and channel geometry per meter of catalyst and it is expressed in [m²/m]

It is helpful to write the following identity:

$$aK = \frac{a_{cat}}{A_{channel}} k \qquad \text{Eq. 8.12}$$

a is a normalized surface factor (usually between 0 and 1), which can display ageing and HC poisoning. This saves a parameter which cannot be determined separately from the other parameters anyway and adds all the catalyst properties to the new frequency factor, K. As it is notable, the conversion of the species y does not depend on the size of the selected balance, since l_b is cancelled. The initial value problem –IVP- can be written as:

$$\frac{dc_{HCNO}}{dt} = -aK_{Hyd} e^{\left(\frac{-E_{Hyd}}{R\,T}\right)} c_{HCNO} \qquad \text{Eq. 8.13}$$

$$c_{HCNO}(t = z = 0) = c_{HCNO,Us}$$

With the given initial condition, the solution of this differential equation is:

$$c_{HCNO} = c_{HCNO,Us} e^{-aK_{Hyd} e^{\left(\frac{-E_{Hyd}}{RT}\right)} t} \quad \text{Eq. 8.14}$$

The equation allows to compute the concentration of isocyanic acid at each location in the catalyst (or at any time, respectively). This expression is later used to solve the NH_3 -balance. The concentration of isocyanic acid, which leaves the catalyst is:

$$c_{HCNO,Ds} = c_{HCNO,Us} e^{-aK_{Hyd} e^{\left(\frac{-E_{Hyd}}{RT}\right)} \frac{V}{\dot{V}}} \quad \text{Eq. 8.15}$$

The main advantage is the possibility to solve the balance equation with only one computational step because the differential equation can be solved analytically without discretization of the gas phase in finite-dimensional balance elements for the numerical solution. Therefore, numerical inaccuracies and instabilities do not occur. All the analytic passages shown in this paragraph can be taken as reference to obtain the equations which will be presented in the following part.

8.2.2 Ammonia-Balance

In order to write the ammonia balance, it is necessary to consider:

- desorption and hydrolysis reactions for ammonia formation
- oxidation and adsorption reactions for ammonia destruction.

The IVP becomes:

$$\frac{dc_{NH_3}}{dt} = a\left(-K_{Oxi} c_{NH_3} \exp(-E_{Oxi}/RT) - K_{Ads} c_{NH_3} (1-\theta) \exp(-E_{Ads}/RT) + K_{Des} \theta \exp\left(-E_{Des}(1-a\theta)/RT\right) + K_{Hyd} c_{HNCO} \exp(-E_{Hyd}/RT)\right) \quad \text{Eq. 8.16}$$
$$c_{NH_3}(t = z = 0) = c_{NH_3,Us}$$

In this equation it should be noted that besides the concentration of ammonia c_{NH3}, the concentration of isocyanic acid is also a function of time.

8.2.3 NOx -Balance

The NO_x concentration at the outlet of the catalyst can be computed solving the following IVP:

$$\frac{dc_{NOx}}{dt} = -aK_{NOx} e^{\left(\frac{-E_{NOx}}{RT}\right)} c_{NOx} \quad \text{Eq. 8.17}$$
$$c_{NOx}(t = z = 0) = c_{NOx,Us}$$

The solution is:

$$c_{NOx}(t) = c_{NOx,Us} e^{-aK_{NOx} e^{\left(\frac{-E_{NOx}}{RT}\right)} t} \quad \text{Eq. 8.18}$$

8.2.4 Fill Level Balance

The fill level of the catalyst can be written taken into account the balance equations already described. It is assumed that the storage in the gas phase is negligible compared to the storage of ammonia on the surface and the temperature, pressure and filling level are constant over the running length of the balance element. Thus, the differences of the concentrations of NO_x, NH_3 and HNCO can be directly used as a measure of the change in the ammonia accumulator. An exception is the ammonia oxidation, which leads to an integration calculation: Ammonia is decomposed to water and nitrogen via the running length of the catalyst. This is no longer visible at the exit, unless water or nitrogen is additionally balanced. As a formula written, the change of NH_3 -storage is based on the concentration changes between input and output:

$$\frac{dm_{NH_3}}{dt} = f_1\left(r_{NOx,Ds} - r_{NOx,Us}\right) + f_2\left(r_{NH_3,Us} - r_{NH_3,Us} - r_{NH_3,Oxi}\right) + f_3\left(r_{NCO,Us} - r_{HNCO,Ds}\right) \qquad \text{Eq. 8.19}$$

The factors f_i denote the respective stoichiometric conversion factor to the corresponding NH_3–mass. The virtual NH_3 -concentration $-r_{NH3,Oxi}$, which describes the ammonia-proportion, which "disappears" by oxidation, represents the mentioned special case. For the calculation, a negative ammonia concentration, which is formed at the exit of the catalyst by oxidation, is taken into account. The equation is numerically integrated in the model to determine the ammonia-loading of the catalyst computing θ, according to Eq. 8.5, and considering that m_{NH_3} is a calibration parameter.

8.3 Implementation of the complete NO x reduction scheme

The aim of this work is to implement the complete NO_x reduction scheme:

$$4NH_3 + 2NO_2 + 2NO \rightarrow 4N_2 + 6H_2O \qquad \text{R 8.3}$$

$$4NH_3 + O_2 + 4NO \rightarrow 4N_2 + 6H_2O \qquad \text{R 8.4}$$

$$8NH_3 + 6NO_2 \rightarrow 7N_2 + 12H_2O \qquad \text{R 8.5}$$

All the reactions happen at the same moment, but the way with which NO_x reduction proceeds in the SCR depends on the exhaust gas composition, temperature and the surface coverage of ammonia. Both the steady approach and transient approach are proposed in Table 8.1. Here, the transient approach has been chosen considering that the ECU model will be adopted for transient application. Among several expressions Lietti et al. introduce:

$$\dot{r}_{std} = k_{std} e^{\left(\frac{-E_{std}}{RT}\right)} c_{std} \theta^* \left[1 - \frac{\theta}{\theta^*}\right] \quad \text{Eq. 8.20}$$

to describe the NOx reduction. Lietti et al. suppose that the rate of reaction is independent of the ammonia surface coverage above a critical surface fraction while, in this work, the hypothesis is the absence of the critical loading coefficient and, therefore, a linear dependency between the rate of reaction and the loading coefficient. Moreover, this expression has been extended to the other NO_x reactions:

$$\dot{r}_{slow} = K_{slow}[NO_2]\theta e^{-\frac{E_{slow}}{RT}} \quad \text{Eq. 8.21}$$

$$\dot{r}_{std} = K_{std}[NO]\theta e^{-\frac{E_{std}}{RT}} \quad \text{Eq. 8.22}$$

$$\dot{r}_{fast} = K_{fast}[NO][NO_2]\theta e^{-\frac{E_{std}}{RT}} \quad \text{Eq. 8.23}$$

The balance which involves both NO and NO_2 is the following:

$$\begin{cases} \dfrac{dc_{NO}}{dt} = -aK_{fast} c_{NO_2} c_{NO} \theta \exp\left[\dfrac{-E_{fast}}{RT}\right] - aK_{std} c_{NO} \theta \exp\left[\dfrac{-E_{std}}{RT}\right] \\ \dfrac{dc_{NO_2}}{dt} = -aK_{fast} c_{NO_2} c_{NO} \theta \exp\left[\dfrac{-E_{fast}}{RT}\right] - aK_{slow} c_{NO_2} \theta \exp\left[\dfrac{-E_{slow}}{RT}\right] \\ c_{NO}\,(t = z = 0) = c_{NO,Us} \\ c_{NO_2}\,(t = z = 0) = c_{NO_2,Us} \end{cases} \quad \text{Eq. 8.24}$$

The non-linearity of the problem can be noticed in the first addendum of the right hand of the equations. For this reason, an analytic solution cannot be implemented in the model. Only numerical methods can be adopted to solve this kind of problem involving a discretization of the time.

8.3.1 Explicit Solution

Numerical methods are commonly used for solving IVP when it is difficult or impossible to get the exact solution. The solution obtained via a numerical solution is an approximate solution. Literature offers several algorithms to solve IVP, but the need of the development of a model adaptable to the ECU computational capability, leads to build a code as simple as possible. Therefore, the first attempt has been the implementation of an explicit code.

The knowledge about the explicit method and, in particular, how stable they are, is consolidated. In this case, a classic explicit Runge-Kutta method is adopted. Runge-Kutta methods are one-step multistage methods. Starting from y_0 at time t_0 and a finite step h, it produces an approximation y_1 at time $t_0 + h$ of the solution $y(t_0 + h; y_0)$. Furthermore, to compute y_1, a Runge-Kutta method computes s intermediate steps where s is known as the number of stages. More precisely, a Runge-Kutta method for a system, i.e., $\dot{y} = f(t, y)$, is defined by

$$y_{n+1} = y_n + h \sum_{i=1}^{s} b_i \, k_i \qquad \text{Eq. 8.25}$$

$$k_i = f(t_n + c_i h, y_n + h \sum_{i=1}^{s} a_{i,j} \, k_j) \qquad \text{Eq. 8.26}$$

The coefficients c_i, a_{ij} and b_i fully characterize the method and they are usually given in a matrix called "Butcher tableau". The components of the vector c_i are the increments of t_n and the entries of the Butcher tableau are the multipliers of the approximate slopes which, after multiplication by the step size h increment y_n. The components of the vector b are the weights in the combination of the intermediary values k_j.

$$\begin{array}{c|cccc} c_1 & a_{11} & a_{12} & \dots & a_{1s} \\ c_2 & a_{21} & a_{22} & \dots & a_{2s} \\ \vdots & \vdots & \vdots & \ddots & \vdots \\ c_s & a_{s1} & a_{s2} & \dots & a_{ss} \\ \hline & b_1 & b_2 & \dots & b_s \end{array}$$

Figure 8.1 Butcher tableau structure

For the classic Runge-Kutta 4, the Butcher tableau has the following scheme:

$$
\begin{aligned}
k_1 &= f(t_n, y_n) \\
k_2 &= f\left(t_n + \frac{1}{2}h, y_n + \frac{1}{2}hk_1\right) \\
k_3 &= f\left(t_n + \frac{1}{2}h, y_n + \frac{1}{2}hk_2\right) \\
k_4 &= f\left(t_n + h, y_n + hk_3\right) \\
y_{n+1} &= y_n + \frac{h}{6}(k_1 + 2k_2 + 2k_3 + k_4)
\end{aligned}
$$

	c	A			
k_1	0	0			
k_2	1/2	1/2	0		
k_3	1/2	0	1/2	0	
k_4	1	0	0	1	0
y_{n+1}	b^T	1/6	2/6	2/6	1/6

Figure 8.2 Runge-Kutta 4, Butcher tableau

It is easy to apply the Runge-Kutta algorithm to the exanimated case. The catalysis is subdivided into n step (100)

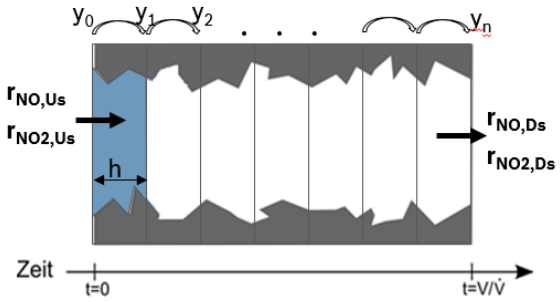

Figure 8.3 Runge-Kutta hypothesis

with a step length equal to

$$h = \frac{SCR\ volume}{number\ of\ steps \cdot volume\ flow}\,[s] \qquad \text{Eq. 8.27}$$

The algorithm shows a high tendency to numerical instability. For example, with trial calibration values and for the case characterized by the highest value of mass flow, the algorithm is not able to complete the computation as shown in Figure 8.4:

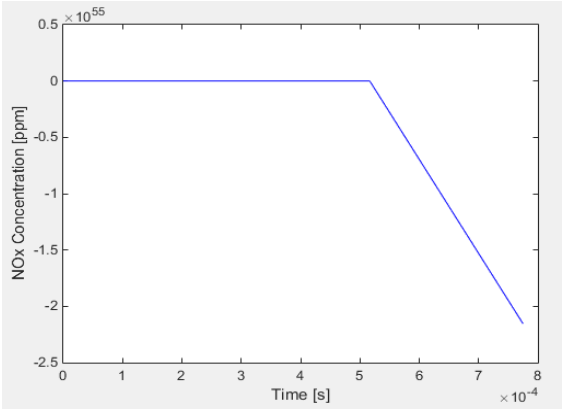

Figure 8.4 Example of an instability of the Runge-Kutta algorithm

To get stability, the reduction of the length step should be sufficient. This solution cannot be followed due to the increase of the number of the steps necessary to complete the computation and, thus, the increase of the computation time that is not compatible with the ECU resource.

It is clear that the present problem is a "stiff" problem. A problem is said to be stiff if the solution being sought varies slowly, but there are nearby solutions that vary rapidly. The software Matlab® offers several libraries to solve this kind of problem. The used library is ode23s which is a Rosenbrock modified algorithm of orders 3 and 2 with error control for stiff systems. It advances from y_n to y_{n+1} with the second-order method (that is, without local extrapolation) and controls the local error by taking the difference between the third- and second-order numerical solutions. Matlab® offers also a second library -ode15s- to solve stiff problems, but it leads to the same results. The adoption of an already implemented code is a necessary step to have a reference to compare with the algorithm which will be developed for the ECU application.

9. Calibration of the modified SCR kinetic Model

The aim of this part of the work is to test the algorithm rather than to achieve a "right" calibration parameter set. A further step in which an optimization tool will be developed will be necessary. To test the model, three kinds of measurement have been conducted:

- "Filling and emptying test"
- Transient test
- RDE test

All the details of the experimental set-up are proposed in Chapter 2; but, here, it is recalled that the RDE activity has been conducted on a vehicle which has a DOC followed by a SCRoF and a SCR under floor while for the test bench activity, the same engine has the DOC followed by a SCRoF without a second SCR.

9.1 Filling and Emptying Tests

Starting from an empty SCR, a filling and emptying test consists in dosing an amount of urea until the phenomena of urea slip comes. The test is conducted for a fixed EoP, thus for a fixed raw NOx emission, a fixed SCR average temperature and a fixed exhaust mass flow. In common practice, this kind of test allows to compute the maximum loading coefficient for a fixed exhaust mass flow and average SCR temperature. In this work, it can give more information because it can be used to understand which are the values within the calibration parameter should be in order to have an acceptable performance during the calibration phase.

In particular, the choice of the EoPs is a relevant step to understand the SCR kinetic model behavior for the widest engine working field. Table 9.1 collects the chosen EoPs. It is necessary to highlight that the EoP with the lowest SCR average temperature is measured even if it occurs only during cold start condition when the average SCR temperature is not above 200°C and it is not able to promote NOx conversion with high accuracy.

Table 9.1 Chosen Operative points for filling and empty test

EoP [rpmxbar]	Average SCR temperature [°C]	Exhaust Mass Flow [kg/h]
1500x3	170	75
1500x4	220	86
2000x4	250	90
2000x6	300	120
2600x8	350	132

An emptying and filling test consists of a series of stages: before each experiment the catalyst has been heated to about 530°C for 15 minutes. In this way it is possible to empty the SCR, then it is possible to cool down the system to the desired average temperature. The experiments are performed with ammonia to NO_x ratios (ANR) slightly up to unity in order to reduce the experimental duration time.

Considering Figure 9.2, it is possible to explain how the experiment proceeds. At time zero only the exhaust mass flow is fed into the SCR. The SCR is empty, hence there is no NOx conversion. The blue line which is the amount of NOx upstream the SCRoF is overlapped on the orange line which is the NOx at the SCRoF outlet. This stage lasts about 25 s in the plotted case. Then, the urea is injected in the system. It is used for NO_x conversion and stored on the catalyst surface at the same time. As the coverage of NH_3 on the catalyst builds up, the rate of NO_x reduction increases and the NO_x concentration at the reactor exit falls due to high conversion efficiency. When the catalyst approach the steady-state condition, NH_3 slip is observed at the last stage, urea dosing is switched off, enabling the rate of NO_x conversion falling to zero after the period of time when the NO_x conversion is guaranteed by the NH_3 storage.

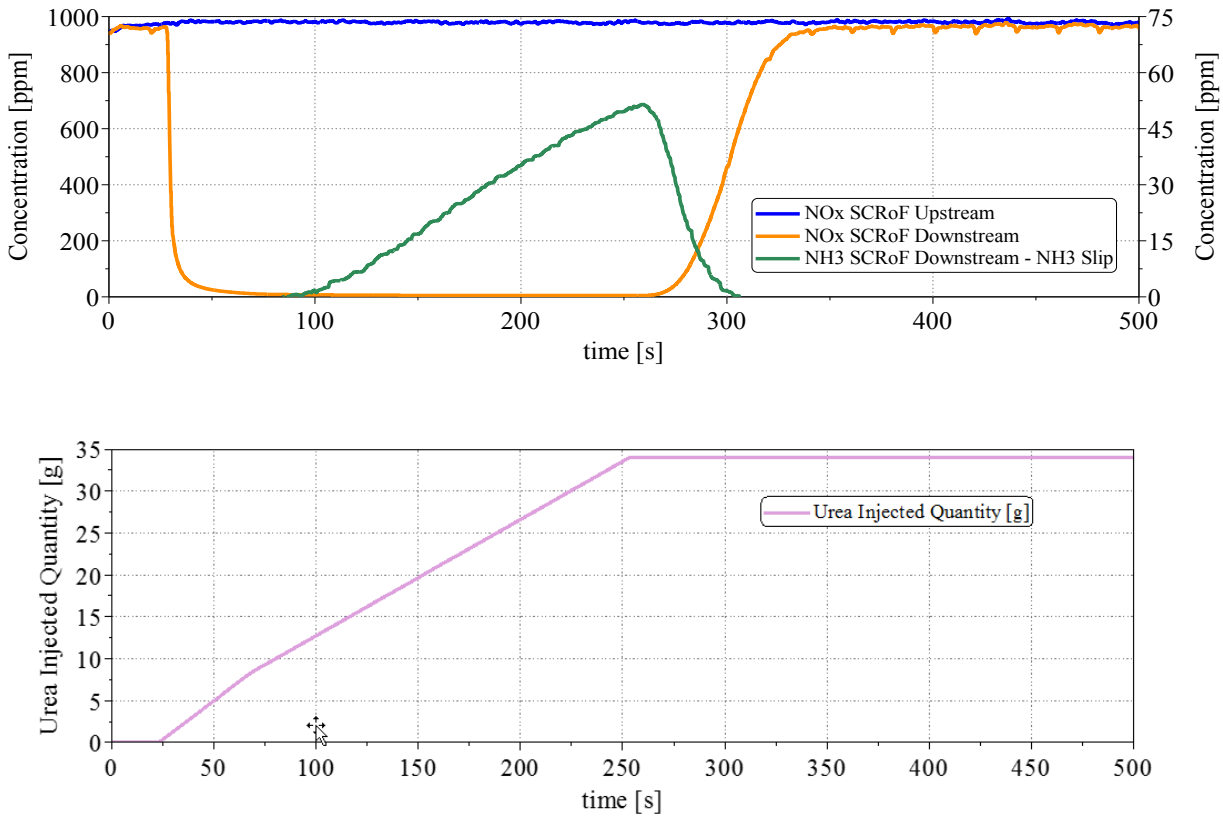

Figure 9.2 Example of Filling and emptying test (EoP 2600x8 [rpmxbar]; SCRoF temperature 350°C; Exhaust mass flow 130 kg/h)

The aim of this part of the work is to understand which is the order of magnitude of the calibration parameters when different operating points are considered. For this reason, for each EoP is found a set of calibration parameters values. These results are obtained with a DoE approach: each calibration parameter is varied within a plausible range and the values of the calibration parameter, which are used to obtain the results in Figure 9.3, Figure 9.4, Figure 9.5, Figure 9.6 and Figure 9.7, are obtained considering the trial with the best RMSE.

In Figure 9.3, NOx measured downstream the SCRoF in orange and the model estimation in violet are represented while the SCRoF inlet measurements is plotted in blue and the cumulate of injected urea in pink. In particular, Figure 9.3 shows the results of the first test when the exhaust gas flow has a SCRoF temperature of 170°C and a mass flow of 75 kg/h. Comparing Figure 9.2 and Figure 9.3, it is observed a difference. The urea dosing occurs early and, thus, the SCRoF converters NOx into N_2

immediately. Due to the low temperature, the efficiency of the SCR is low and its maximum value is 67%. Moreover, at the end of the test, the SCRoF is not completely empty because the NOx downstream measurement is never closed to the NOx upstream. The R^2 is 0.84 and the RMSE 44.03.

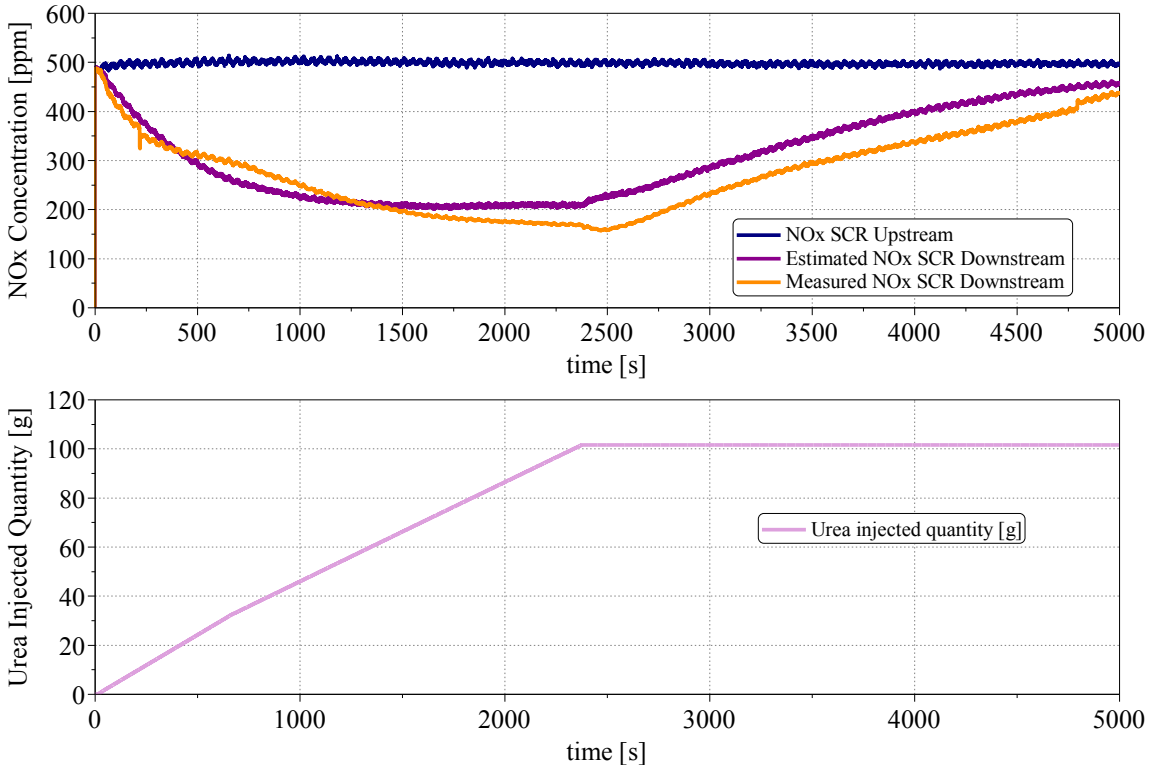

Figure 9.3 Filling and Emptying test (EoP 1500x3 [rpmxbar]; SCRoF temperature 170°C; Exhaust mass flow 75 kg/h)

Figure 9.4 shows the case characterized by an average SCRoF temperature of 220°C and an exhaust mass flow of 86 kg/h. Here the maximum conversion efficiency is 94%. The model has a RMSE 35.57 and the R^2 0.97.

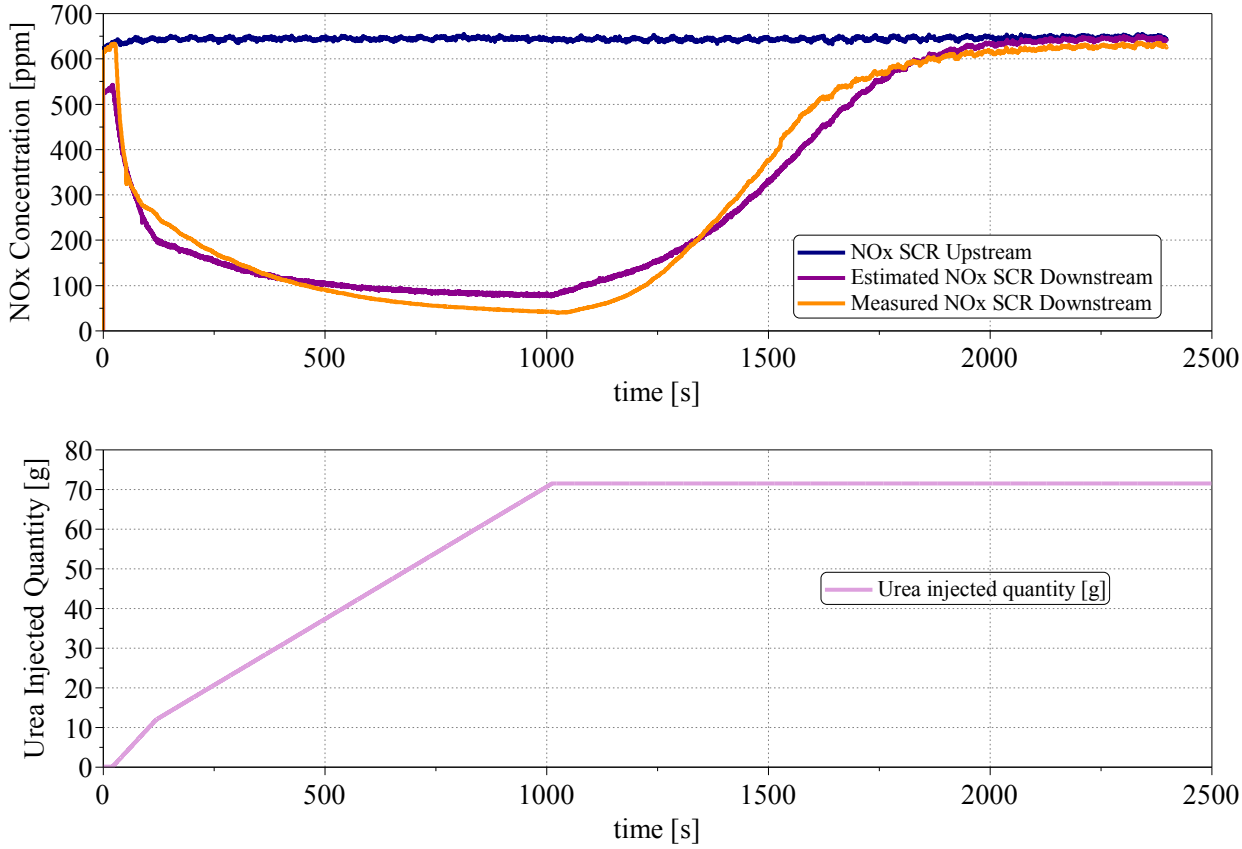

Figure 9.4 Filling and Emptying test (EoP 1500x4 [rpmxbar]; SCRoF temperature 220°C; Exhaust mass flow 86 kg/h)

Figure 9.5, Figure 9.6 and Figure 9.7 show further operating points: the average temperature is above 200°C (250°C for the case in Figure 9.5, 300°C for the case in Figure 9.6, 350°C for the case in Figure 9.7). Starting from the case with 250°C of average SCR temperature to the case of 350°C, the urea dosing injection starts later and urea quantity injected is higher. The efficiency increases with the temperature: in all the cases its value is slightly less than 100%.

In each case the estimation trace follows the measurement track; but during the emptying phase, the adopted method for the calibration is not robust because the value of the curve of the model estimation is not able to follow the measurement trace. The development of an optimization tool could be the answer to obtain a better result because it is not possible to be sure to reach the value of the calibration parameter which gives the highest accuracy with the DoE approach.

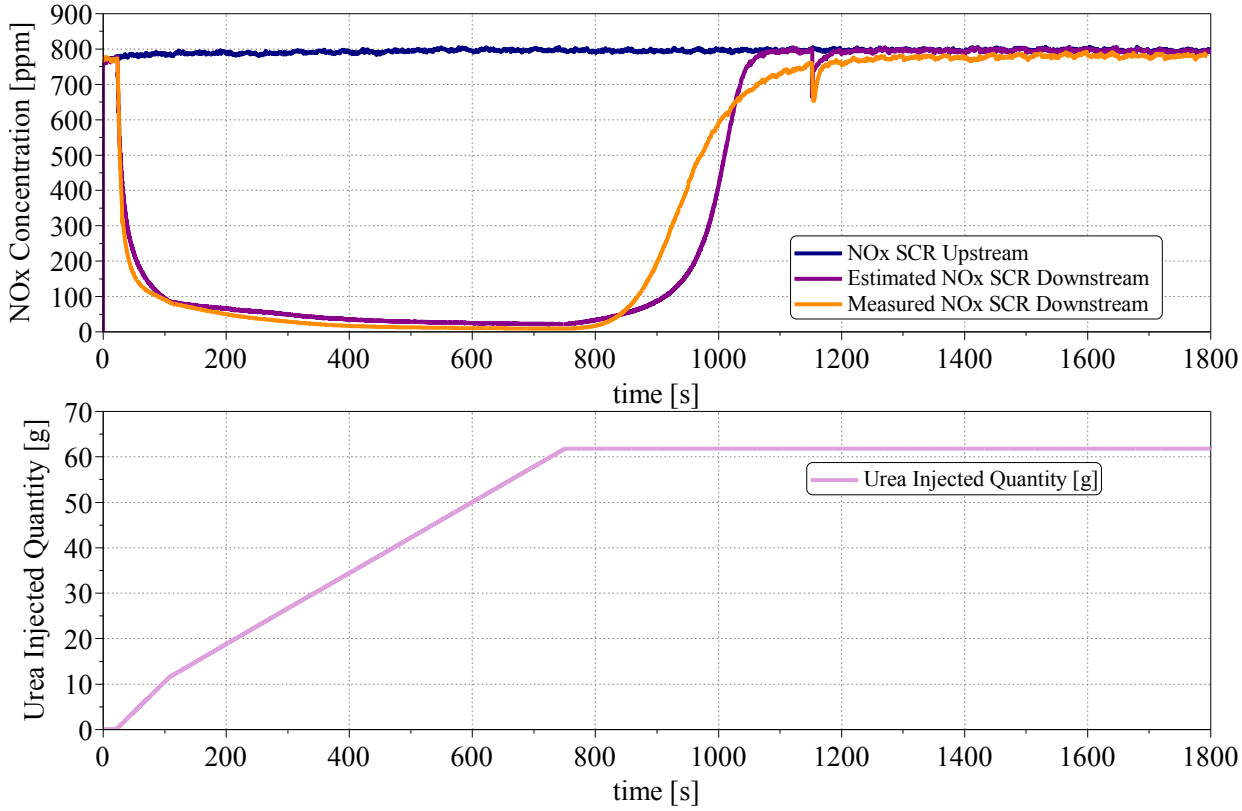

Figure 9.5 Filling and Emptying test (EoP 2000x4 [rpmxbar]; SCRoF temperature 250°C; Exhaust mass flow 90 kg/h)

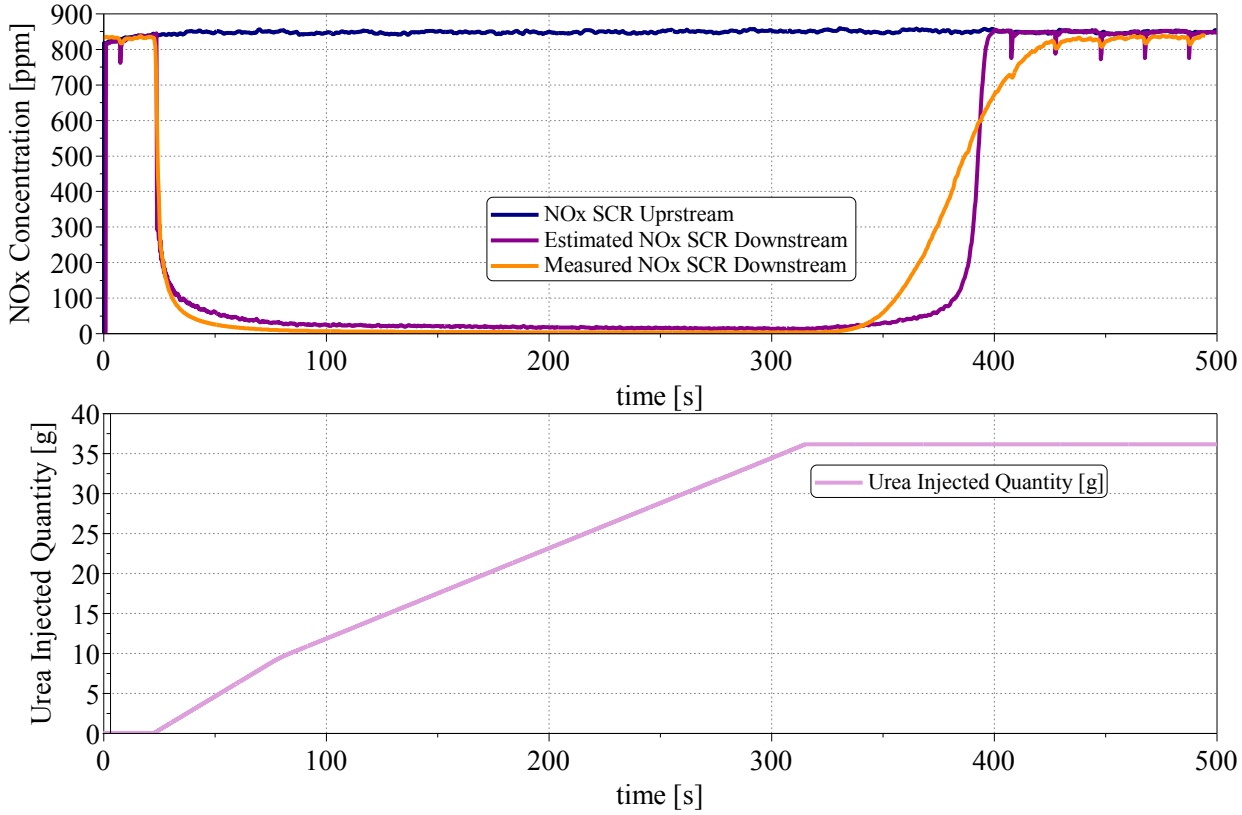

Figure 9.6 Filling and Emptying test (EoP 2000x6 [rpmxbar]; SCRoF temperature 300°C; Exhaust mass flow 120 kg/h)

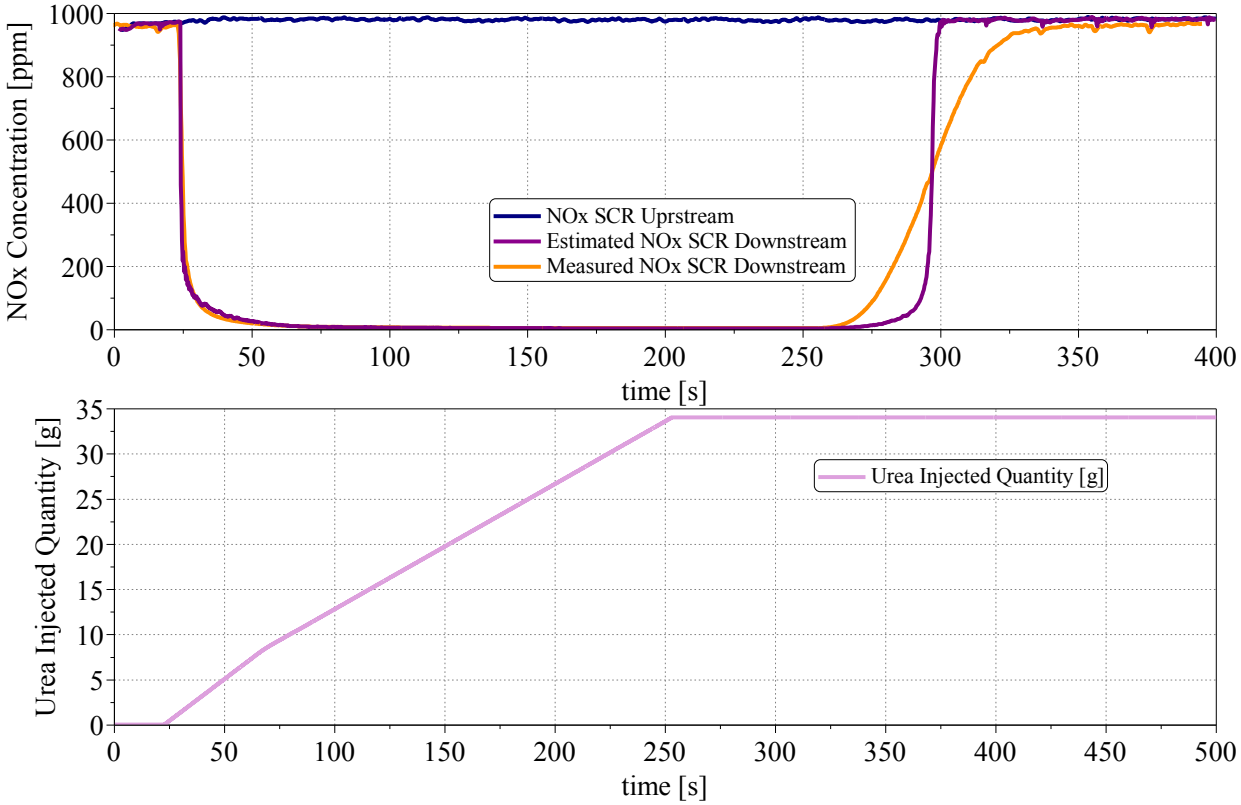

Figure 9.7 Filling and Emptying test. (EoP 2600x8 [rpmxbar]; SCRoF temperature 350°C; Exhaust mass flow 132 kg/h)

For each trace, the computed statistics are:

Table 10.2 Main statistical parameter for emptying and filling test

Test n.	**1**	**2**	**3**	**4**	**5**
SCR Average Temperature	170°C	220°C	250°C	300°C	350°C
R^2	0.84	0.95	0.98	0.93	0.92
RMSE	44.03	35.57	56.19	97.43	126.95

9.2 Calibration of the model

The model is calibrated using a transient drive cycle (here: WLTC) on the test bench. The test has been conducted in cold condition in order to have the first part of the trace with an average SCR

temperature below 200°C. In Figure 9.8 it is possible to read the average SCR temperature and the exhaust mass flow elaborated by the SCR.

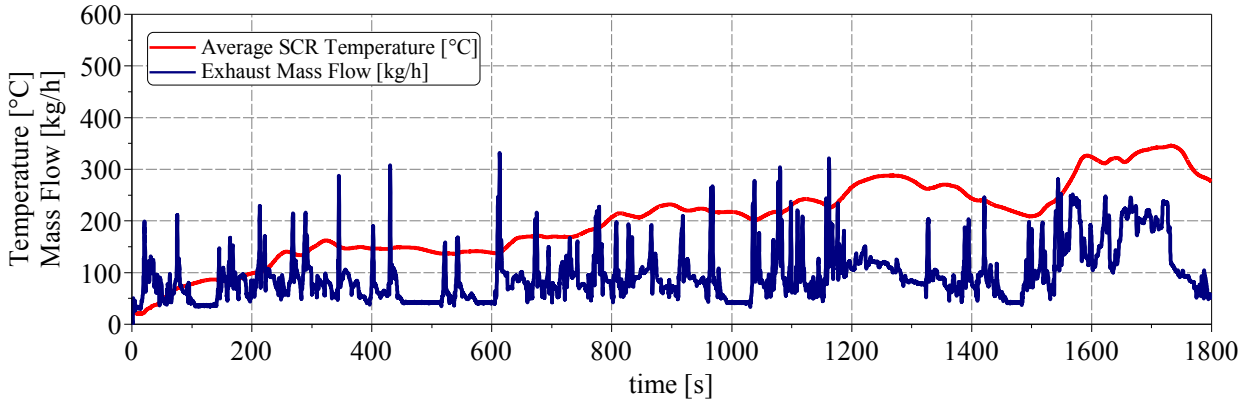

Figure 9.8 SCR average temperature and exhaust mass flow during WLTC

The SCRoF is not empty when the test starts because the following experimental procedure has been considered:

1. emptying of the SCRoF at constant operating point
2. conditioning cycle EU91 VDM which is composed by three repetitions of the extra-urban part of NEDC
3. cool down of the engine for 1.5 h
4. WLTC.

The quantity of NH_3 mass stored in the SCRoF before the WLTC is 1.75 g.

The calibration constants set is achieved considering the relative error on the cumulate curves. In this phase of the development of the work, the achievement of the best calibration parameter set is not the priority goal because the developed model is only a benchmark for a further ECU implementable model. For this reason, a DoE approach is adopted starting from the results obtained from the preliminary filling and emptying test investigation.

In Figure 9.9, the result after of the calibration phase is shown. Until about 800 s, the SCRoF is not able to reduce NO_x due to the low temperature. For this part of the cycle, the model is able to estimate the NOx downstream the SCRoF with 5.98% of relative error on the cumulate curves. Later, there is an increase of the relative error which is regain at the end of the cycle when it is 2.15%. It is necessary

to improve the calibration in the middle part of the cycle where the error is high: 9.83%. The error rises when urea injection events occur; this can be caused by not accurate estimation of the loading coefficient due to the fact that this work is focused only on the balance of NOx.

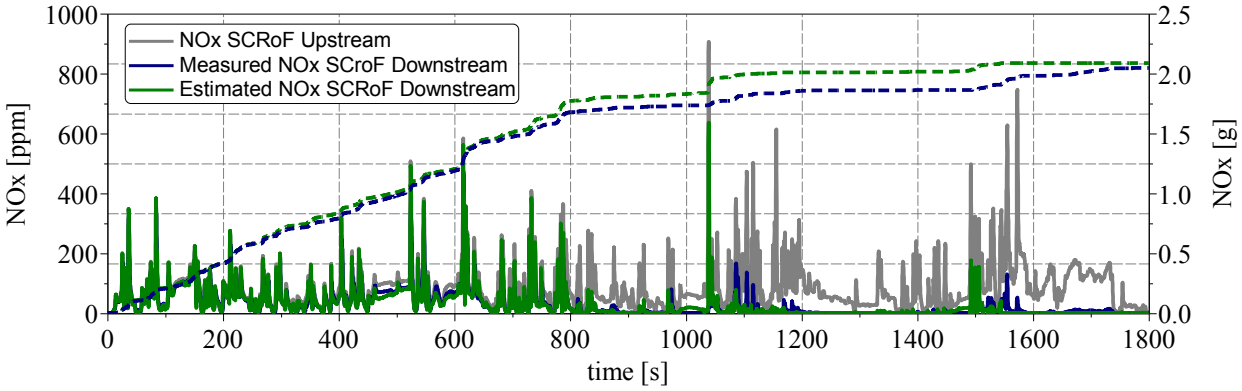

Figure 9.9 Continuous line: comparison between the instantaneous measured NOx SCRoF upstream, measured and estimated NOx SCRoF downstream. Dashed line: NOx cumulate curves

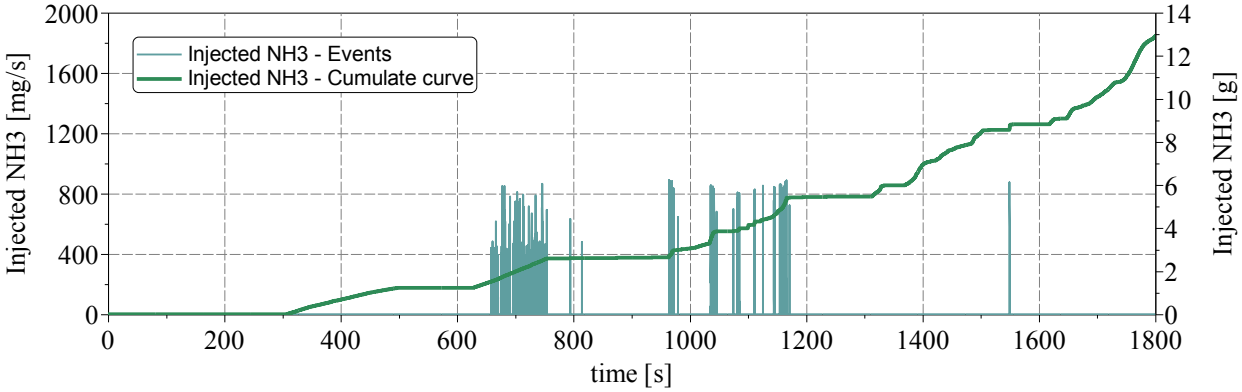

Figure 9.10 Adblue injected quantity during WLTC investigation

The trace of engine speed and injected fuel quantity of a RDE test measured on the highway in Stuttgart with the vehicle is shown in Figure 9.11. Instead, Figure 9.12 shows the average SCR temperature and the exhaust mass flow measured. The measurement is conducted alternating period of time in which the Adblue is dosed to period of time when the Adblue is not dosed in order to test the behavior of the model in both situations. The average SCRoF temperature never goes below the temperature limit (200°C) under which the SCRoF does not work. To test the algorithm, also in this case the set of calibration parameters is obtained by a DoE approach. The results are shown in Figure 9.13. At the end of the test, the cumulate error is 10.66% which can be considered a promising results

for a preliminary investigation. The error rises when the third period of time characterized by Adblue dosing occurs as it is possible to notice comparing Figure 9.13 and Figure 9.14. Also in this case, the error can be affected by a not accurate estimation of the loading factor. Moreover, there is a satisfying correlation because the R^2 is 0.92 and the RMSE is 41.78.

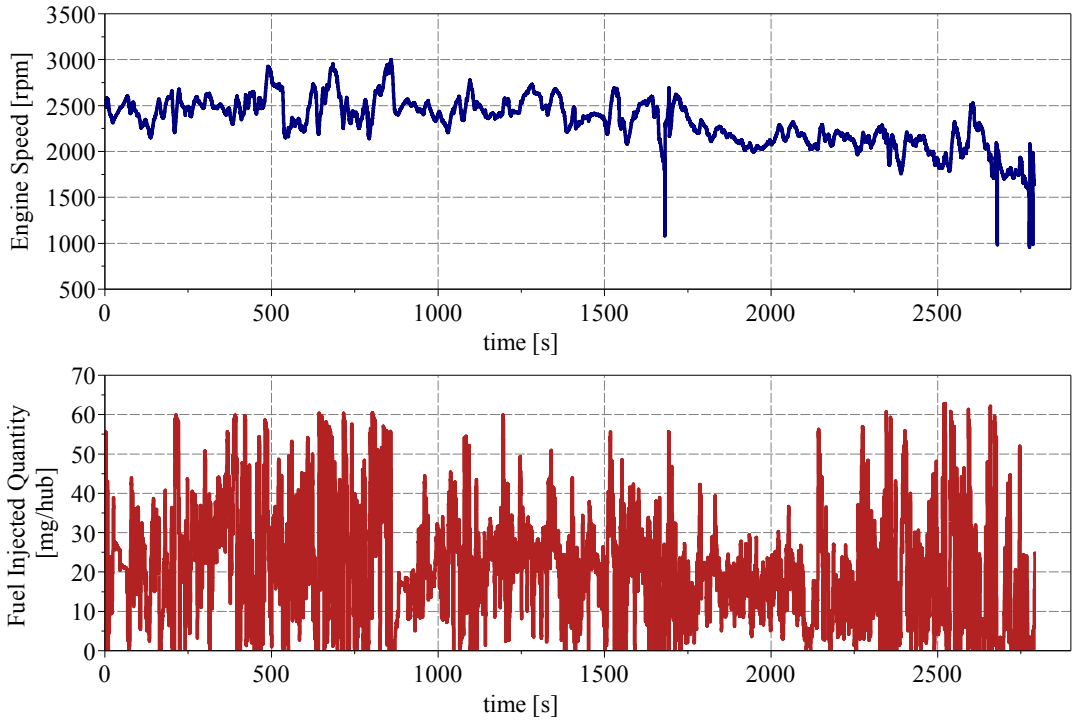

Figure 9.11 Engine speed and injected fuel quantity measured during RDE test

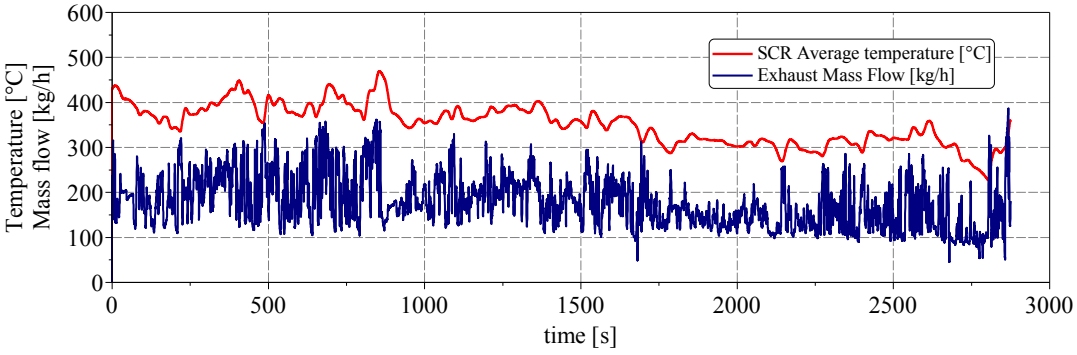

Figure 9.12 Average SCR temperature and exhaust mass flow measured during RDE test

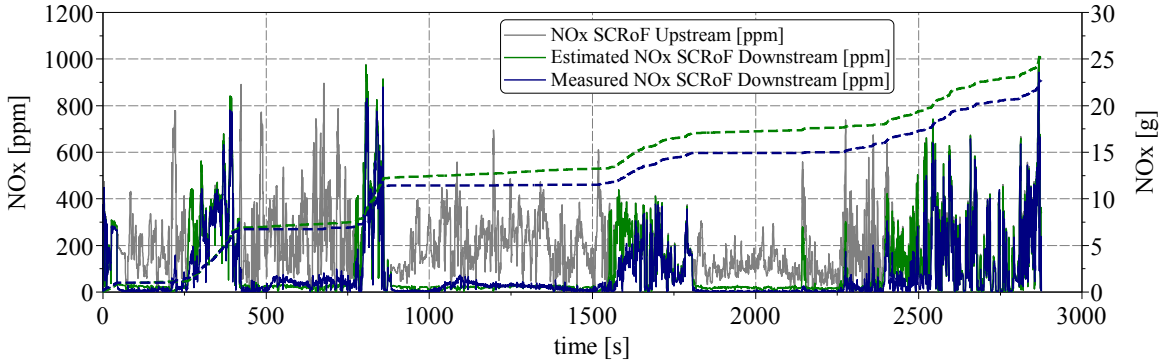

Figure 9.13 Results of the RDE test. Continuous line: comparison between the instantaneous measured NOx SCRoF upstream, measured and estimated NOx SCRoF downstream. Dashed line: NOx cumulate curves

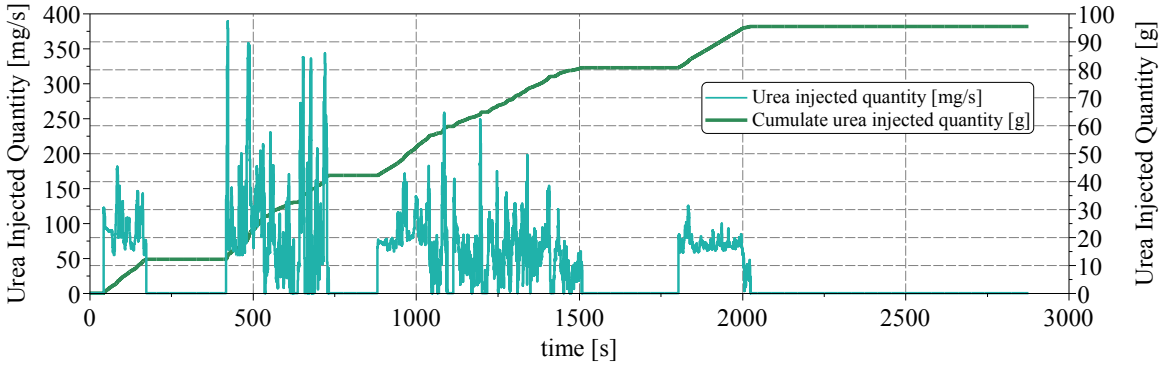

Figure 9.14 Urea injected quantity during RDE test

Conclusion

The implementation of a SCR kinetic model in the ECU allows to estimate the emission at SCR outlet and, hence, to characterize the catalyst. The improvement of an already developed SCR kinetic model is the object of this work that has the purpose to replace the unique and generic reduction NOx equation, that is currently implemented, with the NOx reduction scheme that includes standard, fast and slow reactions.

The main aim is to generate a code implementable in the ECU for real time estimation. In order to get it, it is necessary to have a previous benchmark. Therefore, two attempts have been tested in Matlab/Simulink. The first one is an explicit code. It has been verified that the problem is a stiff problem which can not be solved with an explicit code even if it is easier to implement in the ECU than implicit algorithm. Then, an implicit code –ode23s Matlab library- has been used.

For this algorithm a preliminary calibration has been conducted. In particular, filling and empty tests have been used to characterize the system while a WLTC and a RDE trace has been used to test the model. It is necessary to underline that the results are the outcome of a DoE approach that consists in the variation of the calibration parameters within plausible ranges. After this preliminary study the model has the following results: on the WLTC the cumulate error is 5.98% with a RMSE of 23.98. On the RDE trace the cumulate error is 10.66% with a RMSE of 41.78. The obtained results can be considered as satisfying.

Further steps could incorporate the implementation of a code in the ECU and the check of the performance against and the benchmark from this work. Then an optimization tool would be necessary in order to validate the model with less time possible and highest efficiency. Finally, the comparison between the original and the improved model would give evidence about the gained performance.

Acknowledge

For the development of this thesis the author would like to thank:

- Prof. Sergio Camporeale
- Bosch- CVIT in Modugno (Bari) for the use of facilities and for the technical support; in particular, Eng. Soenke Mannal, Eng. Dr. Roberto Saracino, Eng. Dr. Maria Rosaria and Eng. Dr. Sebastian Fischer. The author thanks Daniela Ingrosso and Marco Benegiamo for the valid support given her during the developing of their master thesis.
- BOSCH GmbH – Stuttgart- for the development of the second part of this work and, in particular, Eng. Dr. Andreas Fritsch.
- all the colleagues met in Bari and in Stuttgart.

References

1. https://www.dieselnet.com/standards/cycles/#eu

2. Houben, H., Marto, A., Pechhold, F., Haussner, M., Borgers, M., “Pressure Sensor Glow Plug (PSG) for Diesel Engines”. MTZ worldwide 11/2004 Volume 65. BERU Aktiengesellschaft. Printed in Germany 02.11.04 Bestell- Nr. 5 000 001 085. www.beru.com

3. Seykens, X., Baert, R., Somers, L., and Willems, F., "Experimental Validation of Extended NO and Soot Model for Advanced HD Diesel Engine Combustion," *SAE Int. J. Engines* 2(1):606-619, 2009, doi:10.4271/2009-01-0683.

4. D’Ambrosio, S., Finesso, R., Fu, L., Mittica, A., Spessa, E., “A control-oriented real-time semi-empirical model for the prediction of NOx emissions in diesel engines” ELSEVIER Applied Energy, 2014, doi:10.1016/j.apenergy.2014.05.046

5. Asprion, J., Chinellato, O., Guzzella, L., “A fast and accurate physics-based model for the NO_x emissions of Diesel engines” ELSEVIER Applied Energy, 2012, doi:10.1016/j.apenergy.2012.09.038

6. Molina, S., Guardiola, C.,Martin, J., Garcia Sarmiento, D., “Development of a control-oriented model to optimise fuel consumption and NO_X emissions in a DI Diesel engine”, ELSEVIER Applied Energy, 2014 doi:10.1016/j.apenergy.2014.01.021

7. Lakshminarayanan,P.A., Aghav,V., “Oxides of Nitrogen from Direct Injection Diesel Engines”. Mechanical Engineering Series pp 189-201

8. Flynn, Durrett, L. Hunter, zur Loye, Akinyemi, Dec, Westbrook, “Diesel Combustion: An Integrated View Combining Laser Diagnostics, Chemical Kinetics, and Empirical Validation”, 1999 Society of Automotive Engineers International Congress and Exposition

9. Heywood, “Internal Combustion Engine Fundamentals.” McGrawHill

10. Walke, N., Marathe, N., and Nandgaonkar, M., "Simplified Combustion Pressure and NOx Prediction Model for DI Diesel Engine," SAE Technical Paper 2013-26-0131, 2013, doi:10.4271/2013-26-0131.A semi-empirical model for rapid NOx concentration evaluation

11. Finesso, R. and Spessa, E., "Real-Time Predictive Modeling of Combustion and NO_x Formation in Diesel Engines Under Transient Conditions," SAE Technical Paper 2012-01-0899, 2012, doi:10.4271/2012-01-0899.

12. Kaa, B., Sosio,M., Grill, M., Bargende, M., “Transient Simulation of Nitrogen Oxide Emissions of CI Engines” , 2nd Conference on Engine Processes July 02 - 03, 2015, Berlin Universitätsverlag der TU Berlin, Published online on the Digital Repository of the Technische Universität Berlin: URN urn:nbn:de:kobv:83-opus4-66261, http://nbn-resolving.de/urn:nbn:de:kobv:83-opus4-66261

13. Quérel, C., Grondin, O., and Letellier, C., "State of the Art and Analysis of Control Oriented NOx Models," SAE Technical Paper 2012-01-0723, 2012, doi:10.4271/2012-01-0723.

14. Kihas, D. and Uchanski, M., "Engine-Out NOx Models for on-ECU Implementation: A Brief Overview," SAE Technical Paper 2015-01-1638, 2015, doi:10.4271/2015-01-1638.

15. Andersson, M., Johansson, B., Hultqvist, A., and Noehre, C., "A Predictive Real Time NOx Model for Conventional and Partially Premixed Diesel Combustion," SAE Technical Paper 2006-01-3329, 2006, doi:10.4271/2006-01-3329.

16. C. Guardiola, J.J. López, J. Martín, D. García-Sarmiento, “Semiempirical in-cylinder pressure based model for NOX prediction oriented to control applications”, Applied Thermal Engineering Volume 31, Issue 16, November 2011, Pages 3275–3286, ELSEVIER, doi:10.1016/j.applthermaleng.2011.05.048

17. Arrègle, J., López, J., Guardiola, C., and Monin, C., "Sensitivity Study of a NOx Estimation Model for On-Board Applications," SAE Technical Paper 2008-01-0640, 2008, doi:10.4271/2008-01-0640.

18. Quérel, C., Grondin, O., and Letellier, C., "A Semi-Physical NOx Model for Diesel Engine Control," SAE Technical Paper 2013-01-0356, 2013, doi:10.4271/2013-01-0356.

19. Wonah Parka, Junyong Leea, Kyoungdoug Mina, , , Jun Yub, Seungil Parkb, Sunghwan Chob “Prediction of real-time NO based on the in-cylinder pressure in Diesel engines” Proceedings of the Combustion Institute Volume 34, Issue 2, 2013, Pages 3075–3082 ELSVIER doi:10.1016/j.proci.2012.06.170

20. Lee, J., Lee, S., Park, W., Min, K. et al., "The Development of Real-time NOx Estimation Model and its Application," SAE Technical Paper 2013-01-0243, 2013, doi:10.4271/2013-01-0243.

21. Savva, N.,Hountalas, D., “Detailed evaluation of a new semi-empirical two zone Nox model by application on various diesel engine configurations”, DOI: 10.4271/2012-01-1156 Conference: SAE international, At Detroit

22. Maroteaux,F. and Saad, C., “Combined mean value engine model and crank angle resolved in-cylinder modeling with NOx emissions model for real-time Diesel engine simulations at high engine speed”, Energy .Volume 88 -August 2015-Elsevier-doi:10.1016/j.energy.2015.05.072

23. Ericson, C., Westerberg, B., Andersson, M., and Egnell, R., "Modelling Diesel Engine Combustion and NOx Formation for Model Based Control and Simulation of Engine and Exhaust Aftertreatment Systems," SAE Technical Paper 2006-01-0687, 2006, doi:10.4271/2006-01-0687.

24. Amin, E., Pecheny, V., Gravante, S., and Siow, Y., "A Computational Procedure for Predicting Nitrogen Oxide Emissions from Diesel Engines," SAE Technical Paper 2006-01-0240, 2006, doi:10.4271/2006-01-0240.

25. Wilhelmsson, C., Tunestål, P., Widd, B., and Johansson, R., "A Physical Two-Zone NO_x Model Intended for Embedded Implementation," SAE Technical Paper 2009-01-1509, 2009, doi:10.4271/2009-01-1509.

26. Mellor, A., Mello, J., Duffy, K., Easley, W. et al., "Skeletal Mechanism for NOx Chemistry in Diesel Engines," SAE Technical Paper 981450, 1998, doi:10.4271/981450

27. Easley, W., Mellor, A., and Plee, S., "NO Formation and Decomposition Models for DI Diesel Engines," SAE Technical Paper 2000-01-0582, 2000, doi:10.4271/2000-01-0582.

28. Psota, M. and Mellor, A., "Dynamic Application of a Skeletal Mechanism for DI Diesel NOX Emissions," SAE Technical Paper 2001-01-1984, 2001, doi:10.4271/2001-01-1984.

29. Rao, V., Honnery,D., “A comparison of two NO_x prediction schemes for use in diesel engine thermodynamic modelling”, Fuel Volume 107, May 2013, Pages 662-670, ELSEVIER, doi:10.1016/j.fuel.2013.01.071

30. Hegarty, K., Favrot, R., Rollett, D., and Rindone, G., "Semi-Empiric Model Based Approach for Dynamic Prediction of NOx Engine Out Emissions on Diesel Engines," SAE Technical Paper 2010-01-0155, 2010, doi:10.4271/2010-01-0155

31. Roberto Finesso, Ezio Spessa, "A real time zero-dimensional diagnostic model for the calculation of in-cylinder temperatures, HRR and nitrogen oxides in diesel engines", Energy Conversion and Management Volume 79, March 2014, Pages 498–510, ELSEVIER , doi:10.1016/j.enconman.2013.12.045

32. Catania, A., Finesso, R., and Spessa, E., "Diagnostics of Mixing Process Dynamics, Combustion and Emissions in a Euro V Diesel Engine," SAE Technical Paper 2011-24-0018, 2011, doi:10.4271/2011-24-0018.

33. Egnell, R., "Combustion Diagnostics by Means of Multizone Heat Release Analysis and NO Calculation," SAE Technical Paper 981424, 1998, doi:10.4271/981424.

34. Andersson, M., Johansson, B., Hultqvist, A., and Nöhre, C., "A Real Time NOx Model for Conventional and Partially Premixed Diesel Combustion," SAE Technical Paper 2006-01-0195, 2006, doi:10.4271/2006-01-0195.

35. Fremovici, M.., Grondin, O., «Compression Ingnition Engine Model Supporting Powertrain Development», ResearchGate, Conference paper, November 2009, doi:10.3182/20091130-3-FR-4008.00007

36. Aithal ,S.M., "Modeling of NO_x formation in diesel engines using finite-rate chemical kinetics", Applied Energy Volume 87, Issue 7, July 2010, Pages 2256–2265, ELSEVIER doi:10.1016/j.apenergy.2010.01.011

37. S.M. Aithala, , , D. Upadhyayb, "Feasibility study of the potential use of chemistry based emission predictions for real-time control of modern diesel engines", Applied Energy Volume 91, Issue 1, March 2012, Pages 475–482, ELSEVIER, doi:10.1016/j.apenergy.2011.10.005

38. Westlund, A. and Ångström, H., "Fast Physical Prediction of NO and Soot in Diesel Engines," SAE Technical Paper 2009-01-1121, 2009, doi:10.4271/2009-01-1121.

39. Stiesch, G. and Merker, G., "A Phenomenological Model for Accurate and Time Efficient Prediction of Heat Release and Exhaust Emissions in Direct-Injection Diesel Engines," SAE Technical Paper 1999-01-1535, 1999, doi:10.4271/1999-01-1535.

40. Miller, R., Davis, G., Lavoie, G., Newman, C. et al., "A Super-Extended Zel'dovich Mechanism for Nox Modeling and Engine Calibration," SAE Technical Paper 980781, 1998, doi:10.4271/980781.

41. D. J Timoney, J M Desantes, L Hernández, C M Lyons, "The development of a semi-empirical model for rapid NOx concentration evaluation using measured in-cylinder pressure in diesel engines", Proceedings of the Institution of Mechanical Engineers, Part D: Journal of Automobile Engineering May 1, 2005 vol. 219 no. 5 621-631, doi: 10.1243/095440705X11095

42. Desantes, J., López, J., García, J., and Hernández, L., "Application of Neural Networks for Prediction and Optimization of Exhaust Emissions in a H.D. Diesel Engine," SAE Technical Paper 2002-01-1144, 2002, doi:10.4271/2002-01-1144

43. Traver, M., Atkinson, R., and Atkinson, C., "Neural Network-Based Diesel Engine Emissions Prediction Using In-Cylinder Combustion Pressure," SAE Technical Paper 1999-01-1532, 1999, doi:10.4271/1999-01-1532.

44. Arsie, I., Pianese, C., and Sorrentino, M., "Development of recurrent neural networks for virtual sensing of NOx emissions in internal combustion engines," SAE Int. J. Fuels Lubr. 2(2):354-361, 2010, doi:10.4271/2009-24-0110.

45. WANG Jun, ZHANG Youtong, XIONG Qinghui, DING Xiaoliang "NOx Prediction by Cylinder Pressure Based on RBF Neural Network in Diesel Engine", 2010 International Conference on Measuring Technology and Mechatronics Automation

46. Henningsson, Maria LU ; Tunestål, Per LU and Johansson, Rolf LU (2012) "A Virtual Sensor for Predicting Diesel Engine Emissions from Cylinder Pressure Data" 2012 IFAC Workshop on Engine and Powertrain Control, Simulation and Modeling (E-COSM'12) In 2012 IFAC Workshop on Engine and Powertrain Control, Simulation and Modeling p.424-431

47. Atkinson, C., Long, T., and Hanzevack, E., "Virtual Sensing: A Neural Network-based Intelligent Performance and Emissions Prediction System for On-Board Diagnostics and Engine Control," SAE Technical Paper 980516, 1998, doi:10.4271/980516.

48. Heiko Sequenz, Rolf Isermann "Emission Model Structures for an Implementation on Engine Control Units", 18th IFAC World Congress Milano (Italy) August 28 - September 2, 2011

49. Ericson, C., Westerberg, B., and Egnell, R., "Transient Emission Predictions With Quasi Stationary Models," SAE Technical Paper 2005-01-3852, 2005, doi:10.4271/2005-01-3852.

50. J. D. Martínez-Morales , E. R. Palacios-Hernández, G. A. Velázquez-Carrillo "Modeling engine fuel consumption and NOx with RBF neural network and MOPSO algorithm", International Journal of Automotive Technology December 2015, Volume 16, Issue 6, pp 1041-1049 SPRINGER 2015

51. Nicol, D., Malte, P.C., Lai, J., Marinov, N.N. and Pratt, D.T., "NOx sensitivities for gas turbine engines operated on lean-premixed combustion and conventional diffusion flames," ASME Paper No. 92-GT-115, 1992

52. Polifke, W., Döbbeling, K., Sattelmayer, T., Nicol, D.G. and Malte, P.C., "A NOx prediction scheme for lean-premixed gas turbine combustion based on detailed chemical kinetics," ASME Paper No. 95-GT-108, 1995

53. https://www.dieselnet.com/tech/cat_scr.php

54. Wurzenberger, J., Wanker, R., "Multi-Scale SCR Modeling, 1D Kinetic Analysis and 3D System Simulation".

55. Chi, J. and DaCosta, H., "Modeling and Control of a Urea-SCR Aftertreatment System," SAE Technical Paper 2005-01-0966, 2005, doi:10.4271/2005-01-0966.

56. Tang, W., Youngren, D., SantaMaria, M., and Kumar, S., "On-Engine Investigation of SCR on Filters (SCRoF) for HDD Passive Applications," *SAE Int. J. Engines* 6(2):862-872, 2013, doi:10.4271/2013-01-1066.

57. Balland, J., Parmentier, M., and Schmitt, J., "Control of a Combined SCR on Filter and Under-Floor SCR System for Low Emission Passenger Cars," *SAE Int. J. Engines* 7(3):1252-1261, 2014, doi:10.4271/2014-01-1522.

58. Lietti, L., Nova, I., Tronconi, E., Forzatti, P., "Transient kinetic study of the SCR-deNOx reaction"

59. Tronconi, E., Cavanna, A., Forzatti, P., “Unsteady Analysis of NO Reduction over Selective Catalytic Reduction –DeNOx Monolith Catalysts”, Ind.Eng.Chem.Res. 1998,37,2341-2349

60. Tronconi, E., Lietti, L., Forzatti, P., Malloggi, S., “Experimental and Theoretical Investigation of the Dynamics of the SCR- DeNOx Reaction”. Chemical Engineering Science, Vol.5, No.11, pp.2965-2970, 1996

61. Sjovall, H., Blint, R., Olsson, L., “Detailed kinetic modeling of NH3 SCR over Cu-ZSM-5”

62. Julien Alexandre dit Sandretto, Alexandre Chapoutot “Validated Explicit and Implicit Runga-Kutta Methods”

63. Watling, Tutuianu, Desai “Development and validation of a Cu-Zeolite SCR Catalyst Model”

64. https://www.dieselnet.com/tech/dpf.php